DISS. ETH NO. 23034

The Influence of Forest Canopy Structure on Snow Hydrology

A thesis submitted to attain the degree of

DOCTOR OF SCIENCES of ETH ZURICH

(Dr. sc. ETH Zurich)

presented by

Charles David Moeser

Msc, University of Nevada, Reno

born on *30.05.1977*

citizen of United States of America

accepted on the recommendation of

Prof. Dr. Harald Bugmann
Dr. Tobias Jonas
Dr. Felix Morsdorf
Prof. Dr. Jan Seibert

2015

Contents

Abstract

Snowmelt dominated watersheds which contain forests yield approximately 60% of the global freshwater runoff. Forest snow interception ranges from 0 to 60% of the total annual snowfall in these areas and creates large snow storage differences between open and forested environments. Snow sublimation rates are much higher in the canopy than in the open and range up to 50% of the total annual snowfall. This large range of interception when paired with a similarly large range in sublimation makes interception the single most dominant physical process to determine runoff from forest areas which house snow. There have been a significant number of snow melt models which included canopy snow interactions. However these models could not reproduce the natural heterogeneity in under-canopy snow cover due to an overly simplistic representation of interception processes. This thesis represents the steps toward the development and implementation of a new interception model valid for discrete time steps, various scales (individual canopy element to forest stand scale) and heterogeneous canopy structures. For the first time, this new model has allowed for the spatial variability of forest snow to be modeled.

Seven forested and two open field areas were set-up in the Summer / Fall 2012 surrounding Davos, Switzerland, with 1982 surveyed and marked points for a three year study. During the 2012-2015 winter seasons, interception, under-canopy snow depth (SD), and under-canopy snow water equivalent (SWE) measurements were made at these points, constituting the largest interception field study performed to date (total of ~84000 manual measurements). Aerial LiDAR data (ALS) were also available at all field areas from a flyover in 2010.

Leaf area index (LAI), canopy closure (CC), and potential incoming solar radiation (PISR) were derived at all field points from the conversion of the birds-eye ALS perspective into a ground viewpoint angular perspective (synthetic images). The synthetic images, demonstrated better correlations than standard ALS methods (r: 0.93 for CC, r: 0.83 for LAI and r: 0.90-0.94 for PISR) when compared to the parameters derived from hemispherical photos at 112 ground points. Novel forest structure metrics were also created at each field point in order to describe the location of the points relative to canopy gaps. Two new metrics,

'mean distance to canopy' and 'total gap area' displayed the highest correlations to interception. Unlike the variable pairing (LAI and CC) found in the standard model, no cross correlation was present. The new metrics were used in tandem with CC, to define the maximum interception capacity (Imax) of a canopy element.

Two physical processes, snow bridging and branch bending were apparent at the field points and an interception efficiency function (interception / precipitation) based upon precipitation values was formulated to mimic these processes. Imax and the efficiency distribution were then integrated to formulate a conceptual model of interception based upon the snow interception measurements. This model displayed a ~27% increase in R^2 (from 0.39 to 0.66) and a ~40% reduction in RMSE (from 5.19 to 3.39) as compared to previous models at the point scale. When up-scaled to larger grid sizes, the model demonstrated further increases in performance.

Due to the inclusion of forest structure parameters (mean distance to canopy and total gap area) in the new model, modeled interception was able to mimic the canopy structure layout, while prior modeling efforts demonstrated homogenous interception estimations even under highly heterogeneous canopy conditions. The large variance of estimated interception between points from the new model translated to approximately double the variance of under-canopy SD, under-canopy SWE and snow on canopy sublimation when compared to prior models. This variance was dictated by the canopy structure, and analogous to the interception estimates, demonstrated a much better fit to the field data than prior modeling approaches.

The pairing of snow bridging and branch bending with the forest structure parameters has allowed, for the first time, accurate representation of the extreme spatial variability of forest snow in a model environment. The effects of interception on under-canopy snow melt processes can now be represented and related to canopy structure characteristics. These improvements not only provide better representations of interception and under-canopy snow at the point scale, but they also allow for improved snow modeling over larger areas.

Zusammenfassung

Einzugsgebiete, deren Abfluss wesentlich von der Schneeschmelze abhängt und die Wald enthalten, liefern in etwa 60% des globalen Süsswasserabflusses. Grosse Unterschiede in der Mächtigkeit der Schneedecke entstehen zwischen freien und bewaldeten Flächen, da in Wäldern jährlich bis zu 60% des Schneefalls von den Baumkronen abgefangen wird. Der Anteil an Schnee, der von dort direkt sublimiert, beträgt bis zu 50% des jährlichen Gesamtschneefalls und ist damit um einiges grösser als im offenen Gelände. Wegen der grossen Spanne an möglicher Sublimation von interzipierten Schnee, ist die Interzeption der wichtigste physikalische Prozess ist, welcher den Schneeschmelzanteil am Abfluss in bewaldeten Einzugsgebieten bestimmt. Zahlreiche Schneeschmelzmodelle versuchen, die Entwicklung der Schneedecke in solchen Gebieten zu simulieren, können aber, auf Grund von stark vereinfachten Annahmen bezüglich der Interzeption die natürliche Variabilität der Schneedecke am Waldboden nicht abbilden. Die vorliegende Arbeit zeigt die Entwicklung und Implementierung eines neuen Modellansatzes auf, der die Interzeption auf unterschiedlichen Skalen (vom Einzelbaum bis zu ganzen Baumbeständen) für einzelne Zeitschritte und für unregelmässige Waldstrukturen abbilden kann. Dank dieses neuen Modells ist es zum ersten Mal möglich, die räumliche Variabilität der Schneedecke in Wäldern darzustellen.

Neun Versuchsflächen (davon sieben innerhalb und zwei ausserhalb von Wäldern) in der Umgebung von Davos (Graubünden, Schweiz) wurden im Herbst 2012 ausgewählt. In den Flächen wurden insgesamt 2032 Vergleichspunkte für die darauffolgende dreijährige Feldstudie vermessen und markiert. An diesen Punkten wurden in den Wintern 2012/13 bis 2014/15 folgende Grössen gemessen: die Schneehöhe (SD), die Schneeinterzeption sowie das Schneewasseräquivalent (SWE). Mit insgesamt über 84000 Messungen handelt es sich hierbei um die bis heute wohl umfassendste Feldstudie bezüglich der Interzeption von Schnee im Wald. Desweiteren standen vom Jahr 2010 Luftaufnahmen (airborne laser scanning, ALS) für sämtliche Versuchsflächen zur Verfügung.

Aus den ALS- Daten wurden künstliche Bilder der Vegetation aus der Bodenperspektive erzeugt, um den Blattflächenindex (LAI), den Kronenbedeckungsgrad (CC) und die potentielle Sonneneinstrahlung (PISR) zu berechnen. Die neuartige Bestimmungsmethode dieser Parameter lieferte gegenüber traditionellen ALS Methoden wesentlich bessere Ergebnisse (r: 0.93 bei CC, r: 0.83 bei LAI und r: 0.90-0.94 bei PISR). Ausserdem wurden neue Parameter entwickelt, um die Lage der Vergleichspunkte in Beziehung zur Waldsturktur zu beschreiben. Zwei dieser neuen Waldstrukturparameter (mean distance to canopy, total gap area) korrelierten stärkster mit der gemessenen Interzeption als traditionelle Parameter. Ausserdem zeigten die üblicherweise in Schneemodellen verwendeten Parameter LAI und CC eine starke Kreuzkorrelation, welche bei den neuen Waldstrukturparametern nicht auftritt. Die neuen Waldstrukturparameter wurden in Kombination mit CC verwendet, um die maximal mögliche Interzeption an einem Ort (Imax) zu bestimmen.

Die beiden physikalischen Prozesse der Schneebrückenbildung ('snow bridging') und des Biegen der Äste unter der Schneelast ('branch bending') wurden an allen Vergleichspunkten beobachtet. Sie beeinflussen die Interzeptionsrate, welche durch das Verhältnis von Interzeption zu Schneeniederschlag beschrieben wird. Basierend auf den im Feld gemessenen Interzeptionswerten, dem Verhältnis von Interzeption zu Schneeniederschlag und Imax wurde ein konzeptionelles Modell für die Interzeption entwickelt. Verglichen mit bisherigen Modellen verbesserte sich die Modellgüte an den Vergleichspunkten beim R^2 um ~27% (von 0.39 auf 0.66), und der RMSE nahm um ~40% ab (von 5.19 auf 3.39). Auf grösseren Skalen konnte sich die Modellgüte noch weiter steigern.

Die Anwendung bisheriger Modelle zeigte räumlich kaum variable Interzeption selbst bei stark unregelmässigen Waldstrukturen. Auf Grund der Berücksichtigung der neuen Parameter zur besseren Beschreibung der Waldstruktur war es möglich ein Modell zu entwickeln, das realistischere Interzeptionsmuster generiert. Die Tatsache, dass die so modellierte Interzeption zwischen einzelnen Punkten sehr stark variierte, führte dazu, dass sich die Varianz der Schneehöhe, des Schneewasseräquivalents im Wald und der Sublimation verglichen mit früheren Modellen in etwa

verdoppelte. Diese Varianz wird durch die unregelmässige Waldstruktur verursacht, welche, ähnlich wie die modellierte Interzeption, besser mit den gemessenen Felddaten übereinstimmte.

Zum ersten Mal ist es somit möglich, die räumlich äusserst ungleichmässige Verteilung von Schnee im Wald zu modellieren, indem wichtige Prozesse sowie neue Waldstrukturparameter berücksichtigt wurden. Dadurch können nun die Auswirkungen der Interzeption auf die Schneeschmelze in bewaldeten Gebieten bezüglich der vorhandenen Waldstruktur dargestellt werden. Durch diese neuen Ansätze kann die Interzeption und die Schneedecke an Punkten in bewaldeten Flächen besser abgebildet werden. Gleichzeitig erlaubt dieser Ansatz auch eine bessere Modellierung der räumlichen Schneeverteilung im Wald auf grösseren Skalen.

1 Introduction

1.1 Significance and Rationale

Mountain forests are critically linked to the hydrologic cycle and provide vital ecosystem services such as water supply and storage. Similarly, snow and ice are a crucial component of the world's freshwater reserve and help to sustain environmental and social needs. It is estimated that within the Northern hemisphere, 20% of the seasonal snow cover is located in forested areas and can account for 17% of total terrestrial water storage during the winter season (Guntner, et al., 2007; Rutter, et al., 2009). In the United States, for example, stream flow from forest land provides almost two-thirds of the total freshwater supply with much of it coming from snow-dominated watersheds. Yet, forest structures within these zones are affected by climate change, variations in land management, and a variety of natural disturbances, all of which create uncertainty regarding the fate of this major source of water. Climate change impacts alone are projected to significantly increase the northern extent of the boreal forest. One-third to two-thirds of the tundra could transition to forest by the end of the century (IPCC, 1997). Accurate estimations of snowmelt and runoff rates from forested areas are of great importance to hydrologic forecasters throughout the world. However, despite their importance, forest snow melt and runoff are still poorly understood. The necessity to understand the interplay between forest structure and snow is made more important by alarmingly high global water withdrawal predictions ranging from an 18% to over 50% increase from the 2007 level (UNEP, 2007; Rosengrant et al., 2002).

1.2   Forest Snow Hydrology

Snow accumulation and ablation processes in open areas are reasonably well understood and represented in many numerical melt models for various scales and climate regimes (Anderson, 1976; Jordan, 1991; Marks et al., 1992; Price and Dunne, 1976; Tarboton and Luce, 1996). However, the processes within forested areas that dictate snow accumulation and ablation vary dramatically (unlike open areas). They demonstrate not only local (forest stand) and regional (landscape) fluctuations but also heterogeneity at extremely fine scales (individual canopy elements) (Jonas and Essery, 2011). The spatial properties of forest canopies greatly influence under-canopy snow physical properties, and create a much larger spatial heterogeneity of snow pack under-canopy as compared to open areas. Forest structure can augment or attenuate the physical processes affiliated with snow accumulation and ablation, as reviewed below.

The canopy absorbs varying percentages of shortwave radiation while redistributing the longwave radiation patterns (Essery et al., 2008; Musselman, 2012). The presence of trees changes the wind fields above the snow surface and typically acts to constrain the turbulent heat and moisture fluxes as compared to open areas (Li, et al., 2008; Pomeroy et al., 2008). Litter fall from trees such as needles and bark acts to change the surface albedo of the underlying snow, thus creating heterogeneous shortwave radiation absorption patterns on the snow surface (Pugh et al., 2012).

Further, snowfall that is intercepted by the canopy can sublimate, melt and drip, or fall to the forest floor (figure 1). Snow interception, i.e. the portion of falling snow that remains in the canopy, can amount to over 60% of total annual snowfall (Montesi et al., 2003; Storck et al., 2002). The canopy provides intercepted snow a raised and multi-tiered surface area, allowing for increased insolation and wind exposure. Consequently, sublimation rates of snow are much higher in the canopy than at the forest floor. Canopy snow sublimation also varies greatly over space, with sublimation losses ranging up to 50% of total annual snowfall with the majority of the variation due to canopy structure (Essery and Pomeroy, 2001;
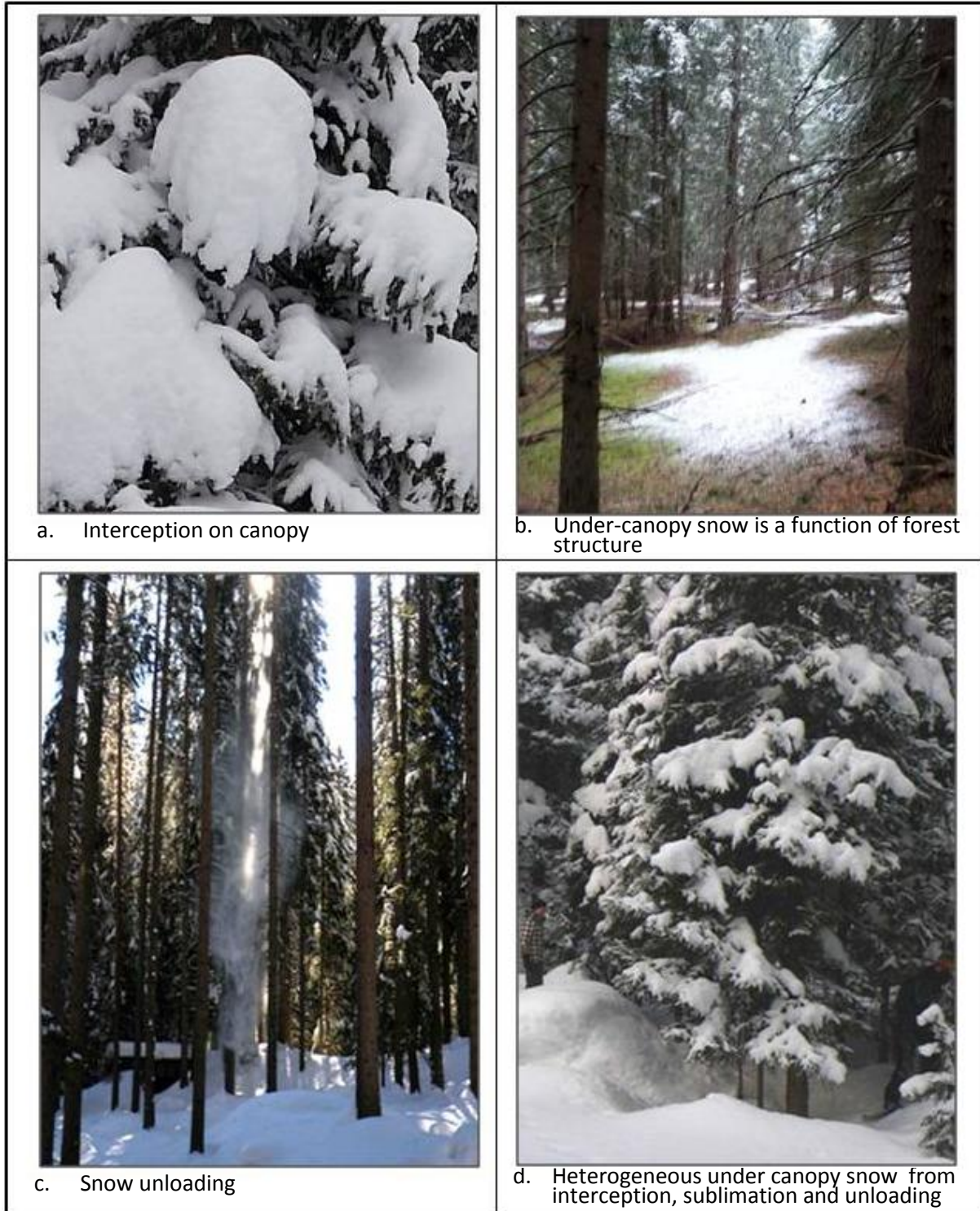
Figure 1: pictures representing interception (a), the effect of forest structure on under-canopy snow (b), mass unloading (c), and the interplay of interception, unloading and sublimation of under canopy snow around a tree (d). Photo a,c,d: David Moeser. Photo b: Giulia Mazzotti

Pomeroy, 1998; Lundberg and Halldin, 2001; Montesi et al., 2004; Suzuki et al., 2003,). The wide range of observed interception rates and sublimation losses makes interception the single most dominant physical process to drive snow cover heterogeneity in forest areas.

1.2.1   State of interception research

Snow interception has been studied for over 100 years with initial qualitative studies coming from the works of Carpenter (1901) in the U.S. Rocky Mountains, and Church (1912) in California's High Sierra Mountains. Church compared the patterns of gaps within a forest to snow distribution as a honeycomb matrix, where the largest amount of honey – or snow in this case – is stored in the combs or the forest gaps. Johnson (1942) was able to quantitatively demonstrate that snow interception is fundamentally different and much greater than rainfall interception.

More recent research has highlighted the importance of snow bridging and branch bending on the maximum canopy snow load and interception efficiency (interception / total precipitation). Tennyson et al. (1974) in Arizona and Bründl et al. (1999) in Switzerland visually captured these processes using time lapse photography. Both studies demonstrated an initial interception efficiency increase on Ponderosa Pine and Norwegian Spruce due to snow bridging.

The snow adhesion and cohesion processes, which lead to an increased surface area within the canopy, and subsequent snow bridging have also been qualitatively described by Miller et al. (1964) and Bunnel et al. (1995). Satterlund and Haupt (1967) were the first to model interception for specific snow storms in a Douglas-Fir and White Pine forest in Northern Idaho. They used a sigmoidal curve to describe interception efficiency changes in a storm event that are due to snow bridging and mass release from branch bending. The model displayed a maximum rise in interception efficiency due to snow bridging (rising limb of the sigmoidal curve) and a subsequent decrease in efficiency (falling limb in sigmoidal curve) as the overlying

intercepted weight increased. Schmidt and Gluns (1991a) furthered this work by studying branches of Engelmann Spruce, Subalpine Fir, Lodgepole Pine and artificial branches in Colorado, USA, and British Columbia, Canada. They found that the magnitude of the interception (and efficiency) was higher with the artificial, stiff branches, implying that interception depends on the bending potential of the branch or, more specifically, on initial branch stiffness and initial branch angle.

Despite the rather large volume of previous research on the interactions between the forest canopy and snowfall, very few studies have attempted to quantify snow interception in the form of an interception model that can be integrated within a snow melt model. Hedstrom and Pomeroy (1998) developed the first model suitable for discrete time steps that included specific canopy parameterizations (i.e., leaf area index (LAI) and canopy closure (CC)) to characterize the canopy of a boreal forest (Saskatchewan, CA). Their model used an exponential decay function to model interception efficiency, which continuously reduces interception efficiency through time and does not account for snow bridging, which has been shown to increase interception efficiency after the onset of a storm (Satterlund and Haupt, 1967; Schmidt and Gluns, 1991a). While it is possible that interception efficiency in boreal forests is dominated by different physical processes due to the underlying climatic differences, snow bridging is a common phenomenon in coniferous temperate forests that should be taken into account in models.

There have been four papers to date (Bunnell et al., 1985; Lundberg and Halladin 2001; Lundquist et al., 2013; Varhola et al., 2010b) that have synthesized the results of this long line of interception research, highlighting the contrasting methods and difficulties of snow interception measurements and modeling. These results have underscored that, despite major steps forward since the introduction of the 'honeycomb matrix,' there is still a need for interception models which are effective in various conditions and scales.

1.2.2   Interception and canopy measurements

A primary difficulty in developing an interception model valid in various conditions and scales is that significant efforts are needed to quantify snow interception. The standard method is destructive, as it relies on a cut, upright tree that is attached to a weighing mechanism that measures the weight increment induced by the intercepted snow during snow fall events (Hedstrom and Pomeroy, 1998; Nakai et al., 1994; Nakai et al., 1999b; Pomeroy, 1998; Satterlund and Haupt, 1967; Schmidt and Gluns, 1991; Storck et al., 2002; Suzuki and Nakai, 2008). Several other inventive methods have been developed in order to reduce the time and infrastructure needed for cut-tree experiments. Time lapse photography has been used to compare the visually inferred intercepted snow load to quantities defined from field measurements (Bründl et al., 1999; Kobayashi, 1987; Nakai et al., 1999a; Tennyson et al., 1974). Gamma ray attenuation has been used to measure the snow water equivalence (SWE) on branches (Calder, 1991). Due to the problems inherent to these techniques, however, neither interception data over large scales nor from a large sample set has been collected to date. Among the three studies that proposed a quantitative interception model, the largest data set was collected by Schmidt et al. (1991b) for a total of 175 branch samples (30 – 36 cm in length) over two seasons. Satterlund and Haupt (1967) used four tree saplings (3.7-4.2 meters tall) for a one-season study, and Hedstrom and Pomeroy (1998) used four Jack Pine trees (7 -15 meters in height and 38 – 90 kg in weight) over four seasons as well as one Black Spruce tree (12 meters in height and 22 kg in weight) over one season.

Similar to the difficulties of quantifying interception, conventional direct measurements for estimating canopy structure are labor-intensive and normally involve destructive sampling of the overstory. Nevertheless, there are several indirect measurement techniques including hemispherical photography, plant canopy analyzers (e.g. LAI-2000), or spherical densitometers. Their utility depends on the structural element that is targeted. Hemispherical photography (HP) is increasingly becoming the standard method

for canopy structure characterization. This technique, however, can deliver a broad range of estimates depending on the optical features of the camera and the settings of the program used for photo analysis and allows for derivations of point metrics only (Zhang et al., 2005). HP image acquisition and processing, like the other field methods, is also very time-consuming, thus limiting the utility of accurately describing canopy metrics for large areas.

Recent advances in Airborne Laser Scanning (ALS) have made this an increasingly common tool to accurately estimate three-dimensional canopy structure. The quantity and quality of the data are rapidly increasing, with large areas of the world already having data available (Asner et al. 2011; Fleck et al., 2012; Korhonen and Morsdorf, 2014; Lovell et al., 2003; Moeser et al., 2014; Morsdorf et al., 2006; Morsdorf et al., 2004; Riaño et al., 2004; Solberg, 2010; Solberg et al., 2009). The standard resolution of most data sets also allows for the effective estimation of CC and LAI as well as single tree characteristics such as canopy height, canopy bulk density, canopy base height, or fuel load (Erdody and Moskal, 2010; Kato et al., 2009; Korhonen and Morsdorf, 2011; Leeuwen and Nieuwenhuis, 2010; Morsdorf et al., 2006; Morsdorf et al., 2004). From ALS, large-scale features such as canopy openings and information how these are positioned relative to the surrounding forest can be derived. Such investigations close what was a significant research gap, and they have considerable implications for forest hydrology research (Varhola et al., 2010a; Zhao et al., 2011).

1.2.3   State of snow models

A significant number of snow melt models have included forest canopy representations. In 2007, an assessment of 33 of these models was performed (Essery et al., 2009; Rutter et al., 2009). This model inter-comparison initiative (SnowMIP2) constituted the first comprehensive assessment of the capabilities of these models to reproduce snow cover dynamics under canopy and revealed several important shortcomings (research gaps). Not only was a best fit model not found for the sites used, but performance

(of all models) showed much lower consistency within forested areas than in open areas, which underscored the sometimes overly simplistic representation of canopy processes.

All the models included in the comparative project that utilized a snow interception module (29 of 33) integrated CC and / or LAI to parameterize the canopy (Hedstrom and Pomeroy, 1998). However, field points that have the same LAI or CC can feature widely different large-scale canopy structures, such as open areas surrounding these points. Furthermore, the importance of the larger-scale forest structure has been highlighted as a major factor determining under-canopy SWE accumulation patterns and the timing of under-canopy snow melt (Golding and Swanson, 1986; Lopez-Moreno and Latron, 2008a; Lopez-Moreno and Stähli, 2008b; Troendle and Meiman, 1986; Varhola and Coops, 2013; Varhola et al., 2010a; Veatch et al., 2009; Winkler and Moore, 2006; Winkler et al., 2005). Specifically, a simplified representation of canopy structure can hamper the ability of current snowmelt models to accurately quantify the effect of forest canopy on snow accumulation and melt. For example, two forested sites with identical CC but different canopy gap size distributions can display systematically different SWE values. However, as SnowMIP2 pointed out, many current models have difficulties in contrasting these two situations.

1.3   Research Outline and Dissertation Structure

Three goals were defined prior to the start of this project in order to constrain the subsequent work with the overarching aim of improving under-canopy snow water resources modeling:

G1: Investigate the spatial distribution of under-canopy snow as it relates to specific structural aspects of the overlying canopy.

G2:   Develop enhanced representations of canopy structure in order to improve forest snow model performance.

G3: Develop procedures to integrate the enhanced representations of canopy coverages from the point to forest stand scale.

Taken as a whole, these goals helped fill several research gaps highlighted from the SnowMIP2 project (section 1.2.3). While each subsequent chapter can be read as a stand-alone paper, taken together they represent the steps toward the development and implementation of a new interception model. Chapters two and three focus on the creation and validation of novel ALS programs to derive traditional (chapter 2) and new canopy metrics (chapter 3) which corresponds to goal one. Chapter 4 utilizes the methods / canopy parameters from chapters 2 and 3 and assesses how they are related to an extensive snow interception data set and proposes a new interception model (goals two and three). Chapter 5 operationalizes the model from chapter 4 into a model applicable for discrete time snow melt modeling (goals two and three).

All chapters rely on extensive field data. Seven forested and two open field areas around Davos, Switzerland were equipped in Summer / Fall 2012 for a three-year study in which repeated interception, under-canopy snow depth, and under-canopy SWE measurements were made at 1982 points, comprising the largest interception field study performed to date (total of ~84000 manual measurements). The field areas were set up in diverse canopy structures and densities, and hemispherical photos were taken at 112 of these points for the validation of modeled canopy metrics (figure 2).
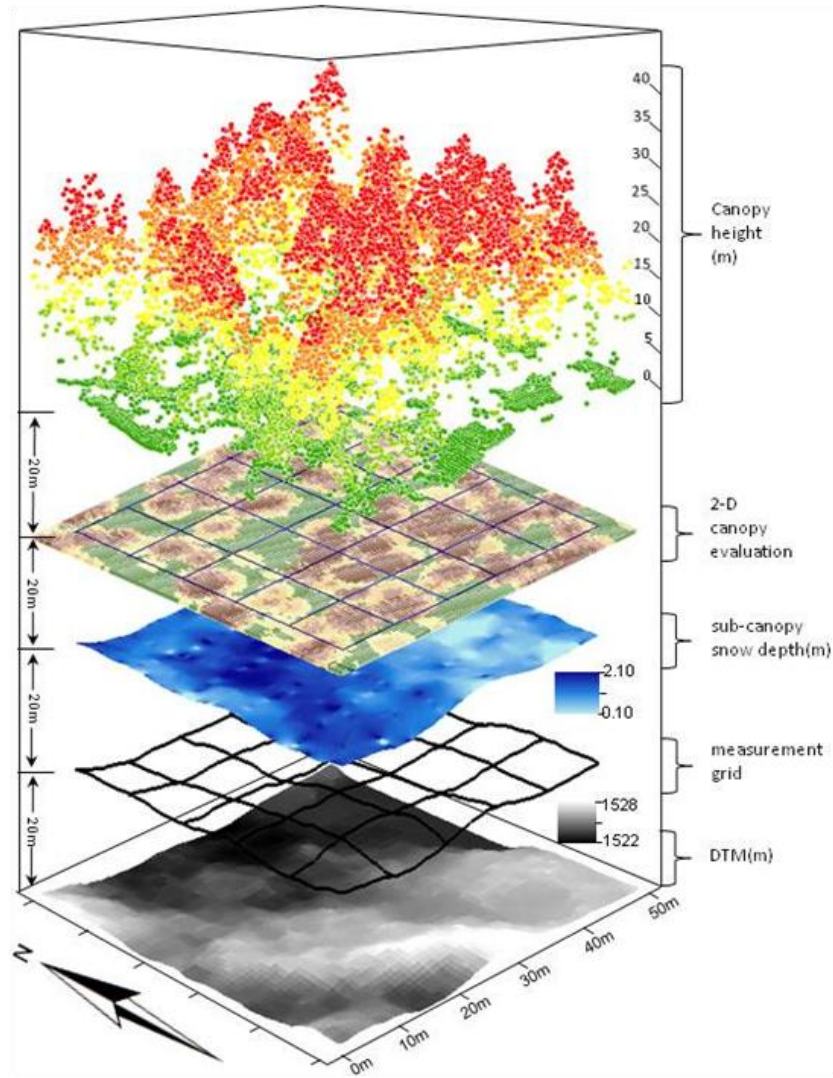
Figure 2. Conceptualized view of data integration from one field area

Chapter 2

A novel method is developed which converts ALS data to mimic hemispherical photos (synthetic images).

Thus, the standard downward-looking perspective of ALS data is converted into an upward-looking or

ground perspective. The Cartesian coordinate system of the ALS point cloud is also converted into a polar

system in order to mimic the angular viewpoint of hemispherical photos. The synthetic images are then

processed using standard image analysis software to derive CC, LAI, and potential incoming solar radiation

(PISR). The method is calibrated at each point where a hemispherical photo was taken. Upon calibration,

the method is fully automated and is applied at each of the 1932 forested field points, where the synthetic images demonstrate high correlations with low biases for each factor (LAI, CC, PISR) in all canopy conditions. These results are then compared to hemispherical photos as well as the output from implementation of standard ALS methods (for CC and LAI). Finally, the derivation of this method and its potential implementation for other datasets are discussed.

Chapter 3

A vector-searching algorithm is developed that searches ALS data in 192 directions around a point for the presence of canopy features. This algorithm creates new forest structure metrics that estimate the size and relative locations of forest gaps around a point. The foundation of the method and steps taken towards automating the algorithm are discussed. Forest structure metrics are derived for all field points. These metrics as well as LAI, CC and PISR from chapter 2 are correlated to the manual interception measurements at the field points. The cross-correlation between each metric as it relates to interception is analyzed from another novel automated method that pairs correspondence analysis and k-means clustering in order to answer the following questions: Should we use LAI and CC as the primary canopy descriptors within forest snow models? Are there more robust canopy descriptors that could be utilized? As with the method in chapter 2, transferability of the 'vector-searching algorithm' to other data sets is also reviewed.

Chapter 4

This section proposes a new model for the maximum interception capacity on a canopy element (I_{max}), which is based upon three canopy and forest structure metrics derived in chapters 2 and 3. The field data are analyzed and evidence of snow bridging and branch bending is seen in all field sites and at all points. The I_{max} model is then paired with an underlying sigmoidal distribution of interception efficiency to describe snow bridging and branch bending as a function of precipitation and canopy metrics to form a novel

interception model valid for storm events. This new interception model is compared with the standard interception model at differing storm sizes and a broad range of canopy densities. Significantly higher correlations and lower errors are seen in the new model. Both models are upscaled from the point to various grid sizes and compared. Similar results as with the point model comparison are seen. Finally, the utility of the canopy metrics in the new interception model are analyzed as a function of model performance and further compared to the traditional metrics used in the standard interception model.

Chapter 5

The storm-based model in Chapter 4 is converted into a model capable at discrete time steps. The model is used within an ensemble snow melt model, the Factorial Snow Model (FSM) at hourly time steps at 1272 field points for the 2012/13 and 2013/14 seasons. The interception, under-canopy SWE and under-canopy snow depth (SD) time series from FSM are compared to the snow measurements from this project. The data are further compared to the surrounding forest structure at each point. The spatial variability of the forest is found to be well captured in the interception estimates, under-canopy SD estimates and under-canopy SWE estimates mainly due to the inclusion of the new forest structure metrics. The FSM model is also utilized with the standard interception model, and the same analysis is performed where homogenous estimations of interception, under-canopy SWE and under-canopy SD are evident despite a highly heterogeneous canopy structure. Both underlying interception efficiency distributions unique to each interception model are analyzed as a function of storm intensity.

2

Canopy closure, LAI and radiation transfer from airborne LiDAR synthetic images

D. Moeser[1], J. Roubinek[1], P. Schleppi[2], F. Morsdorf[3], T. Jonas[1]

[1]WSL Institute for Snow and Avalanche Research SLF, Davos Dorf, Switzerland
Tobias Jonas: jonas@slf.ch   Jiri Roubinek: roubinek@slf.ch

[2]Swiss Federal Institute for Forest, Snow and Landscape Research WSL, Birmensdorf, Switzerland
Patrick Schleppi: patrick.schleppi@wsl.ch

[3]Remote Sensing Laboratories, Department of Geography, University of Zurich, Switzerland
Felix Morsdorf: felix.morsdorf@geo.uzh.ch

Abstract

Forest canopy structure and associated solar radiation fluxes greatly influence snow accumulation and melt and have large implications for water availability from forested areas. The ability to efficiently and explicitly infer canopy parameters at high resolution is crucial to improve the success of large scale applications of snow water resources modeling within these areas. In this paper, the utility of estimating leaf area index (LAI), canopy closure (CC) and below canopy potential incoming solar radiation (PISR) from synthetic hemispheric photos derived from airborne LiDAR data was evaluated. LAI and CC estimates from the synthetic LiDAR images were directly compared to actual hemispherical photos taken at 16 points at 7 field areas with heterogeneous canopy stand characteristics for a total of 112 photo comparison points. The synthetic data was further analyzed against LAI and CC derived from more traditional aerial LiDAR methods using a Cartesian space which integrates values over an area rather than a point based angular viewpoint. Furthermore, the PISR estimates were directly compared to in-situ radiometer measurements

taken at 30 different locations during clear sky conditions with heterogeneous canopy stand properties. When compared to the actual hemispherical photos, the CC and LAI metrics from synthetic images showed higher correlations and lower biases for all canopy coverage classes (r: 0.93 for CC and r: 0.83 for LAI) than the metrics from the Cartesian approach which displayed decreased correlations and higher biases with increasing canopy closure. Using a clear sky partitioning scheme for the direct and diffuse portions of the incoming shortwave radiation, the PISR was also accurately estimated from the synthetic images with average site correlations ranging from 0.90 to 0.94 where the timing and peak trends of both the diffuse and direct radiation components were well represented. Finally, a basic methodology for the steps toward automation of the process was presented in order to explicitly derive these metrics within similar LiDAR datasets.

2.1   Introduction

Forested headwaters that are snowmelt dominated produce 60% of the global freshwater runoff (Chang 2003). Within the Northern hemisphere it is estimated that 20% of the seasonal snow cover is located within forested areas and can account for 17% of total terrestrial water storage during the winter season (Guntner et al. 2007; Rutter et al. 2009). However, the state of forest structures within these zones is changing due to effects from climate change and land use management, as well as a variety of natural disturbances all of which create uncertainty regarding the fate of this major water cycle component. The necessity to better understand the interplay between forest structures and snow is augmented by alarmingly high global water withdrawal predictions ranging from an increase of 18-50% for just 13 years from now in 2025 (Rosengrant et al. 2002).

Arriving at accurate estimations of the variations in snowmelt and runoff rate from forested areas is of great importance to hydrologic forecasters throughout the world. However, accumulation and ablation of seasonal snow cover within forested areas exhibits very different dynamics as compared to snow within open areas (Jonas 2011; Pomeroy 1995). This is due to the surrounding forest structure acting to both

exacerbate and diminish involved physical processes, creating much greater spatial snow pack heterogeneity compared to open areas.

The multidimensional arrangement of overhead forest canopy characteristics controls a variety of physical under canopy energy and water balance drivers and standard snow modeling approaches integrate both leaf area index (LAI) and canopy closure (CC) (or sky view fraction) to describe the canopy. Conventional direct measurement methods for estimating the overhead canopy structure are severely labor intensive and typically involve destructive sampling of the overstory. However, there are a variety of indirect measurement schemes and their utility is dependent upon the canopy qualifier in question. These indirect field estimations of canopy structure include hemispherical photography, plant canopy analyzers like the LAI-2000, or a spherical densitometer and each have particular strengths and weaknesses depending on the specific structure element (Breda 2003; Hyer and Goetz 2004).

Similar to physical canopy structure measurements, field estimations of potential incoming solar radiation (PISR), or a composite of the direct and indirect components of shortwave radiation during clear sky conditions at specific points, can be costly and time consuming and generally necessitate radiometer array deployment around the field area. PISR measurements are variable through space as well as time and can drastically vary on a local level due to the presence of canopy components relative to the sun track. Most commonly, arrays of fixed sensors have been used to capture the spatial variability of radiation below the canopy (Link et al. 2004; Pomeroy et al. 2008). Alternatively, radiation sensors have been moved manually or automatically along ground transects, cables, or rails (Stähli et al. 2009; Sturm et al. 1995). This variation as compared to open areas necessitates measurement of multiple sites making it impractical to use ground-based measurement to estimate the spatial and temporal dynamics of PISR under canopy for large areas. Due to this, many practitioners have used estimates of canopy parameters such as LAI to empirically derive PISR (Hellström 2000). Hemispherical photographs can also be used, as the photographs serve as records of the geometry of canopy openings in order to determine precisely the PISR as it is related to the surrounding forest architecture (Thimonier et al. 2010; Musselman et al. 2012).

Hemispherical photography (HP) has traditionally been used to arrive at three key parameterizations, LAI, CC and more recently PISR, primarily because their determination is dependent on an angular viewpoint from a point to describe the distribution of multidirectional gap fractions. Despite the proven utility of HP, image acquisition and processing is very time consuming, thus limiting the utility of accurately describing these parameters for large areas. Aerial laser scanning (ALS) data has been increasingly utilized to derive estimates of these descriptors and is becoming more readily available for large areas throughout the world. Most practitioners utilize an area averaging approach where a basic ratio of canopy pixels to total pixels based on an analysis of grid size as well as height cutoff for canopy closure whereupon correlations with hemispherical photos are generally good (Lovell et al. 2003; Riaño et al. 2004).

Many estimates of LAI from ALS utilize a ratio of canopy returns to total echo returns over an area to arrive at a LAI proxy for a point (Morsdorf et al. 2006; Solberg 2010; Solberg et al. 2009). However these methods do not directly integrate an angular field of view which is why relating these different perspectives creates intrinsic difficulties when comparing the area averaged output to a point based output such as hemispherical photography (Varhola et al. 2012). The downward looking vertical distribution of foliage from ALS and upward looking angular distribution which integrates larger volumes of branches and trunks from hemispherical photography for a point affects an accurate inter-comparison of the two (Figure 2). Furthermore, these methods necessitate averaging values over larger areas for an individual point implicating a utility directed at area based rather than point based estimates. Several recent studies have converted ALS data from a traditionally Cartesian or X,Y,Z space into a polar system in order to mimic point based hemispherical photographs which are increasingly thought of as the standard for derivation of these parameters (Alexander et al. 2013; Musselman et al. 2013; Varhola and Coops 2013; Varhola et al. 2012). This new development also allows for a visual as well as quantitative analysis of the output giving a physical basis to LiDAR based approaches as well as greatly reducing the requisite setup and processing time needed to take real hemispherical photos.

This study has created a methodology allowing for direct extrapolation of LAI, CC and PISR from the conversion of ALS into a ground view angular perspective. We have automated the process of explicitly creating LiDAR derived hemispherical photos (synthetic images), and the subsequent parameter estimations (LAI, CC, PISR). We then directly compared these to the parameters derived from hemispherical photos taken on the ground. In order to evaluate the utility of a point based angular perspective, the LAI and CC estimates were further compared with those derived from a standard areal averaging Cartesian approach by utilizing a basic form of the methods highlighted in the works of Fleck et al. (2012), Morsdorf et al. (2006) and Solbereg et al. (2009). Finally the PISR estimations were then directly compared to a series of ground based radiometer arrays in various canopy and topography regimes. This is the first study of which we are aware, that has employed such techniques with (1) high resolution data over (2) large domains with (3) spatially explicit ground truth data at a large number of points within diverse canopy coverage areas (1862 points available for direct ground comparison

2.2   Methods
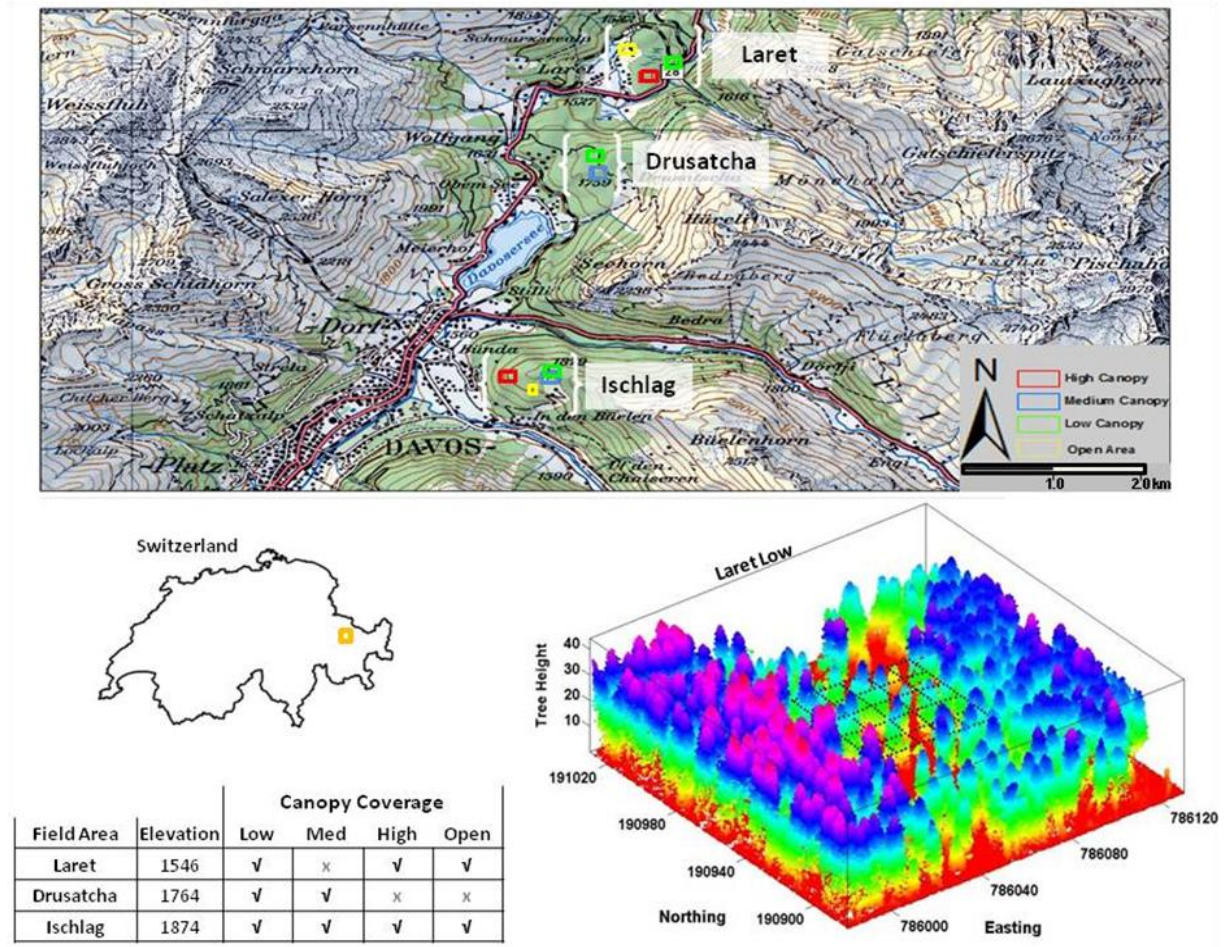
Figure 1. The study areas are located in various elevation bands and distinct canopy coverage regimes surrounding Davos, Switzerland. The upper map represents the aerial extent of the LiDAR dataset. The lower right box plot is a digital representation generated from the raw LiDAR data of the 'Laret low' field area with the geo-rectified sampling grid inside (276 points). The remaining 6 field sites have the same design setup. A hemispherical photo was taken at each internal grid crossing for a total of 16 photos per site as well as 10 auxiliary locations at three sites for the radiation measurement campaign.

A series of 7 forested field areas have been established for long term study in the region immediately surrounding Davos, Switzerland (Figure 1). Each field area was 50 m by 50 m and was located within three generalized elevation (low to high: Laret, Drusatcha, Ischlag) and canopy coverage (low, med, high) classes. Despite the generalized CC classification, each field area exhibited heterogeneous canopy coverages at the sub-plot scale (Figure 1) allowing for a multi-scale analysis on a broad range of canopy

classes. Field areas are characterized by low to no surface slopes with low surrounding terrain shading influences. Forest stands were predominately Norwegian spruce and varied in height from new growth up to 45 m in height with the majority between 10 and 30 m.

Field areas were set up in the fall of 2012 and are part of a long term forest snow hydrology study area operated by the WSL Institute for Snow and Avalanche Research (SLF). A distometer (Leica Disto X310) was used to calculate accurate (± 1cm) 10 m intervals for the positions of 36 intersection points at each field area, which were then marked with 2.4 m long poles. A nylon cord was fixed between all pole intersection points and 2m intervals were manually measured and marked along each of the six north-south and six east-west transects for a total of 276 points per site. A differential GPS (Trimble geo XH 6000) was used to arrive at coordinates of each internal pole point with a maximum error of ± 20cm. These coordinates were then distributed to all 2 m interval points with an estimated rectification error of ± 50cm. This gave a total of 1862 geo-referenced locations available across all field areas for direct ground comparison.

2.2.1   Hemispherical photos

Hemispherical photography utilizes a lens with an extremely short focal distance allowing for a broad field of view of approximately 180°. The field of view limit, with the camera directed upward, can reach the horizon and for processing purposes each point within the horizon's projected circle is defined by polar coordinates. The image angle corresponds to the azimuth, and the radius indirectly corresponds to the zenith angle. We took 16 hemispherical photographs at all primary intersection points within each field area for a total of 112 photographs (Figure 1). The photos were taken using a Canon 600D with a Sigma 4.5mm F2.8 EX DC HSM circular fisheye lens mounted on a specifically designed tripod allowing for quick leveling and directional setup to true north. Each photo was taken 1.2 meters above the ground surface in May 2013 under primarily low light conditions in order to maintain a good sky-canopy contrast. Underexposed photos were taken to get good contrast between the canopy and the sky. A point exposure measurement of the sky was first taken and this value minus 0.5 exposure stop was utilized for the setting.

2.2.2   Airborne LiDAR data

LiDAR data acquisition was carried out from the 11th to the 15th of September 2010 using a Riegl LMS Q 560 sensor from a series of helicopter flyovers at a nominal flying altitude of 700 meters for a total area of ~90km^2. The wavelength emitted from the Riegl device was 1550 nm with pulse durations of 5 ns and includes up to 7 returns per pulse with a maximum scan angle range of ±15°. The average point density of the full waveform data set yielded an average echo density of 35.68/m^2 of the flyover domain and 19.05/m^2 for the last returns within the utilized domain area. The affiliated digital terrain model (DTM) or the underlying ground surface elevations were computed by using the classified ground returns at a 0.5 m horizontal resolution by Toposys using their in house processing software, TopPit (http://www.toposys.com/).

2.2.3   Radiometer installation

An array of 10 radiometers (CM3 pyranometers: Kipp & Zonen) which measure the sum of direct and indirect shortwave radiation were deployed for 24 hour intervals at three field sites: Laret low, Drusatcha medium and Ischlag high. All sites demonstrate low terrain shading and are located at three elevation and canopy closure regimes (see Figure 1). Each radiometer was fixed approximately 10 meters to the north, south, east, west, northwest, northeast, southwest, and southeast respectively from a center point, which was also equipped with a radiometer. The final or tenth radiometer was set within a canopy closure regime that was not captured with the others. The circular array was set in a specific position within each of the three field areas to capture as much canopy heterogeneity as possible while retaining a generalized canopy regime representative of the entire site. Like the predefined site grids, all points have been geo-referenced and an affiliated hemispherical photo was taken at the exact point where each radiometer was placed. Each campaign was carried out during 100% visual clear sky conditions from sunrise to sunset on the 14th of August 2013 for Drusatcha medium, 22nd of August 2013 for Ischlag high and the 3rd of September 2013 for Laret low. The 15 second output format from the radiometers were then aggregated for 10 minute intervals.

2.2.4   Polar coordinate conversion

In order to incorporate a point based angular viewpoint into LAI, CC and PISR calculations, raw ALS data

was converted into a spherical coordinate system where the traditional Cartesian coordinates, X, Y, and Z

were converted into a distance from the origin to the point (R), the inclination or polar angle between the

zenith and a projected ray from the origin to the point (θ, theta) and the angle between the positive x axis

and the x/y plane (Φ, phi). A significant amount of pre-processing was initially required in order to use the

point cloud data and represent this data as hemispheric images. All holes within the DTM (terrain surface

below the canopy) were first filled using a triangular based interpolation. Elevations from the raw data were

converted into canopy heights by taking the difference between the raw point cloud elevations and the

DTM. Any canopy heights below 1.2 meters, representing the acquisition height of the hemispherical

images, were removed. Φ was calculated from 0 to 90 degrees for a full 180 degree view frame. The θ

values were then flipped on the east-west to mimic the upward viewing projection of hemispheric photos.

Despite some prior work demonstrating that inclusion of data with distances greater than 50 meters

accounted for no significant correlation increases, no data with horizontal distances less than a 100 m

distance from the origin were removed in order to ensure all relevant information is preserved regardless of

site specific vegetation heights (Alexander et al. 2013). Polar coordinate plots (as an example, see figure 2)

were then created at (1) all points where hemispherical photos were taken within the field areas and (2) at

all points on each sampling grid per site (1932 points) and saved as image files.
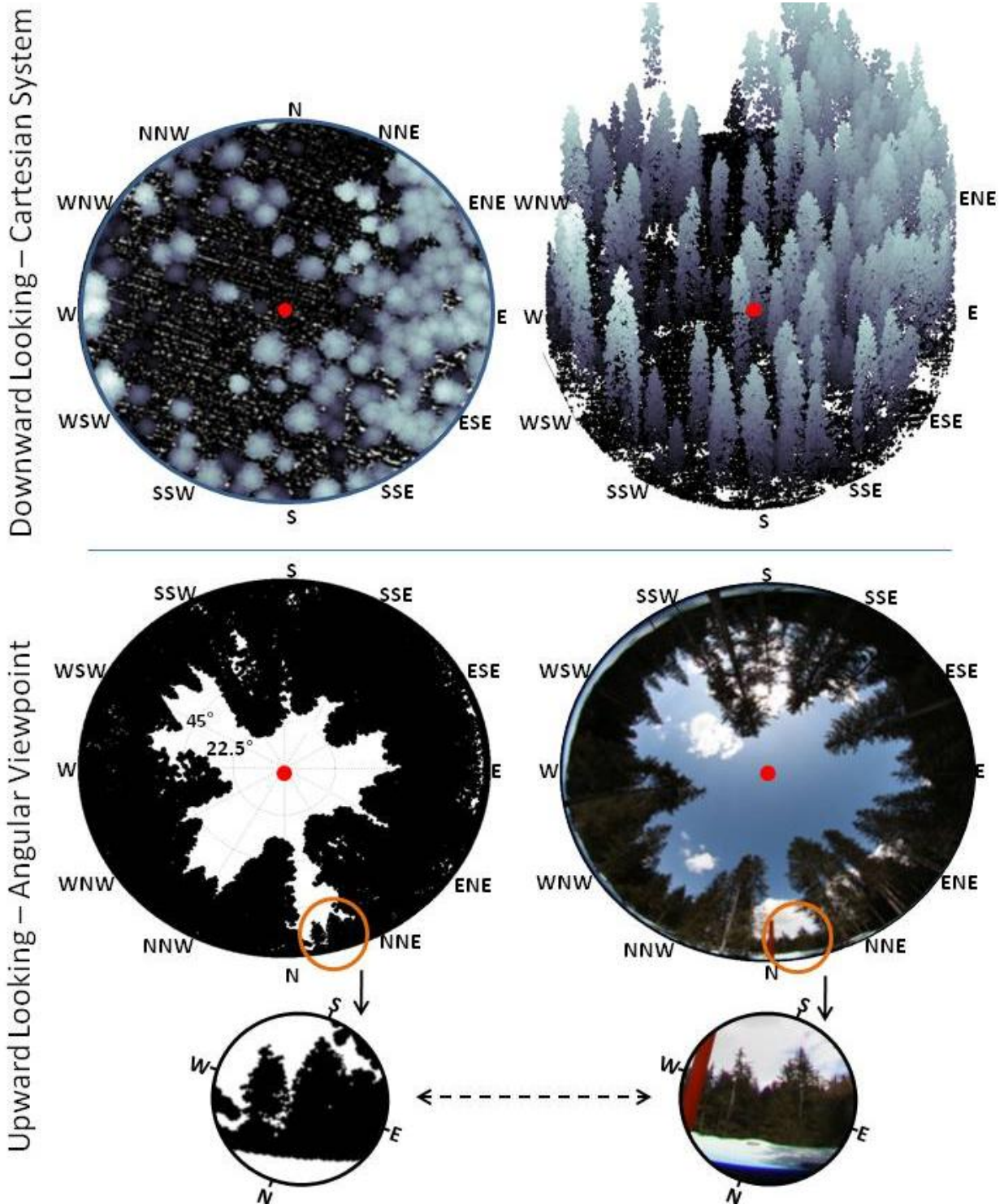
Figure 2: The standard overhead Cartesian viewpoint from the LiDAR is displayed on the upper tiles. The lower tiles are representations of an angular viewpoint where a hemispherical photo is displayed on the right and a synthetic hemispherical image (Polar projection system) on left with distance integrated pixel print size. Canopy points closest to the origin are represented as large pixels and points further away as small pixels. Bottom images are zooms of canopy characteristics on the horizon. All images are from the same point (Laret Low field area) and integrate a data trap size of 100 meters. The point of acquisition is labelled as a red dot in the middle of each image. Note the large geometric projection differences between the Cartesian system (upper tiles) and the polar system (bottom left lower tiles).

Successful imitation of hemispherical images required several assumptions regarding point size output of the synthetic images. An initial analysis was performed which explored how to introduce distance into the images, i.e. how should a tree at the maximum horizontal distance limit (100 meters) be compared to a tree seen near the origin. Several varying point projection algorithms were created for the data set, including (1) a fixed output point size, (2) variable output size based on horizontal distance to point and (3) variable point output size based on distance to point. The optimal output was determined by a sensitivity analysis which was optimized by comparing the correlation between effective LAI as well as CC from the synthetic and real images. The best fit was obtained by distributing the point cloud output into a printed circle with the size directly based on the distance from origin (R). The print size of the circle was linearly interpolated from near to far (Figure 2, lower left tile). The process was automated allowing for almost immediate production of 112 synthetic images at the exact coordinates as the actual images as well as production of images at each of the labeled points within the 7 field areas for a total of 1932 synthetic hemispherical images. This process has also been created to facilitate extension to other data sets in order to explicitly arrive at synthetic hemispherical images within an ALS dataset domain based solely on a coordinate input list.

2.2.5   Estimation of LAI and canopy closure with an angular approach

The HP and synthetic photos were analyzed by 'Hemisfer,' version 2- beta, an image analysis software developed at the Swiss Federal Institute for Forest, Snow and Landscape Research WSL (http://www.wsl.ch/dienstleistungen/produkte/software/hemisfer/, Thimonier et al., 2010). This software was used to obtain effective LAI, CC and PISR. These calculations are based on the classification of pixels as either white (sky) or black (canopy) by applying a brightness threshold to the analyzed picture. Thresholding of real photographs was carried out according the algorithm of Nobis & Hunziker (2005) integrated in Hemisfer, taking into account the gamma value ($\gamma = 2.2$) of the pictures. In some pictures (dependent upon the contrast) the blue color channel was used in order to improve the contrast between the sky patches and the vegetation. Light transmission, T, was then calculated as the proportion of white pixels within analysis rings, with the rings defined as ranges of zenith angles θ (theta) in 15° steps. The

contact number, K, or average number of times that a straight line would touch the canopy over a distance equal to the thickness of the canopy was calculated as a function of the zenith angle and light transmission:

$$K = -\cos \theta \ln T \qquad \text{eq. (1)}$$

The K values were then integrated over rings of various θ angles to obtain effective LAI in accordance with a standard technique first introduced by Miller et al. (1967). No clumping correction was applied (for the sake of simplicity LAI represents effective LAI within this paper). Canopy closure was calculated as the average of the T (θ) values, weighted by the solid angles of the corresponding rings.

2.2.6   PISR

The potential incoming solar radiation under the canopy (PISR) was calculated from analysis within the Hemisfer program with the transmission of the direct and diffuse components through the canopy structure represented by each real or synthetic picture. Modeled clear sky and real sky conditions were utilized to partition the atmospheric direct and diffuse radiation parameters. While the clear sky conditions better mimic potential incoming solar radiation it was also necessary to include a 'real' sky condition when estimating solar radiation over larger time scales when specific diffuse and direct parameterizations are variable. To partition the real sky conditions over the whole year the average values specified by Timofeyev & Vasil'ev (2008) were used where the direct and diffuse radiation parameters were set to 25% of the solar constant. The clear sky conditions specific to the field areas as well as our radiometer campaign dates were utilized and made available at 15 minute intervals from the photovoltaic geographic information system project (PVGIS) within the European commission joint research center, Institute for Energy and Transport (http://re.jrc.ec.europa.eu/pvgis/solres/solres.htm, Huld et al. 2008)). This time series was further interpolated to match the 10 minute output data of the radiometers.

The calculations within Hemisfer were carried out in 1-minute steps according to the position of the sun in the sky, taking the slope and exposition of the plots into account (Schleppi and Paquette 2013). PISR values obtained for a period ranging from January 1st to December 31st and were aggregated per 10 minute time step. The estimated PISR values from the real and synthetic images on the corresponding day of the radiometer campaign were utilized for direct comparison to the radiometer measurements.

2.2.7   Estimation of LAI and canopy closure within the Cartesian system

Effective LAI and CC were also calculated from the raw ALS data without a coordinate transformation and used as comparative tool for the estimates from the synthetic images. Canopy closure was calculated by first converting all returns from the point cloud into a 0.5m grid and then quantifying the ratio of cells which have canopy cover to the total number of cells within the digital surface model. A LAI proxy was estimated by computing the ratio of all raw LiDAR first returns to total ground returns and was derived from a modified routine initially utilized by Morsdorf et al. (2006) and recommended within the ICP manual for methods and criteria of forest monitoring which analyzes LAI as a ratio of return hits (Fleck et al. 2012; Morsdorf et al. 2006; Solberg et al. 2009). Both metrics were calculated using a height cut-off and a data trap area, where
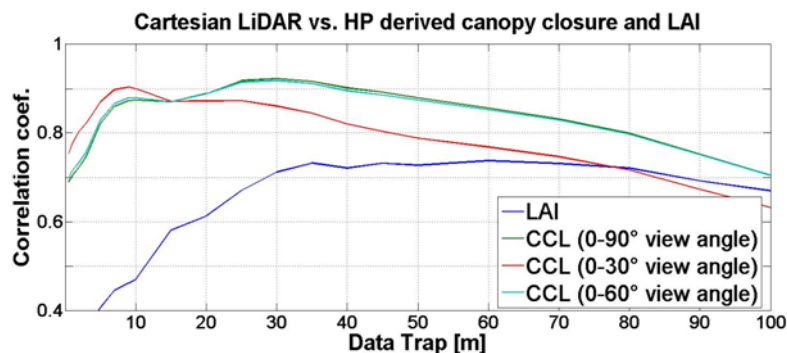
Figure 3. Correlation between HP and LIDAR (Cartesian coordinate system) derived LAI and CC. Varying data trap sizes of the aerial LiDAR data were utilized and analyzed for correlation to the HP values. Three viewing angles from 0 to max or 90° within the HP data, representing the differing zenith angles of the hemispheric photos were also compared with the CC derived from the Cartesian system. The best correlation is for a 90° viewing angle with a trap size of 30 meters for CC, while LAI necessitated a slightly larger data trap of 35 m for the best correlations.

the height cut-off is preset to the height of the field collected hemispherical photos (1.2 m). In this case, the data trap size represents the distance away from the analyzed point with the point located in the center. The data trap was initially left flexible where a sensitivity analysis of the CC and LAI output from the hemispherical pictures were compared to the ALS data and optimized based upon correlation between the datasets (Figure 3). Estimating parameters in this manner does not utilize a point based angular viewpoint, compared to estimates from a HP approach, (Figure 2) creating difficulties in direct comparison of both methods. If the data trap is sufficiently small, then only canopy cover, which is a measure of canopy from a specific ground point to the matching overhead point, not canopy closure values can be derived. Canopy closure values however are a measure of canopy from a point to an area (Fiala et al. 2006). Due to this viewpoint discrepancy, CC values were also derived from the HP at three different zenith windows: 0° - 30°, 0° - 60° and 0° - 90° for comparison (Figure 3). Figure 3 represents the initial sensitivity analysis which demonstrated that the full frame of view available from HP (0-90 degrees from the zenith) delivered the best results when compared with LiDAR derived CC and LAI output from an analysis bounding box size of at least 30 meters. The correlations slightly dropped when smaller viewing angles from the HP's CC derivation were analyzed. The optimal data trap size for LAI, however, was slightly higher at 35 meters. The correlations for both parameters, but especially for LAI, were low with small data bin sizes and not until the data trap sizes increased significantly were reasonable correlations seen. However this range will always depend on both the vegetation density as well as the vertical canopy height at each site (Morsdorf et al. 2006). This range also depends on the line of site obstruction of data as viewed from hemispherical photos. These occlusions can be seen within Figure two, if the top left and bottom left panels are compared. The visual scale inequalities between the two systems (Cartesian and polar) also highlight the data representation differences. The differences emphasize the utility of the Cartesian system may be better suited for spatial averages where point estimations are better relegated to an angular or polar approach. Only the estimates of LAI and CC garnered from the optimized bounding box sizes were then used as a comparative tool for the results from the synthetic hemispherical images. As with the parameter

investigations in the polar coordinate system, all aspects of the analysis have been automated and can be extended to other LiDAR data sets.

2.3 Results and Discussion

2.3.1 Synthetic image LAI and CC derivation vs. hemispherical photographs
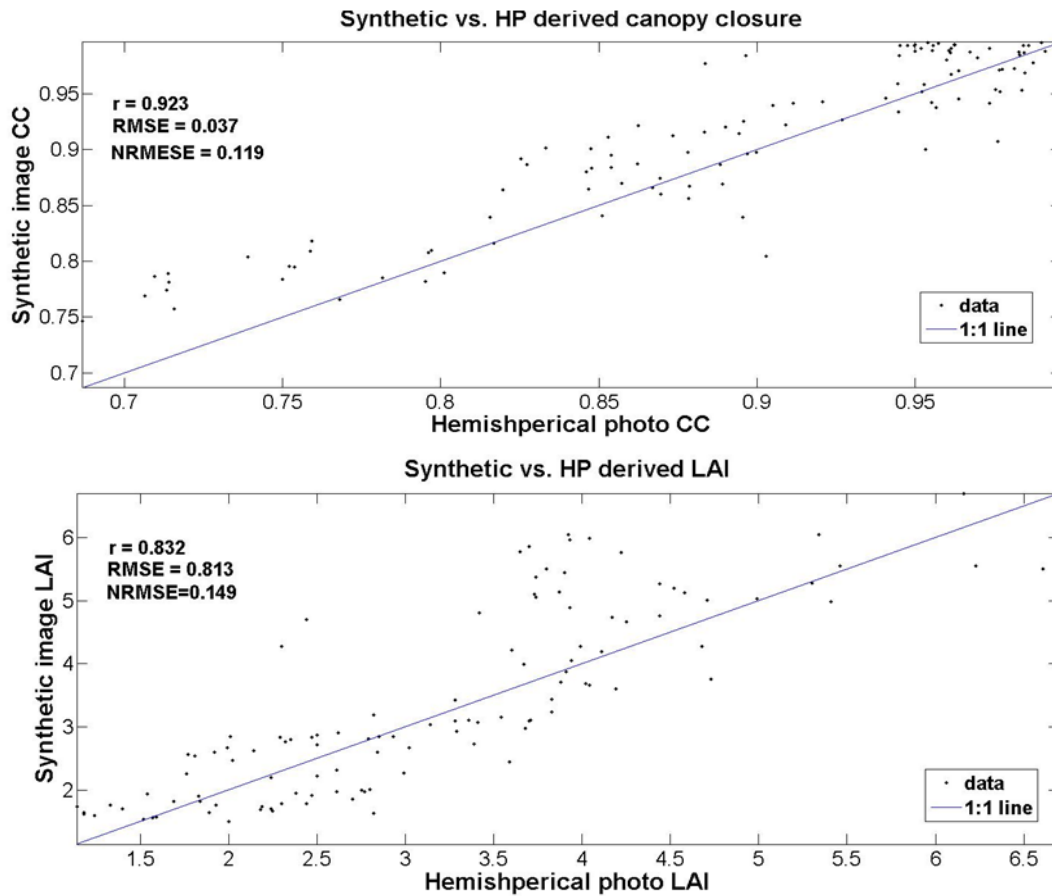
Figure 4. The upper graph compares CC derived from synthetic images on the y axis with HP calculated CC on the x axis. The lower graph compares LAI derived from synthetic images on the y axis with HP calculated LAI on the x axis. The 1:1 line is displayed on both graphs as a solid line. Both metrics display good correlation between methods with correlation coefficients of 0.92 and 0.83 and normalized RMSE's of 0.12 and 0.15 respectively.

The sensitivity analysis of the printed point size distribution within the synthetic images was optimized and gave a best fit when a linear interpolation utilized a point size distribution of 7 to 0.5, where the closest
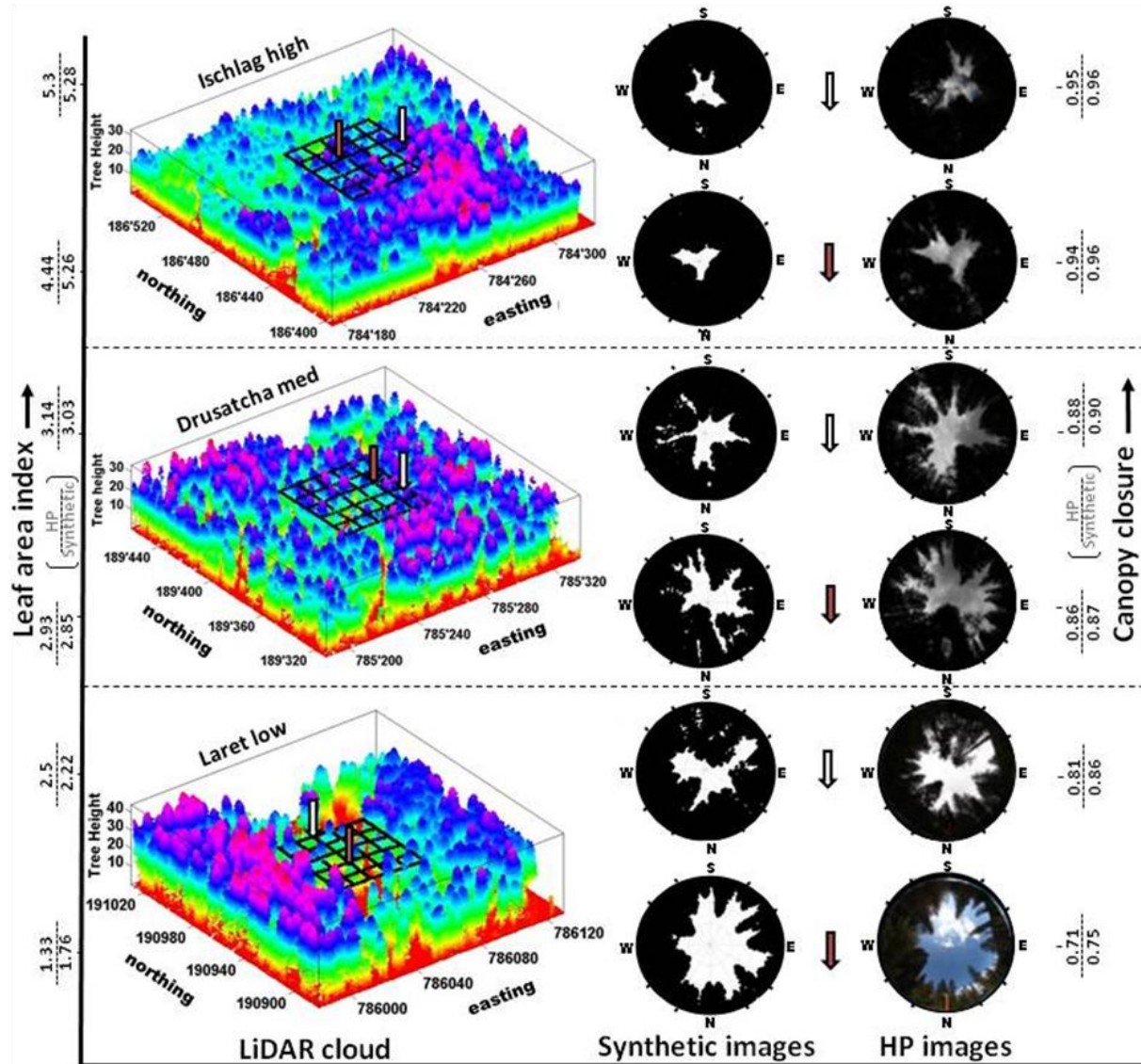
Figure 5. Examples of synthetic images from three field sites representing low canopy, medium canopy and high canopy closure (in the middle column) which range in LAI from 1.76 to 5.28. The y axis increases in canopy closure and LAI values with the top number being values calculated from HP and the lower number being estimations from the synthetic images. The left column contains LiDAR data cuts of 150 x 150 meters for three field areas from low to high canopy cover. The internal black lines represent the sampling grid (50 x 50m) where the hemispherical photos were taken. On the grid, two arrows represent the synthetic and HP locations. The right column holds the hemispherical photos.

points were given a print output of 7 and the farthest points were given a point size of 0.5. As seen in Figure 4, LAI and CC from the synthetic images showed good correlations and low bias when using this interpolation scheme. Results of this run gave correlation coefficients of 0.83 and 0.93 respectively when

compared to HP output. The correlations remained high for the extent of the series which range from very open areas to extremely closed forests with LAI values ranging from ~1 to 7. Figure 5 gives a series of examples of HP and synthetic photos at different canopy closure regimes, ranging from 0.75 to 0.96 within 3 distinct field sites. Due to the small size of the images, it is hard to visualize small canopy scale correlations from the point size distribution, but trends within the different gaps sizes are clearly visible. For a visual overview of smaller scale correlations see Figure 2.

2.3.2   Cartesian system LAI and CC derivation vs. hemispherical photographs

CC and LAI derived from the Cartesian system also provided reasonable correlations between the data series. Correlations of CC derivation in the Cartesian system (r: 0.91) were within 1% of the estimated CC correlations from the synthetic images (r: 0.92). LAI estimation correlation was 0.73 for the series and represented a 10% reduction when compared to the correspondence between the synthetic and HP images (r: 0.83). The CC estimates functioned reasonably well through the entire series from low to high canopy cover values. The LAI estimates also functioned reasonably well, but only on the lower end of the range (LAI ≤ 4). When HP LAI values were greater than 4, the Cartesian derived estimates became saturated and failed to estimate higher values (Figure 6). The greatest differences, however, did not reside with the correlation coefficient values. All values were systematically biased and necessitated a basic regression correction to arrive at the correct values. This bias has been seen in prior studies and can be manipulated based on the return echo utilized. However the interplay between return echo and CC bias is still unclear because it depends on the sensor used, the underlying vegetation and the echo detection method (Morsdorf et al. 2006). Due to this ambiguity all return echoes hitting above the height threshold (height at which the hemispheric photos were taken) were utilized. ALS data in this system provided a nearly vertical downward view and the offset of the CC values also highlighted the inherent differences in comparing a point based angular derived output with that of a area averaged planar one. Despite the integration of large data traps (as described in section 2.2.4), which indirectly integrated an angular approach, it is clear that it was still not sufficient when comparing the results to an angular one. The LAI proxy estimates on the other

hand were estimated by directly analyzing the ratio of initial returns (which represents outer canopy hits) to total ground returns. This proxy ratio will always be offset and necessitate local scaling to agree with the HP values. The non-linear distribution of these echoes also affected the estimation power of the dataset at higher LAI values due to saturation effects of the echoes (Figure 6 lower panel).
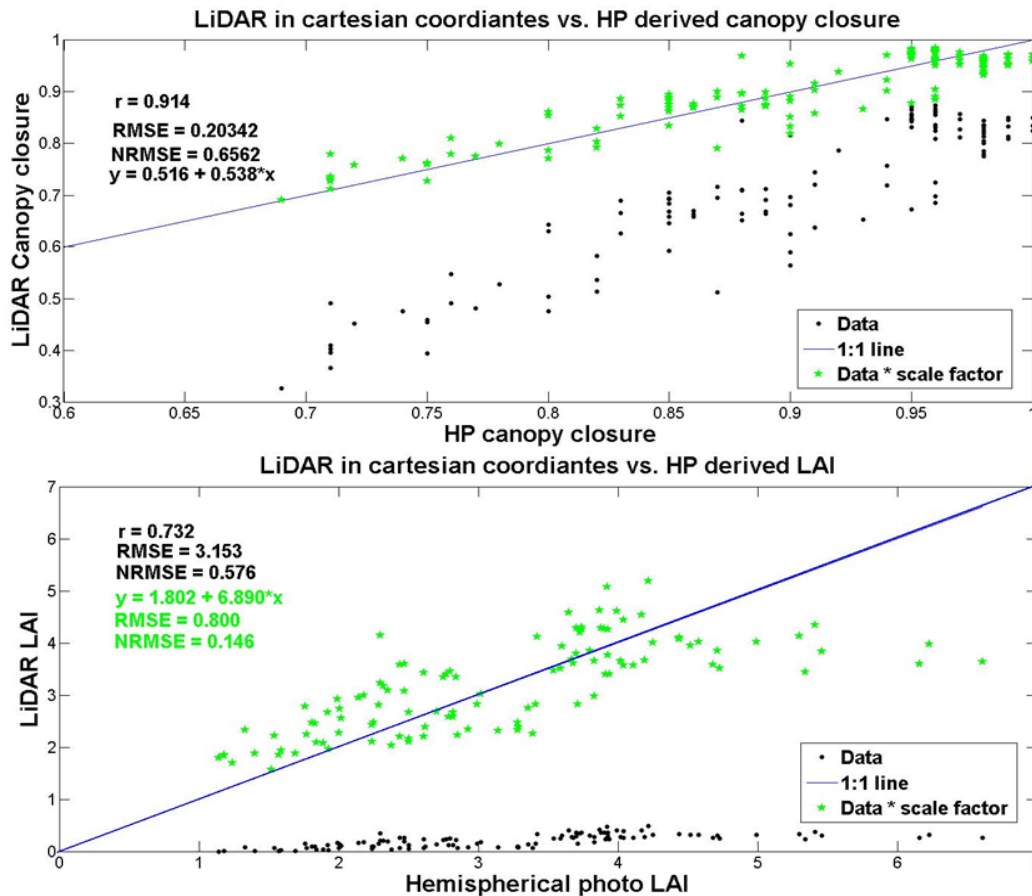
Figure 6. The upper graph compares canopy closure derived from LiDAR in the Cartesian system on the y axis with HP calculated canopy closure on the x axis (black). The correlation is within 1 percent of that of the values derived from synthetic images. However the values are systematically biased necessitating a basic regression to obtain comparable estimates (green). The lower graph compares LAI derived from LiDAR in the Cartesian system on the y axis with HP calculated LAI on the x axis (black) where the correlation is 10 percent lower as compared to that of the values derived from synthetic images. A basic regression is also necessary to arrive at comparable values (green). The LAI correlation with this approach also degrades with values above 4. In both charts, the black dots represent the initial estimates and the green stars represent the regressed values.

While forest metric processing in the Cartesian system from this data set display clear advantages over HP use in terms of time consumption and the ability to explicitly arrive at metrics for large areas, its utility and performance was still reduced when comparing this to the synthetic image processing. Specifically, Cartesian based LAI estimation gives no visual output aid to qualitatively asses the output and, at least with this dataset, difficulties arose when calculating LAI within dense forest areas (LAI >4). Both LAI and CC necessitated a scaling factor to compare with HP output whereas the synthetic images could be directly optimized from the point size output manipulation. The synthetic images allowed for a visual record of the geometry, where at a quick glance one could get a good idea of the overlying forest structure for various points. LAI and CC were estimated with higher precision for the entire data dataset range as compared with the Cartesian approach. These differences imply that the point LAI and CC estimations are better estimated using a polar system whereas the utility of the Cartesian system may be better suited for spatial averages.

2.3.3   PISR comparison

PISR was initially calculated from the HP and synthetic images within Hemisfer by adding both the diffuse and indirect shortwave radiation components. The 10 synthetic images per site were parsed into ten minute and one hour time step averages. This data was then used to directly compare with the 24 hours of data from the radiometer campaigns for (1) individual radiometers as well as (2) field site composites (average of 10 radiometers per site).

The field site composite comparisons of the synthetic and radiometer data show correlation coefficients ranging from 0.90 to 0.94 at one hour time steps and 0.73 to 0.83 for 10 minute steps with similar correlations seen within the HP photos (Table 1). The individual point comparisons using the synthetic images gave average correlations of 0.72 for the 1 hour data series and 0.51 for the 10 minute data. Figure 7 shows three individual point comparisons at varying canopy cover regimes at 10 minute intervals within each of the radiometer campaign sites where the correlation ranged (from the synthetic images to radiometer measurements) 0.70 to 0.88 with an average normalized RMSE of 0.264. The general timing and peak trends of PISR was well represented within the 10 minute synthetic data series at the point scale.

However the bias of the direct radiation component increased with increasing canopy closure values canopy (starting at CC values of 0.85), and caused a reduction in peak radiation estimation within the synthetic images which had CC values ≥0.85. This was readily apparent at the high canopy density site, Ischlag high, where the direct component of solar radiation was not fully captured (Figure 7 top graph). The HP series also demonstrated similarly good correlations; however the goodness of fit showed no link to increasing canopy closure. Figure 9 column 'a' show site comparisons of synthetic data at hourly time steps. This data also captured the timing and peak trends of both the diffuse and direct shortwave radiation component at all sites, but like the point data series, the Ischlag high field sites demonstrated a reduction in the direct component correlation with the radiometers. The data fits maintain high correlations, but the comparisons demonstrated increasing biases (Figure 8) with increasing canopy closure as previously described with the point comparisons.

Table 1. Correlation coefficients, RMSE's and normalized RMSE's of all radiometer measurements as compared to the estimated values from (a) HP photos, (b) synthetic images and (c) synthetic images with a rescaling function at each radiometer campaign field site. The values in bold are from 1 hour composites and the values in dark grey are from 10 minute averages.

(**1 hour avg** / 10 min avg)		R	RMSE	NRMSE
Laret Low	HP photos	**0.918 / 0.823**	**67.52 / 103.04**	**0.147 / 0.21**
	Synthetic images	0.897 / 0.784	84.00 / 114.70	0.449 / 0.415
	Synthetic images with rescaling function		80.93 / 113.00	0.176 / 0.225
Drusatcha medium	HP photos	**0.922 / 0.858**	**43.59 / 60.24**	**0.124 / 0.149**
	Synthetic images	0.942 / 0.833	58.26 / 73.22	0.85 / 0.736
	Synthetic images with rescaling function		41.27 / 68.01	0.118 / 0.168
Ischlag high	HP photos	**0.84 / 0.636**	**8.163 / 14.36**	**0.263 / 0.197**
	Synthetic images	0.898 / 0.739	14.622 / 95.77	0.528 / 0.131
	Synthetic images with rescaling function		5.354 / 15.91	0.163 / 0.237
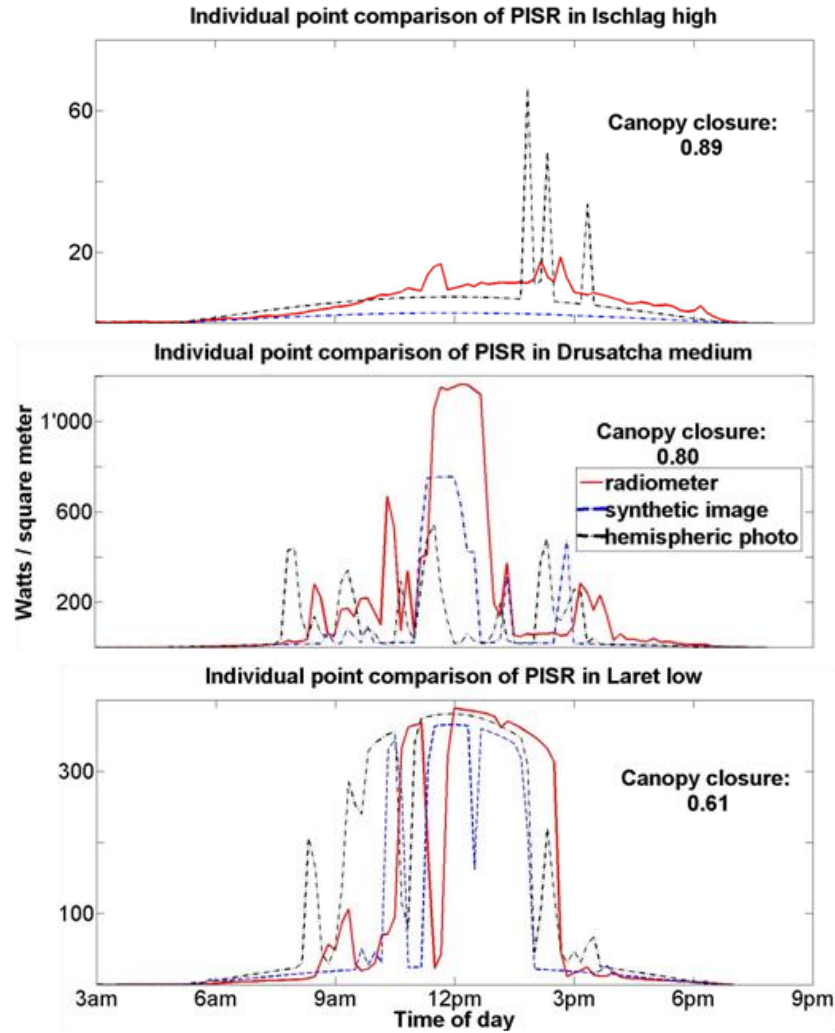
Figure 7. Comparison of 10 minute average radiometer (red), hemispheric photo (black) and synthetic image (blue) data for individual points with different canopy closure values. From low to high: (1) Laret Low (2) Drusatcha med and (3) Ischlag high field areas. The modeled data utilized the PVGIS direct and indirect shortwave radiation partitioning for clear sky global irradiance in Davos Switzerland for the radiometer campaign dates.
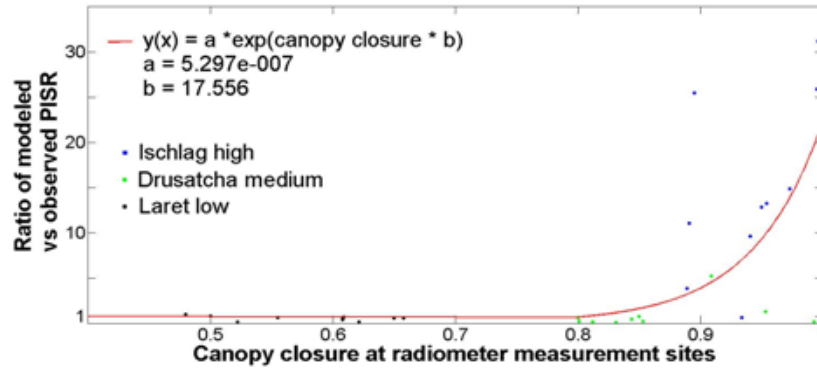
Figure 8. The offset of PISR estimations from the synthetic photos to the radiometer measurements (y-axis) were plotted as a function of canopy closure (x-axis). Site locations of each of the 10 radiometer points are labelled with different colors. As canopy closure increases beyond 0.85 an exponential relationship was used to describe the interaction between ratio and canopy closure (red line). A value rescaling algorithm was created from this relationship and applied to all synthetic photos at each field site.

Calculations of total offset of estimated PISR from the synthetic images to the radiometer measurements at all points (total of 30) were plotted against canopy closure (also calculated from the synthetic images) and an exponential relationship was defined between the two when canopy closure values increase above 0.85. See Figure 8. This relationship was then applied to the field estimations seen in column 'a' of figure 9. The same comparison was made utilizing the HP data series and a similar trend between the offset of modeled and observed PISR vs. canopy closure was seen until the closure values increased above canopy closure of ~0.85, where no rising limb was seen. Since this exponential relationship was not visible within the HP photo data series, it seems likely this offset within some of the synthetic images was due to the thick cover integrated into the synthetic images as overlapping pixels which reduced simulated solar beam transmittance. While the point size distribution worked well for the duration of the data series for CC and LAI, it is hard to avoid overlapping pixels at not just dense areas but also at the perimeters of the pictures. Even though smaller pixels were assigned to these distant points, the high amount of returns within dense canopy can falsely remove small gaps within the canopy. However, the predefined linear point size distribution size (see section 2.2.1) did not seem to be the only constraining factor. The simulations from the hemispherical photos showed no reduction in bias at the high density sites but a small decrease in

correlation with increasing canopy cover. This is hard to decipher because the radiometers utilized did not separate the diffuse and direct portion of the radiation creating difficulty in a full analysis of the PVGIS modeled clear sky portioning scheme utilized in the radiation partitioning. Nonetheless, the predictive power of the HP and synthetic photos maintained a good fit and necessitated no scaling function for any points with canopy closure below 0.85.

Yearly synthetic PISR estimates were also derived for (1) all points within each sampling grid of the solar radiation field areas, 276 points per site ($\frac{276}{(50m)^2}$), (2) at all primary intersection points within each field area, 16 points per site ($\frac{16}{(50m)^2}$) and (3) at the center of each field area ($\frac{1}{(50m)^2}$). In these cases, the generalized real weather direct and diffuse radiation partitioning coefficients from Timofeyev & Vasil'ev (2008) were utilized. These factors do not give a clear sky condition like the time series data from the PVGIS model utilized within the direct radiometer comparisons. Instead, they give an average partitioning value and are thus more accurate over time. The yearly under canopy PISR estimations ranged from ± 8% to ±78% between scales ($\frac{1}{(50m)^2}$: $\frac{16}{(50m)^2}$: $\frac{276}{(50m)^2}$) with an average scalar difference of approximately ±50%. The results can be viewed within figure 9 as a yearly radiation regime along with the yearly averages displayed on each graph. This demonstrates the extreme variance of radiation regimes underneath forest canopy and emphasizes the necessity of explicit radiation regime estimates at fine scales.

Estimated yearly radiation regimes from synthetic images

1 day field campaign data comparison
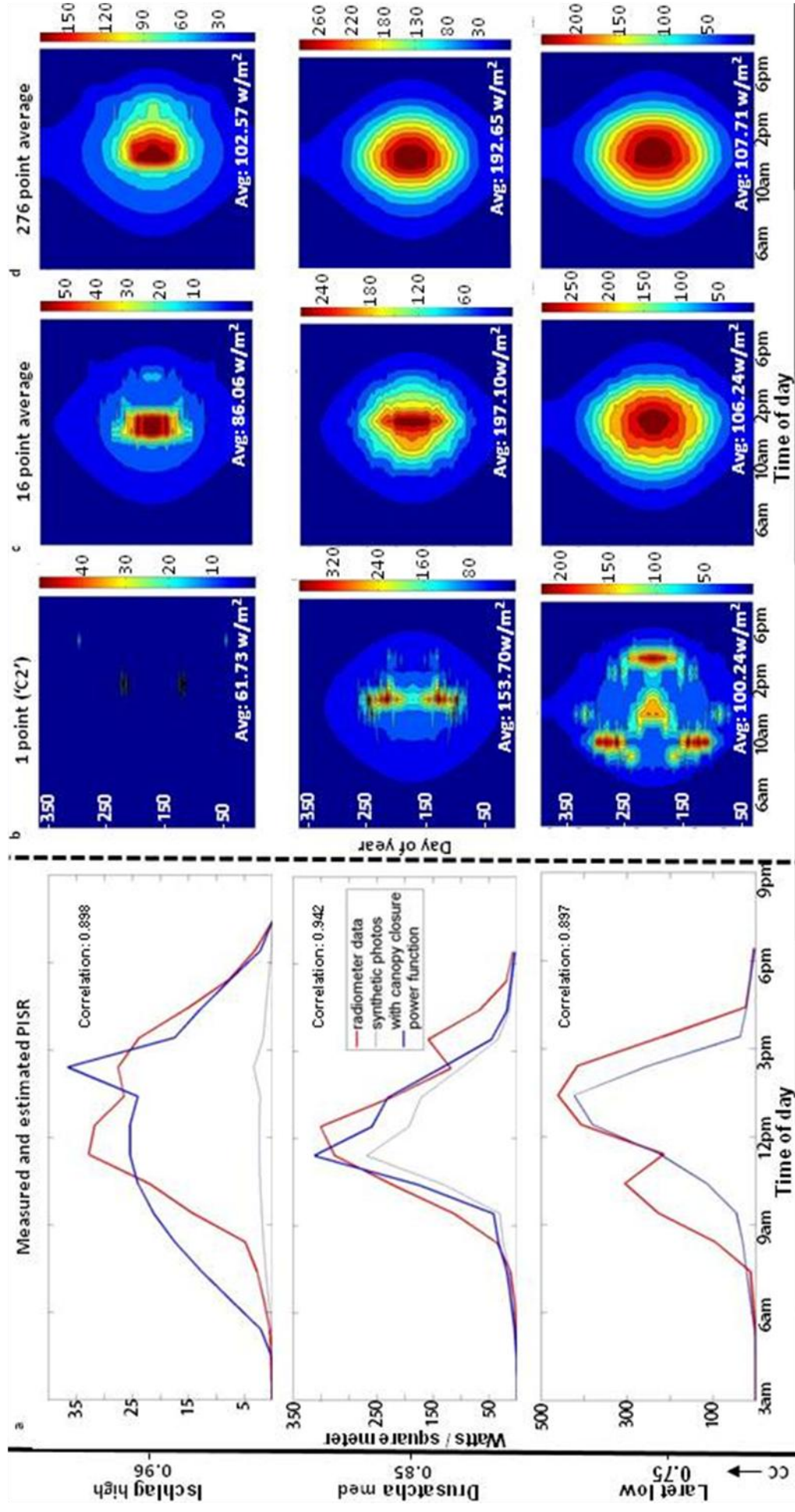
Figure 9. The y axis represents data from low to high canopy closure with average field site values seen beside each field area name. Column 'a' shows a direct comparison of average hourly values from the 10 radiometers (red) at each field site and the estimated values from the 10 synthetic images (thin blue) as well as a value rescaling algorithm (thick blue) as a function of canopy closure applied to the initial estimates which had canopy closure values greater than 0.85. The initial estimates utilized the PVGIS direct and indirect shortwave radiation partitioning for clear sky global irradiance. The correlations between the synthetic photo estimates and the radiometer values can be seen in bold. The subsequent columns (b,c,d) show estimated yearly radiation regimes from the field areas (w/m2)derived from synthetic images utilizing the generalized radiation partitioning values from Timofeev and Vasil'ev. Column 'b' is an estimation from one point (at the approximate center of field area –point C2). Column 'c' is an average of 16 values from all primary intersection points within each field area. Column 'd' is an average of 276 values from all sampling points within each field area. Average daily values are calculated from sunrise to sunset. Note the discrepancy within values lending emphasis to high resolution data extrapolation.

2.4 Conclusion

LAI and CC could be accurately predicted at high resolution and low bias across all canopy coverage conditions using the synthetic images and displayed several improvements over that of the Cartesian system estimations when using this data set. The synthetic images were able to estimate both metrics from low to high generalized canopy coverages where the standard Cartesian coordinate system (with our approach) was not able to effectively predict LAI at values above 4. The synthetic images also allowed for an initial visual analysis to qualitatively analyze the validity of the estimated metrics as well as allow for a visual comparison to hemispherical photographs. The Cartesian system demonstrated universal biases of estimations and required a basic regression to arrive appropriately scaled values. Furthermore, this bias correction was still not able to accommodate for improved accuracy of LAI values above 4. The synthetic images demonstrated improved correlations and normalized RMSE's for both canopy metrics (r: 0.93 for CC and r: 0.83 for LAI) and required no data scaling. Scalar inequalities (figure 2) between the Cartesian system, where canopy elements are averaged over an area, and the point based polar system integrate canopy components in different manners. These differences can be seen within the results and imply that the LiDAR integrated with Cartesian system may be better relegated for spatial averages whereas synthetic images from LiDAR data may be better suited for point estimations.

Both methods can be utilized with different datasets; however production of synthetic images will require a re- analysis of the point size distribution if datasets with a different average echo density are utilized as this is an indirect function of the overall density of the LiDAR dataset. It is possible that future work can integrate point cloud density into point size distribution for a general scaling function for all data sets. However, it should be cautioned that with less dense point clouds more thought is needed to arrive at a distribution due to the non linearity between the landscape and the photo output when using a hemispherical lens. This suggests that for a general point size distribution equation to be formulated, focal length must also be integrated into the distribution function for lower resolution data sets. Integration of the LiDAR return type may also prove to be an important factor in creating a universal point size distribution.

Despite this initial hurdle, when the appropriate point size distribution was found, this method was able to predict LAI and CC over the entire dataset domain across all possible canopy density conditions without a subsequent regression to account for the scaling or estimation differences.

PISR was also precisely estimated from the synthetic images with average site correlations ranging from 0.90 to 0.94. This method allowed for flexible direct and diffuse incoming radiation partitioning dependent upon the day and point in space analyzed. However at canopy closure values greater than 0.85 the direct radiation component was underestimated from the synthetic images and necessitated an exponential scaling function based on canopy closure. This emphasizes the need for extended research regarding an improved method for scaling the printed point size distribution of the synthetic images in order to resolve the need for a canopy density based scaling function to better transfer these methods to other LiDAR datasets with non-concurrent point cloud sizes.

Despite potential problems with automatic transference of the results to other datasets, the results prove to be extremely promising for high resolution derivation of canopy and solar radiation metrics. The ability to accurately infer these parameters explicitly on very small scales has major implications for snow modeling within forested areas. Canopy interactions and solar radiation under the canopy influence snow cover, snow depth and snow density at sub-m scales. This small scale heterogeneous behavior creates intrinsic difficulties when forest snow processes are generalized within larger scales. A good example can be seen in figure 9 where average PISR values at three different field areas are derived for a point, and for an ensemble average of 16 and 276 respectively. The major difference between these values (± 8% to ±78% differences with an average of ±50%) highlights the need for explicit high resolution parameter estimation within heterogeneous canopy coverages. The ability to model these factors for any point where LiDAR data of sufficient resolution is available can allow for better parameterizations of forest snow mass and energy balance models. This can permit more detailed analyses of large scale forest snow hydrological issues that were previously impossible before the availability of such datasets.

Acknowledgments

Novel Forest Structure Metrics from Airborne LiDAR data for improved snow interception estimation

D. Moeser[1,2], F. Morsdorf[3], T. Jonas[1]

[1]WSL Institute for Snow and Avalanche Research SLF, Davos Dorf, Switzerland
Tobias Jonas: jonas@slf.ch

[2] Forest Ecology, Institute of Terrestrial Ecosystems, Department of Environmental Sciences, Swiss Federal Institute of Technology ETH, Universitätstrasse. 16, CH-8092 Zurich, Switzerland

[3]Remote Sensing Laboratories, Department of Geography, University of Zurich, Switzerland
Felix Morsdorf: felix.morsdorf@geo.uzh.ch

Abstract

A set of 57 novel canopy metrics of potential value for snow modeling were created from airborne LiDAR data. The metrics were meant to estimate size and relative location of gap openings around a point within forested areas, allowing for measures of the spatial arrangement of surrounding canopy elements. These new metrics were correlated with snow interception measured in the field (8488 manually measured snow interception points). The results were further compared to the correlation values between effective interception and traditionally used forest parameters (CC, LAI). The correspondence between all metrics was also analyzed in order to understand the potential cross correlation between each variable. LAI (average R: 0.57) demonstrated low correlations when directly compared to snow interception and further showed a large cross correlation with canopy closure (average R: 0.72). A new metric, 'mean distance to canopy' had the highest correlation (average R: 0.78) over all storm events to the effective interception. But in contrast to LAI, this metric did not show any cross correlation with canopy closure (CC). Likewise, 'total gap area,' an indirect measurement of

apparent gap fraction (another new metric), also showed a high correlation to effective interception (average R: 0.72) without demonstrating a significant cross correlation to CC or to mean distance to canopy. These findings suggest that modeling forest snow processes with both CC and LAI may not be the best option due to both the low correlation of LAI as well as high cross correlation between these parameters. However, the pairing of mean distance to canopy and/or total gap area with canopy closure could give more robust estimations of snow interception within heterogeneous terrain

3.1   Introduction

The hydrology of forests plays an important role in the global water budget. Snowmelt dominated watershed headwaters which contain forests produce 60% of the global freshwater runoff (Chang, 2003). Forest canopy structure greatly influences snow accumulation and melt and controls water availability from forested areas. Specifically, the surrounding forest structure can influence involved physical processes, creating much greater spatial snow pack heterogeneity compared to open areas. Snow interception, a major driver of heterogeneous snow distribution, ranges from low to just over 60% of total annual snowfall (Montesi et al., 2003; Storck et al., 2002).The importance of snow interception within forest canopies has not gone unnoticed within the hydrology community. There is a growing body of work spanning 75 years which described attempts to directly quantify and model forest snow interception (Hedstrom and Pomeroy, 1998; Satterlund and Haupt, 1967; Scmidt and Gluns, 1991; Varhola et al., 2010b). These studies highlight the complex interplay between the physical under-canopy energy and water balance processes and the overhead multidimensional arrangement of forest canopy characteristics. Intercepted snow on the forest canopy drives sublimation in forested areas and like interception, sublimation is highly variable. Many studies have estimated sublimation from coniferous canopies to range from 25 to 50% of the total annual snowfall in cold and dry climates typical of the northern boreal forests (Essery and Pomeroy, 2001; Hedstrom and Pomeroy, 1998; Lundberg and Halldin, 2001). Interception in many cases represents water lost (due to sublimation) to not only local water balances, but to larger-scale water budgets. Within the Northern Hemisphere it is estimated that 20% of the seasonal snow cover is located within forested areas and can account for 17% of total terrestrial water storage during the winter season (Guntner et al., 2007; Rutter et al., 2009).

Due to the recognized importance of forest snow processes on the water budget, many snow models include a vegetative canopy representation. The Snow Model Inter-comparison Project (SnowMIP2) included 33 models with a canopy representation of varying degrees of complexity (Esssery, 2009; Rutter et al., 2009). All of these models, which have directly integrated a snow interception module, utilize either canopy closure (CC), leaf area index (LAI) or a composite of the two to describe the canopy structure. However, the interplay between canopy characteristics such as LAI and CC and snow interception also depends on where these characteristics are situated in relation to the greater surrounding forest architecture.

Canopy gaps have large impacts on the snow holding capacity in many forested areas. These areas can show divergent snow accumulation patterns as compared to the surrounding forest and can house maximum snow accumulation even as compared to neighboring open areas (Troendle and Meiman, 1986; Winkler et al., 2005). The interfaces between the open and forested areas also show the most heterogeneous snow accumulation and ablation patterns within a forested area and can house both the maxima and minima snow depths depending upon the position relative to the surrounding forest (Golding and Swanson, 1986; Veatch et al., 2009). In efforts to describe the relationship between openness and surrounding canopy, some practitioners categorize gaps for opening size as a function of the average surrounding tree size. In order to permit for more robust interception modeling at landscape scales, the greater canopy topography as well as the spatial heterogeneity of canopy structure needs to be accounted for within the models. Despite this, interception modules continue to use only point based predictors, most likely due to the intensive requisite time involved in collecting canopy metrics over large areas.

Standard overhead canopy structure methods for measurement are prohibitively labor intensive and normally require destructive sampling of the overstory. However, there are many indirect methods which include hemispherical photography, plant canopy analyzers (LAI-2000), or a spherical densitometer and each have particular strengths and weaknesses (Breda, 2003; Hyer and Goetz, 2004). Hemispherical photography (HP) is increasingly becoming a standard method for canopy

structure characterization. However, this technique can deliver a broad range of estimates dependent upon the initial camera and utilized program settings and allows for derivations of only point based CC, LAI and incoming shortwave radiation on the forest floor (Zhang, et al., 2005). HP image acquisition and processing, like the other field methods, is also very time consuming, thus limiting the utility of accurately describing these metrics for large areas.

Airborne laser scanning (ALS) data has been increasingly utilized to derive estimates of CC and LAI with good correlations and is becoming more readily available for large areas throughout the world (Asner et al. 2011; Fleck et al., 2012; Korhonen et al., 2014; Lovell et al., 2003; Moeser et al., 2014; Morsdorf et al., 2006; Morsdorf et al., 2004; Riaño et al., 2004; Solberg, 2010; Solberg et al., 2009). ALS can also derive large scale features such as canopy openings within forested areas and it is also possible to provide information on how these open areas are positioned relative to the surrounding forest.

Since ALS can quickly characterize surfaces over large scales, it can also be used for a variety of novel canopy metric estimates of potential value for forest snow modeling. As outlined above, such investigations represent a significant research gap with large potential improvements within forest hydrology, which have just begun to be investigated (Varhola et al., 2010a; Zhao et al., 2011). While the aim is to find metrics specifically related to snow interception, it is possible that there could be overlap from these findings into other disciplines such as forest ecology and biology, where such metrics have not yet been fully investigated.

This analysis was done in order to better answer the following questions: Should we be using LAI and CC as the primary canopy descriptors within forest snow models? Are there more robust canopy descriptors which could be utilized? This work has highlighted the utility behind the algorithm used for the calculation of new canopy metrics and tested their functionality. We created 57 canopy metrics from ALS data of potential value for snow modeling. The variables were meant to estimate size and relative location of gap openings around a point within a forested area, allowing for measures of the spatial arrangement of surrounding canopy elements. These new metrics were directly correlated snow

interception measured in the field (8488 manually measured snow interception points). The results were further compared to the correlation values between interception and the traditional parameters (CC, LAI), as well as incoming shortwave radiation estimates. The correspondence between all metrics was also analyzed in order to understand the potential cross correlation between each parameter.

3.2   Methods

3.2.1   Field areas
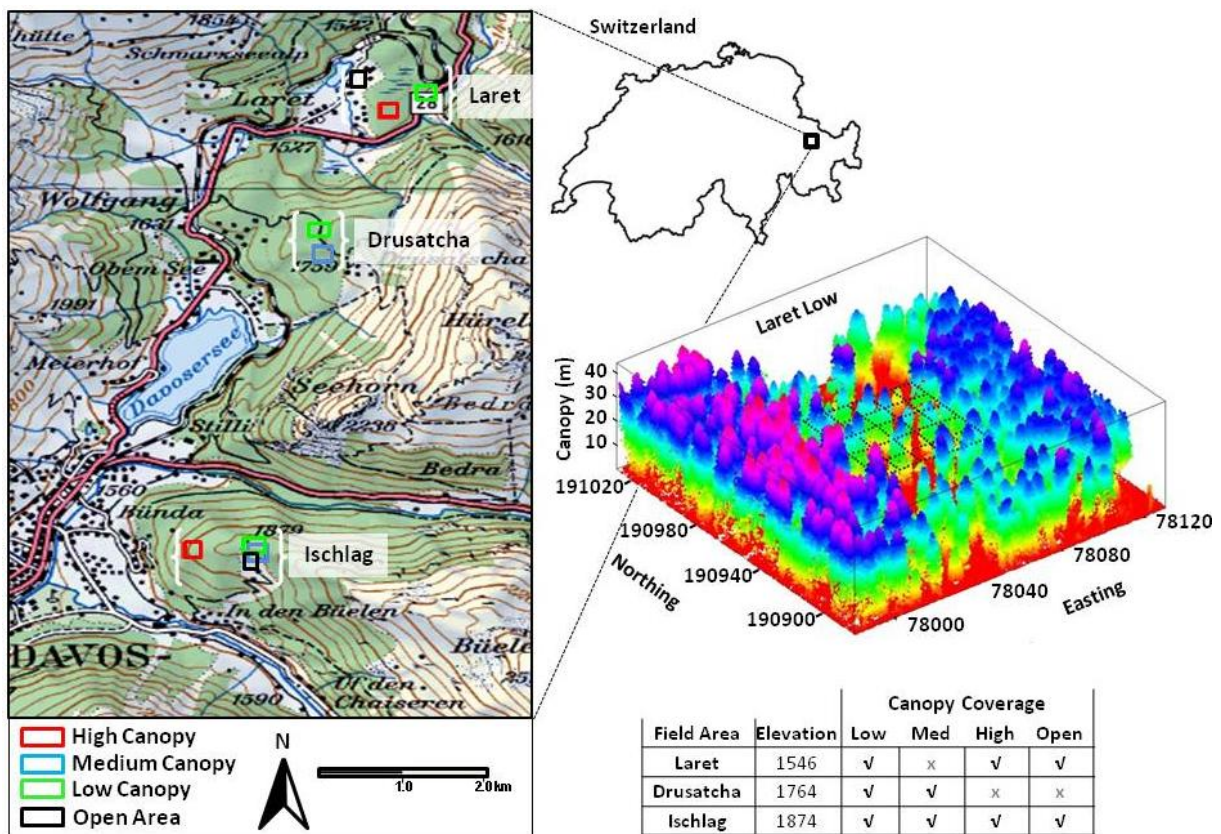
Figure 1. There were seven forested areas and two open field areas located in three elevation regimes around Davos in eastern Switzerland. Each field area was located in a unique gap fraction regime and maintained heterogeneous canopy characteristics. The box plot on the right is a representation of the ALS cloud data within the Laret low field area. The sampling grid with each point (276 points), represented as black dots along the internal grid, can be seen within the ALS cloud box plot. The other field areas have the same experimental setup and the generalized canopy coverages and elevations for these areas can be seen in the lower right table.

Seven forested field areas were equipped for a multiyear study in the region immediately surrounding Davos, Switzerland (Figure 1). The field areas were 50 m by 50 m, and were chosen due to the highly heterogeneous canopy coverages at the sub-plot scale along with larger scale canopy characteristics

such as open areas present within the 'medium' and 'low' sites (Figure 1). Forest stands were predominately Norwegian spruce and varied in height from new growth up to 45 m in height with the majority between 10 and 30 m. Within each field area were 276 pre-labeled and surveyed points with a maximum absolute positioning error of +/-50cm (derived from 36 control measurements within each field area) for a total of 1932 locations for repeated ground measurements. Each sampling grid was arranged in the same setup within all field areas (Figure 1). Two open field areas were further equipped as reference sites for direct comparison to the under canopy snow measurements (refer to Moeser et al., 2014 for a more detailed description).

3.2.2   Snow data collection

Snow depth data was collected after every snow storm event (defined here as a total open area snowfall amount of 15 cm or greater) in the winter 2012 and 2013 season (15 cm threshold dictated by the IMIS-SLF meteorological station from the Intercantonal measurement and information system). These depth measurements were collected at each forested point (1932 points) as well as at 100 open area control points (total of 69552 measurements). Snow interception however was measured after only 9 of these snowfall events (from a total of 27) due to the demanding pre-conditions necessary for such a campaign: (1) Forest canopy 100% snow free before a snow storm event, (2) A defined crust on the underlying snow, and (3) minimal wind redistribution during the storm period. When all of these pre-conditions were met, a differential snow depth was measured immediately after snowfall, i.e. the new snow accumulated on top of the overlying crust. From these pre-conditions, the measurements can be thought of as 1 - snow interception. After parsing all snow measurements and removing all data potentially conflicting with the pre-conditions there were 8488 remaining interception measurement points available for comparison. Despite the initial data parsing and the pre conditions, it is likely the data contains intra storm period unloading events when the maximum interception capacity above a measurement point is reached. Due to this, the interception measurements refer to effective interception (or cumulative storm interception). It is possible to attach an unloading estimate to these measurements from the work of Hedstrom and Pomeroy (1998), Pomeroy et al. (1998 a, b) as well as Storck et al. (2002). However, these unloading metrics involve just an initial multiplier (0.678 and 0.6

respectively) regardless of the time step or overlying canopy, creating no change in the correlation between the interception measurements and the proposed canopy metrics. Furthermore, the only other unloading algorithms of which the authors are aware use a temperature threshold of 0 at which point the difference between the snow storage capacity of the tree and the rain storage capacity of the tree is given as unloaded snow (Koivusala et al., 2002). Since the temperature values are well below freezing, this algorithm would not account for the snow unloaded during the storms (Table 1).

Table 1. Dates of snow sampling within the 2012/13 and 13/14 winter seasons. The snow depth measurements represent the total snow storm depth which fell in the Laret open field site. The swe and temperature, representing storm based values (swe – total storm swe, and temp - average storm temperature °C), are modeled for the Laret open field site. The wind speed is the average wind speed during each storm event at the Davos Stilli Meteorological station at 1560m situated just south of the lake seen (and labeled) in figure 1.

storm date	snow depth (cm)	swe (mm)	temp (°C)	wind speed (m/s)
13-Jan-2013	28.53	22.65	-3.9	0.27
22-Feb-2013	20.31	13.89	-12.1	0.55
6-Mar-2013	37.16	28.96	-4.2	0.56
20-Mar-2013	16.81	13.62	-3.5	0.19
27-Mar-2013	17.41	12.81	-5.7	0.58
15-Jan-2014	27.65	24.42	-2.4	1.71
28-Jan-2014	27.80	21.18	-4.7	0.26
17-Feb-2014	24.31	22.49	-1.9	1.38
24-Mar-2014	35.88	26.93	-5.1	2.33

All snow depth values were converted into snow water equivalent (SWE) from the US Army Corps of Engineers (1956) where snow density was related to the average storm temperature as follows:

$$\text{snow density} = 67.92 + 51.25\, e^{(T/2.59)} \qquad \text{eq. (1)}$$
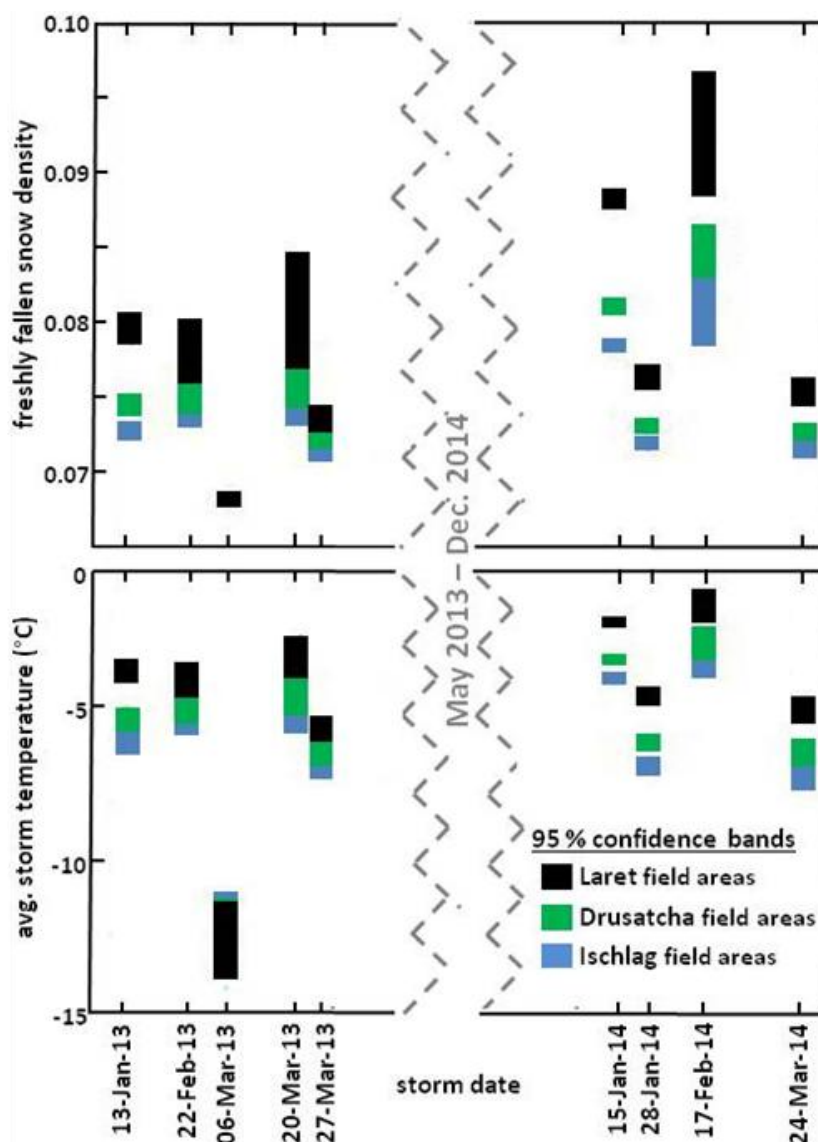
Figure 2. Four meteorological stations surrounding Davos were used to create a linear temperature model unique to each time step to estimate temperature at each field area. These temperatures were then used to estimate the density of the freshly fallen snow at each field area for each storm using the algorithm from the US Army Corps of Engineers (1956). The confidence intervals for the density model utilize the confidence bounds from the temperature models. Note that the confidence bands within the density graph are minimal at low temperatures due to the exponential nature of the density model showing that despite large spread in confidence for the temperature during storm 3, this uncertainly was not transferred to the density model.

where T is the average storm air temperature (°C). The air temperature at each site, for each storm event, was interpolated from individual linear models created for each storm event with an average correlation coefficient of 0.92 and root mean square error of 0.38 (Figure 2). Each temperature model utilized temperature data from 4 meteorological stations from the 'Intercantonal measurement and

information system' (IMIS) surrounding Davos, Switzerland at four unique elevation bands: 1560 m, 2140 m, 2290 m, 2540 m (IMIS – KLO, IMIS – SLF, IMIS – PAR, IMIS – WFJ).

Equation one was then used to attach fresh snow density values to all measured snow depth values at each storm to calculate SWE. Finally, the observed interception was derived from the difference between the freshly fallen SWE in the open and the freshly fallen SWE in the forest.

3.2.3   ALS Data

3.2.3.1   Technical details

ALS data acquisition was carried out from the 11th to the 15th of September 2010 using a Riegl LMS Q 560 sensor from a series of helicopter flyovers at a nominal flying altitude of 700 meters above the ground for a total area of ~90km^2. The wavelength emitted from the Riegl device was 1550 nm with pulse durations of 5 ns and up to 7 returns were detected per pulse using a maximum scan angle of ±15°. Morsdorf et al. (2008) performed an experiment over similar terrain within similar conditions where it was showed that small scan angles do not significantly alter the measurements of canopy gap fractions. The post processing of the full waveform data set yielded an average echo density of 36 pulses per m^2 of the flyover domain and 19 pulses per m^2 for the last returns (i.e. shot density) within the utilized domain area. The affiliated digital terrain model (DTM) or the underlying ground surface elevations were computed by using the classified ground returns at a 0.5 m horizontal resolution by Toposys using their in house processing software, TopPit (http://www.toposys.com/).

3.2.3.2   CC, LAI and radiation flux derivation

Canopy Closure, LAI (effective LAI) and incoming shortwave radiation was estimated from the ALS data by creation of synthetic hemispheric images at each ground point (1932 points) from conversion of the standard Cartesian X,Y,Z coordinate system to a polar system to mimic the angular viewpoint of a hemispherical photograph. These synthetic images were processed as if they were normal hemispherical photographs with 'Hemisfer', an image analysis software developed at the Swiss Federal Institute   for   Forest,   Snow   and   Landscape   Research   WSL (http://www.wsl.ch/dienstleistungen/produkte/software/hemisfer/, Thimonier et al., 2010). Despite the

limited scan angle of the flyover, these estimates showed high correlations ranging from R = 0.83 for LAI , R = 0.93 for CC (when compared to hemispherical photos) and R = 0.90 – 09.4 for incoming solar radiation (when compared to radiometer data) depending upon the site. Refer to Moeser et al. (2014) for a detailed method description.

3.2.3.3 Canopy metric definition

In addition to the standard metrics (CC, LAI), new canopy metrics were created at each ground point (1932 points). These metrics were generated from a vector searching algorithm designed to analyze ALS data for canopy characteristics which quantify the dimensions of a canopy gap at various directions as well as total gap size area. This section explains the basic functionality of the algorithm and gives general definitions of the new canopy metrics. Section 2.3.4 gives a detailed explanation of how the algorithm functioned.

The algorithm searched ALS data transformed into a 2 dimensional tree height model at specific user defined locations (i.e. the ground points). The data was scanned for presence of canopy elements in 192 unique directions (every 1.9 degrees) on the planar surface from vectors originating at a predefined point. Each of the 192 directional vectors, with the origin at the user defined location, traveled in unique and constant directions until a canopy element was hit (end point). Each vector was then attached the distance (in meters) between the user defined location and the closest canopy feature which was in the directional path of the vector (Figure 3). All end points from the 192 vectors were connected and a 2-dimensional poly-shape was created (Figure 4 part c). This was repeated for all user defined locations. This poly-shape (total gap area) represented the size of the gap surrounding the user defined point(s) in m^2, or in other words the total open area around a point. The mean length of each directional vector (mean distance to canopy) in m, the max length of each vector (max distance to canopy), and the minimum length of each vector around from the user defined point (min distance to canopy) were also calculated which gave generalized information about the fetch of a canopy gap from the location perspective at the point in question, as well as the point(s) location relative to the gap.

Vector pairs were used in further calculations and were defined as the coupling of two opposing vectors (92 vector pairs). For example, the vector traveling exactly west from a point would be paired with the vector traveling exactly east. The mean length of the vector pairs were calculated (mean gap diameter) in m, along with the maximum (maximum gap diameter) and minimum vector pair lengths (minimum gap diameter) in order to provide basic information about the shape of the gap around the point in question.

All of these metrics were additionally generated for unique directional sectors, where the vector searching sectors were limited to 180 and 90 degree windows. The 180 degree windows included analyses restricted to the cardinal directions, north, south, east and west. The 90 degree windows included all quarter quadrants as well as the cardinal directions: north, south, east, west, northeast, southeast, southwest, and northwest. Refer to table 2 for an overview of the calculated metrics. To use total gap area as an example; total gap area was calculated around the predefined points for the (1) entire domain (360 degrees), (2) to the north with a 180 degree search window, (3) to the east with a 180 degree search window, (4) to the south with a 180 degree search window, (5) to the west with a 180 degree search window, (6) to north with a 90 degree search window, (7) to the northeast with a 90 degree search window, (8) to the east with a 90 degree search window, (9) to the southeast with a 90 degree search window, (10) to the south with a 90 degree search window, (11) to the southwest with a 90 degree search window, (12) to the west with a 90 degree search window, and (13) to the northwest with a 90 degree

Table 2. Fifty-seven canopy metrics were created from the searching algorithm. Gap area and distance to canopy metrics were derived for the entire domain as well as for each directional sector from a 90 and 180 degree search window. The gap diameter metrics and canopy height proxies were generated only for the entire domain. Values within parentheses indicate number of times the descriptor was created.

| Canopy Descriptors	The full domain	180°sector (N,S, E, W)	90°sector (N,S, E,
total gap area (m²)	√	√ (4x)	√ (8x)
max gap diameter (m)	√	---	---
max distance to canopy (m)	√	√ (4x)	√ (8x)
min gap diameter (m)	√	---	---
min distance to canopy (m)	√	√ (4x)	√ (8x)
mean gap diameter (m)	√	---	---
mean distance to canopy (m)	√	√ (4x)	√ (8x)
max canopy height proxy (m)	√	---	---
mean canopy height proxy (m)	√	---	---

Figure 3. Schematic of the searching vectors (blue) movement within an empty domain. Vectors begin and finish due north and move in a clockwise rotation. Red lines represent the breaks between the directional sectors. The underlying gridded domain is seen in the background. The vectors reach the edge of the domain unless a canopy element (represented as a dark circle) is first reached.

search window. The directional windows were also used for the mean distance to canopy, maximum distance to canopy and minimum distance to canopy metrics. The vector pair metrics (mean gap diameter, maximum gap diameter and minimum gap diameter) were only generated for the entire domain (360 degree window).

Finally, in addition to the directional searches, a secondary static domain with a 10m radius around each point was then used to estimate general tree height proxies around the predefined points. A maximum canopy height value (max canopy height proxy) was calculated for each data trap as well as an average of all values within each data trap (mean canopy height proxy) from the tree height module. Table 2 outlines all calculated metrics.

3.2.3.4   Searching algorithm construction

The directional search for canopy elements surrounding a given center location utilized the general procedure outlined in the previous section. Specifically, an initial height threshold (hth), a starting bounding box where the vectors travel through despite potential presence of canopy elements, and a basic smoothing function were integrated into the algorithm to cope with unwanted scatter due to ungrouped understory canopy returns (Figure 4).

When a height threshold is set, the algorithm ignores all canopy elements which have heights less than the pre-established value. The height threshold was set at 1.25 meters in order to mimic settings that were also used for the derivation of the ALS based CC, LAI and incoming solar radiation (Moeser et al.,2014). Therefore the 192 vectors around the predefined point(s) only stop when a canopy element greater than the hth (1.25 m) within the direction path is reached.
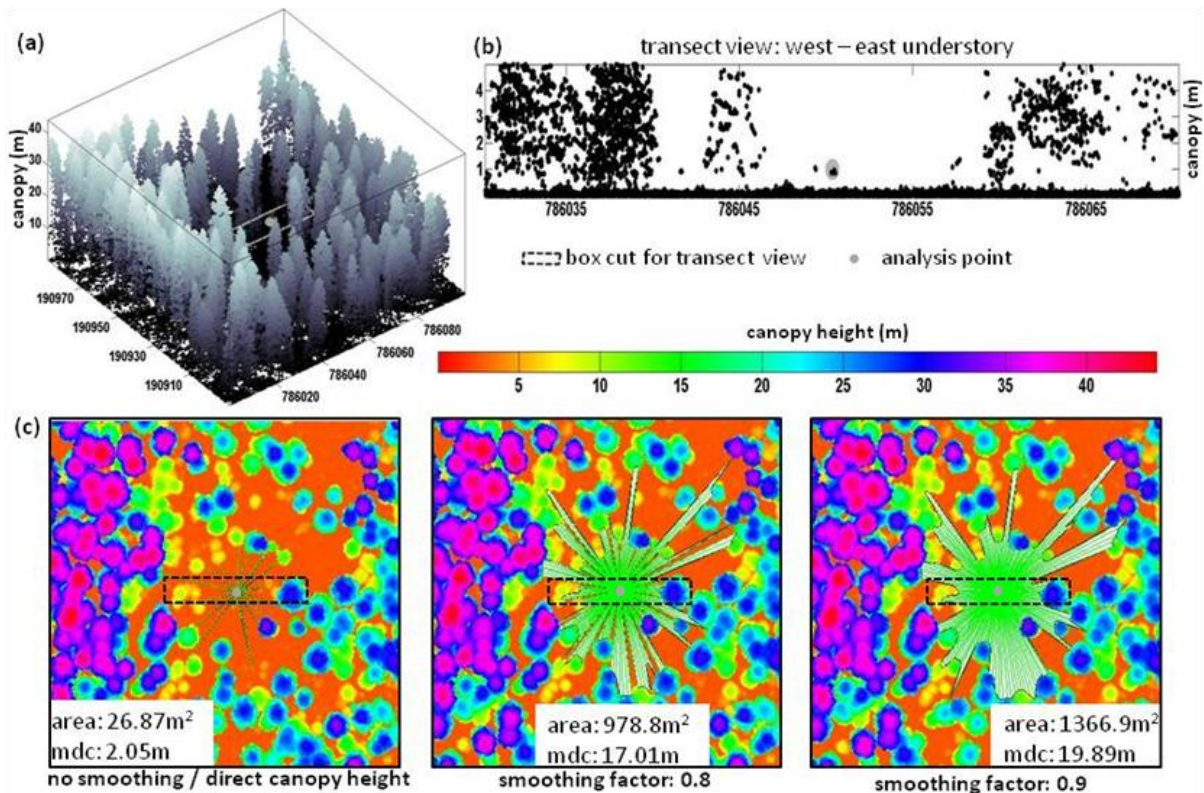
Figure 4. (a) LiDAR point cloud data around measurement point 'C1' within the 'Laret low' field area. (b) Shows the understory of LiDAR returns (zoom in of canopy returns less than 5 m which were located within the box cut domain seen within each subsequent tile) with the analysis point at the established hth of 1.25 m. Please note lack of structure seen within the understory as compared to the overstory in part a. (c) 2-d viewpoints of the same data from part a. These tile show the polygon's created in green from 3 different smoothing scenarios. The estimated gap area (area) and mean dist to canopy (mdc) can be seen within the insets of each. Column three of (c) shows the best fit smoothing factor of 0.9. The black box within each plan view shows the exact dimensions of the transect view in part b. All utilize a starting box of 0.75 m and a height threshold of 1.25 m.

The smoothing function was introduced in order to reduce the amount of noise effects of the ALS returns within the understory. Refer to figure 4 for a transect view of the understory surrounding a point. The smoothing function was implemented by creating a 0.25 x 0.25m raster of the ALS data cloud where the average return value (transformed to canopy heights) was then assigned to each grid cell. This grid was then binarized based on the hth: When the gridded canopy returns were ≥ hth (1.25m), the grid cell value was assigned 1 and when the return was < hth (1.25m), the grid cell value was assigned 0. A moving 3x3 neighborhood cell mean filter was applied over the domain (200m * 200m domain around each analysis point) where each element i, situated in the middle of the neighborhood, was assigned the mean of the neighborhood.

The smoothing function was further parameterized by a smoothing factor which represented a percentage of canopy / percentage of total. The smoothing factor acted as secondary threshold within the smoothed raster and values above this threshold value were considered canopy and values below are passed through by the search vectors. This value was optimized to a value of 0.9 (the vector was stopped at a grid cell when at least 90 percent of the surrounding grid cells had canopy elements over the hth.) based on a visual comparison with the ALS data cloud (Figure 4c). From the use of this smoothing factor with the smoothed raster, the vectors were able to bypass ungrouped understory canopy returns, which allowed for the vectors to travel past canopy returns which fell over the hth (1.25m) but demonstrated a low surrounding density (Figure 4b).

Finally, since the smoothing function was based on a gridded approach, an initial starting bounding box was integrated. For example, if the neighboring pixel to the north of the starting point was classified as canopy, then entire 45 degree viewshed to the north would have also been classified as canopy, since all vectors traveling between the northwest and northeast directions would hit this grid cell. Due to this, an initial starting distance of 0.75m was allocated to the searching vectors, which reduced the significance of canopy hits close to the starting point affecting the neighboring classifications.

3.2.3.5   Searching algorithm transferability

Since the vector searching algorithm works on ALS data converted to a raster, high point cloud density data is not necessarily needed to provide accurate metric derivation. This process has been fully automated and initial settings including the height threshold, the grid size of the raster (raster of ALS data cloud), smoothing factor and initial starting bounding box as well as the predefined location list (where the process was to be performed) were programmed as user defined presets. This flexibility allows for the use of this algorithm within other data sets regardless of the initial data resolution.

3.2.4   Data analysis

In accordance with the snow measurement assumptions (Section 2.2), snow interception (in mm SWE) can then be thought of as: SWE in the open (P_{open}) – SWE in the forest (SWE_{forest}). In order to normalize the data over each storm event, the ratio of SWE_{forest} / P_{open} was used as a direct comparison

to the metrics from the ALS data. This included all metrics seen within table 2 as well as the LAI, CC, and incoming solar radiation generated from synthetic ALS images (Section 2.3.2). All metrics were individually correlated to the interception data at each storm event and subsequently averaged.

All forest metrics were then inter-compared using correspondence analysis (CA) in order to analyze cross-correlation between the metrics. CA is a non-parametric principle component method for analyzing correspondence or independence among variables. The significance of each association was based upon the chi-squared distance between each data point and the expected value, where the expected value was equal to the value that has the highest probability of occurring within the dataset (Car, 2002). Eigenvectors (factors) associated with the Eigen decomposition of the matrix of the chi-square values from the data set were plotted on independent axes, along with the Eigen values for each sample which allowed for a visual assessment of independence or cross correlation. Each factor axes were also assigned a significance value (percent of inertia) which represented an estimate of the amount of variability captured within the dataset from the factor. Independence was then analyzed by the plotted variable separation distance, with greater significance given to the separation on the axes with a higher factor value (Greenacre and Blasius, 1994; Lorenzo-Seva et al., 2009; Van de Velden and Kiers, 2003; Van de Velden and Kiers, 2005).

K means clustering was then used in order to automatically choose groups of variables which have similar CA plotting characteristics by maximizing the inter cluster distance and minimizing the intra cluster distances (Seber, 2004; Späth, 1985). Independence within CA is normally qualitatively analyzed from a visual analysis of variable separation. However, this unique method pairing (CA and K means clustering) allowed for an automated and unbiased approach. The analysis was performed iteratively from a random centroid selection of each potential cluster (cluster groups set to 4). The factor values from the CA were also integrated into the K means clustering routine, where the partitioning of the intra and inter clustering distances were further based on the factor value (refer to axis values in figure 5). Each factor value was given a normalized percent weight based on the additive of each plotted dimension factor value (3 dimensions). These weights were then applied to the coordinates of

the input data. This allowed the k means clustering routine to favor relationships based upon the amount of variance captured within each dimension (percent of inertia).

3.3   Results and Discussion

Table 3 gives an overview of correlations of canopy metrics to interception ratio. All gap diameter metrics retained almost exact correlations as the distance to canopy metrics. Due to this, the gap diameter metrics have been removed from table 3. This highlights the near identical predictive ability of these two metrics and shows that mean gap diameter represents, regardless of the quadrant, almost equivalent gap opening characteristics as mean distance to canopy. Furthermore, All maximum and minimum estimates (max/min distance to canopy, max/min gap diameter for the entire domain as well as sectors) demonstrated significantly lower correlations to the interception rate as compared to mean (mean distance to canopy, mean gap diameter) or total gap area estimates. Therefore all metrics quantifying maximum or minimum length regardless of the quadrant have also been removed from table 3. This implies that even if there are large fetches within a specific direction where there is no canopy, the influence to snow interception is minimal. The descriptors which integrate all directions within a sector are better apt at interception estimation than canopy metrics which hold true only for specific directions. However, estimations of such metrics (max/min distance to canopy, max/min gap diameter) could prove important for other factors within the energy balance valuable for forest snow modeling that are not analyzed in this study such as radiation transfer.

The highest correlated metric was mean distance to canopy and maintained this ranking (average R = 0.78, standard deviation = 0.09) within each precipitation event (correlation range = 0.58 - 0.89). Canopy closure had a slightly reduced average correlation (-6%) at 0.72 and demonstrated a slightly higher standard deviation with a correlation range between 0.43 and 0.87. LAI showed significantly lower correlations than the higher correlated metrics, with an average R of 0.57, standard deviation of 0.16 and a correlation range between 0.21 and 0.77. The best correlated area metric was total gap area which shared an equivalent average correlation with canopy closure at 0.72 and a slightly reduced standard deviation of 0.11 (correlation range = 0.50 – 0.86). These results imply that metrics which

evaluate the overall position of a point in space (mean distance to canopy), as well as metrics which calculate larger scale features (total gap area), are equally important for interception estimation as the canopy parameters which evaluate just overlying canopy density above a point. An overview of the metric statistics can be seen in table 3.

The correspondence and k means analysis shown in figure 5 utilized a compilation of all storm events. However, similar results were also observed when the analysis was run on individual storm events. The smallest cluster (n=3) retained canopy closure, leaf area index and tree height proxies. The tight clustering of these parameters demonstrated a significant amount of cross-correlation (dependence) between these metrics and implied that regardless of the metric, they represented identical parts of the total interception variation. The strongest (highest correlation to interception) member of this grouping was tied at mean tree height and canopy closure with the lowest correlated end member being leaf area index. This implied that not only may LAI not be the best predictor for interception, but regardless of which of these metrics are used, identical parts of the total interception variation are represented.

 The second smallest cluster (n=10) integrated all total gap area metrics (total gap area, gap area to the north 180°, gap area to the northeast 90°, etc) except those to a southerly direction, with the strongest member being total gap area. This demonstrates the potential utility of a canopy metric which represents a larger scale feature such as canopy and forest openings.

The next grouping (n= 15) incorporated all distance to the south estimates (mean distance to canopy - south 180°, mean distance to canopy - southeast 90°, etc), area to the south estimates (mean gap area - south 180°, mean gap area - southeast 90°, etc), and all incoming solar radiation estimates which incorporated the direct component (direct incoming solar radiation- DIR_IR and average daily potential incoming solar radiation – PISR). The strongest member was average daily potential incoming solar radiation (PISR). This doesn't necessary imply that solar radiation is an important factor within interception modeling, this does however highlight the interplay between canopy openness and solar radiation, and shows that perhaps area measurements to the south could be used as a solar radiation proxy when no direct estimates are available for snow melt studies.

The largest grouping (n=45) incorporated all distance estimates (mean distance to canopy, mean distance to canopy - north 180°, mean distance to canopy - northeast 90°, etc.) except those with a southern aspect as well as all diffuse incoming radiation estimates (DIF_IR). The strongest end member in this grouping, mean distance to canopy also had the highest overall correlations of all analyzed metrics and maintained low variance for all storm events. These correspondence results in tandem with the correlation analysis highlight that metrics which analyze the overall position of a point within a gap relative to the canopy, are equally, if not more important for interception modeling, than just a canopy coverage assessment.

Table 3. Overview of correlations of canopy metrics to interception ratio, where the mean represents correlations averaged over each storm event and stdev represents the standard deviation of the correlations. All values under each header are organized from high to low correlation. No maximum or minimum distance to canopy estimations are shown due to significantly lower correlations as compared to the mean distance estimates. Gap area diameter estimates were also removed due to near identical correlations shared with mean distance to canopy estimations. 'DIF_IR' represents the diffuse under canopy component of the estimated incoming solar radiation, 'DIR_IR' represents the direct under canopy component of the estimated incoming solar radiation and 'PISR' represents the potential incoming solar radiation or a composite of the direct and indirect component. While canopy closure maintains significant correlations please note the low LAI value of 0.57 (range 0.21 – 0.77) which demonstrated a 21% reduction as compared to the best correlated factor, mean distance to canopy (R: 0.78). **represents variables created using synthetic images.

| Correlations to SWE interception at 9 storm events					
Searching Function - distance			**Searching Function - area**		
	mean	**stdev**		**mean**	**stdev**
mean dist. to canopy	0.78	0.09	total gap area	0.72	0.11
mean dist. to canopy - north 180°	0.74	0.10	total gap area - east 180°	0.67	0.11
mean dist. to canopy - east 180°	0.74	0.09	total gap area - north 180°	0.64	0.11
mean dist. to canopy - south	0.70	0.09	total gap area - south 180°	0.64	0.10
mean dist. to canopy - east 90°	0.70	0.09	total gap area - east 90°	0.60	0.10
mean dist. to canopy - NE. 90°	0.69	0.09	total gap area - NE. 90°	0.59	0.09
mean dist. to canopy - west 180°	0.68	0.09	total gap area - west 180°	0.57	0.09
mean dist. to canopy - north 90°	0.67	0.10	total gap area -SE. 90°	0.55	0.10
mean dist. to canopy - SE. 90°	0.64	0.09	total gap area - south 90°	0.52	0.09
mean dist. to canopy - NW. 90°	0.62	0.10	total gap area - north 90°	0.50	0.10
mean dist. to canopy - south 90°	0.62	0.08	total gap area - SW. 90°	0.50	0.08
mean dist. to canopy - west 90°	0.61	0.08	total gap area -NW. 90°	0.49	0.11
mean dist. to canopy - SW. 90°	0.60	0.07	total gap area - west 90°	0.48	0.08
solar radiation			**standard metrics**		
mean daily DIF_IR**	0.74	0.12	mean canopy height	0.72	0.08
mean daily PISR**	0.67	0.14	canopy closure**	0.72	0.13
meandaily DIR_IR**	0.54	0.15	LAI**	0.57	0.16
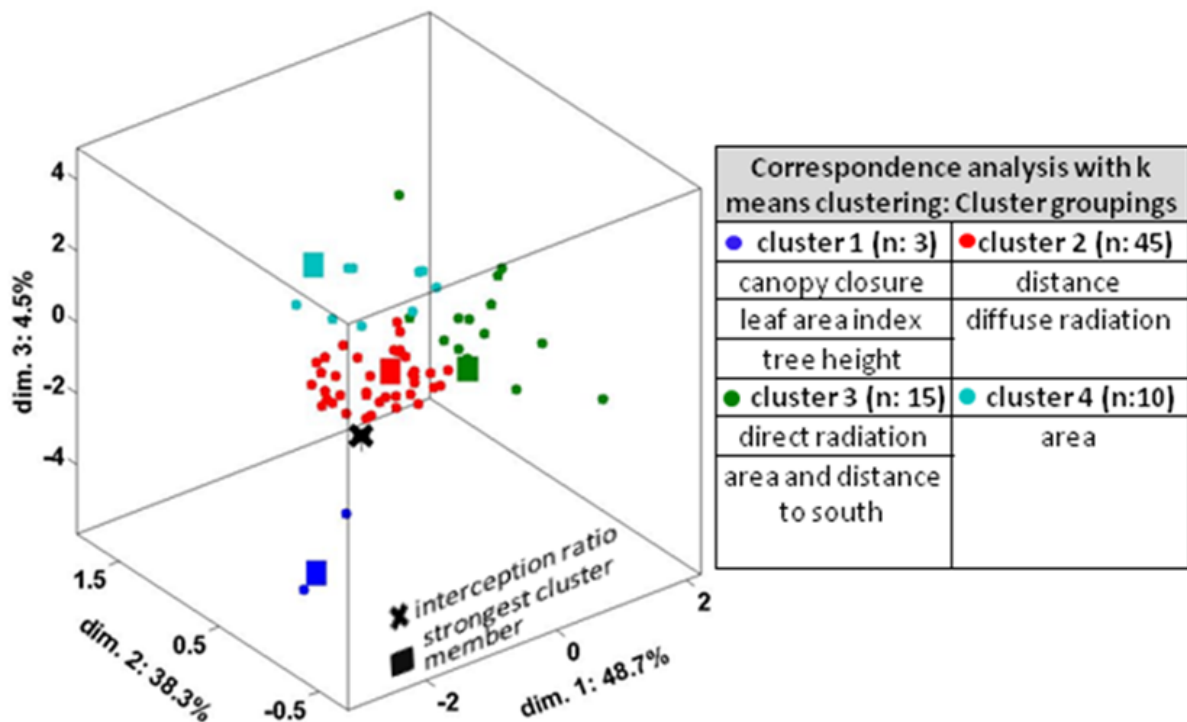
Figure 5. Correspondence analysis with integrated k means clustering of metrics for 4 groupings. Each grouping is represented by a color, and within each grouping a box shows the location of highest correlated metric within the grouping. The cross represents the location of the independent element, snow interception ratio. The traditional canopy descriptors, CC and LAI and the mean tree height proxy were plotted in the same grouping, showing a high degree of cross correlation between these descriptors. The second largest grouping in light blue integrated only estimates of area. The third cluster included direct radiation estimates as well as area and distance estimates to the south. The largest cluster (red) integrated all remaining distance estimators and included the highest correlated factor of the series, mean distance to canopy.

Finally, the metric correspondence analysis demonstrated that no increased predictive power is available within this dataset if LAI and CC are used simultaneously for snow interception estimates. It further highlighted the weak direct correlation between LAI and snow interception ratio. Several of the variables created from the searching algorithm demonstrated significantly higher correlations than LAI and showed distinct separation from the traditional metrics grouping (cluster 1). This implied that not only could a variable such as a mean distance to canopy accurately be used as an independent variable to model interception ratio but also that a composite of these variables could create a more robust model than the standard pairing of LAI and canopy closure. Current interception models, either stand alone, or subsequently integrated into snow melt models use this standard metric pairing. Therefore, it seems likely that one or more of the new metrics could be integrated into the interception

model distributions for a more accurate representation of the overall water balance within forested areas.

3.4   Conclusion

ALS has the potential to supplement not just interception modeling techniques but also forest snow modeling in general. Within the field areas surrounding Davos, Switzerland, the availability of ALS data has allowed for the creation of novel canopy metrics without the prohibitive time necessary to manually measure thousands of points to describe the canopy over large areas. The vector searching algorithm is fully automated and could characterize thousands of locations within the field areas (section 2.1) in a period of minutes. This, in conjunction with an extensive database of manually measured snow interception over heterogeneous terrain (~8,500 manual measurement points) allowed us to create and test the capabilities of new input metrics in relation to parameters historically used for forest snow modeling (CC , LAI).LAI demonstrated low correlations when directly compared to snow interception ratio and further showed a large cross-correlation with canopy closure. Mean distance to canopy had the highest correlation over all storm events to the interception ratio. But in contrast to LAI, this variable did not show any cross correlation with canopy closure (CC). Likewise, total gap area, an indirect measurement of apparent gap fraction also showed a high correlation to interception ratio without demonstrating a significant cross-correlation to CC or to mean distance to canopy.

These findings suggest that modeling forest snow processes with both CC and LAI may not be the best option due to both, the low correlation of LAI as well as high cross-correlation between these variables. However, the pairing of mean distance to canopy and/or total gap area with canopy closure could give more robust estimations of snow interception within heterogeneous terrain. Together, these variables have the ability to quantify not just canopy density but canopy metrics relative to larger scale canopy structural features such as canopy openings.

In order to permit for more robust modeling at scales greater than the point scale, the greater canopy topography needs to be accounted for. The inclusion of metrics which describe point based canopy topography (canopy closure) with those which give information regarding where these metrics reside in

relation to the larger encompassing features such as total gap area or mean distance to canopy could allow for better upscaling of snow forest models to the landscape scale.

All programming was performed using Matlab. All scripts related to this algorithm are freely available upon request.

Acknowledgements

Improved snow interception modeling using canopy parameters derived from airborne LIDAR data

D. Moeser[1,2], M. Stähli[3], T. Jonas[1]

[1]WSL Institute for Snow and Avalanche Research SLF, Davos Dorf, Switzerland
David Moeser: moeser@slf.ch   Tobias Jonas: jonas@slf.ch

[2] Forest Ecology, Institute of Terrestrial Ecosystems, Department of Environmental Sciences, Swiss Federal Institute of Technology ETH, Universitätstrasse. 16, CH-8092 Zurich, Switzerland

[3]Swiss Federal Institute for Forest, Snow and Landscape Research WSL, Birmensdorf, Switzerland
M. Stähli: manfred.staehli@wsl.ch

Abstract

Forest snow interception can account for large snow storage differences between open and forested areas. The effect of interception can also lead to significant variations in sublimation, with estimates varying from 5 to 60% of total snowfall. Most current interception models utilize canopy closure and LAI to partition interception from snowfall and calculate interception efficiency as an exponential decrease of interception efficiency with increasing precipitation. However, as demonstrated, these models can show specific deficiencies within heterogeneous canopy. Seven field areas were equipped with 1932 surveyed points within various canopy density regimes in three elevation bands surrounding Davos, Switzerland. Snow interception measurements were taken from 2012 to 2014 (~9,000 samples) and compared with measurements at two open sites. The measured data indicated the presence of snow bridging from a demonstrated increase in interception efficiency as precipitation increased until a maximum was reached. As precipitation increased beyond this maximum, the data then exhibited a

decrease in interception efficiency. Standard and novel canopy parameters were developed using aerial LiDAR data. These included estimates of LAI, canopy closure, distance to canopy, gap fraction and various tree size parameters. These canopy metrics and the underlying efficiency distribution were then integrated to formulate a conceptual model based upon the snow interception measurements. This model gave a ~27% increase in the R2(from 0.39 to 0.66) and a ~40% reduction in RMSE (from 5.19 to 3.39) for both calibration and validation data sets when compared to previous models at the point scale. When upscaled to larger grid sizes, the model demonstrated further increases in performance.

4.1 Introduction

The hydrology of cold forested regions is dominated by snow forest processes and plays a significant role within the global water budget. Snowmelt dominated watersheds which contain forests yield approximately 60% of the global freshwater runoff [Chang, 2003]. Within the Northern hemisphere it is estimated that 20% of the seasonal snow cover is located within forested areas and can account for 17% of total terrestrial water storage during the winter season [Guntner et al., 2007; Rutter et al., 2009].

In the Northern boreal forests, these processes are especially pronounced, with many internal forest snow mechanisms showing not just regional or local dependencies but demonstrating heterogeneity at extremely fine scales. Specifically, the surrounding forest structure can both augment and attenuate the physical forcing processes affiliated with snow accumulation and ablation. A prime example, intercepted snow from the forest canopy, ranges from 0 to just over 60% of total annual snowfall [Montesi et al., 2003; Storck et al., 2002]. Intercepted snow in most cases represents water lost, since this is the primary driver of sublimated snow in forested areas. Sublimation, like interception also demonstrates a significant range in values, and many studies have estimated sublimation to range up to 50% of the total annual snowfall [Essery and Pomeroy, 2001; Hedstrom and Pomeroy, 1998; Lundberg and Halldin, 2001]. This large range of interception when paired with similarly large sublimation estimates makes interception the single most dominate physical process to drive snow cover heterogeneity in forest regions.

Snow interception has been studied for over 100 years, with the initial studies from Carpenter [1901] and Church [1912] which qualitatively describe forest snow interception. To date, three papers known to the authors have attempted to synthesize the results of these studies and highlight the contrasting methods utilized to measure and represent interception processes [Bunnel et al., 1985; Lundberg and Halldin, 2001; Varhola et al., 2010b]. If anything, these results serve to highlight the complexity of the phenomenon and emphasize that despite the large volumes of prior work; still more is needed to create an interception model valid over various conditions at various scales.

Many papers have highlighted the importance of snow bridging, branch bending and snow bouncing on the maximum snow load and interception efficiency (interception / total precipitation) or the fraction of SWE which is intercepted in the canopy. Tennyson [1974] and Bründl [1999] visually captured these processes using time lapse photography/video and showed an initial increase in snow interception efficiency on both Ponderosa pine and Norwegian spruce. The adhesion and cohesion processes leading towards snow bridging (potential surface area increase as well as potential broadening of the stress bulb) and the subsequent (initial) interception efficiency increase has been described qualitatively by Bunnel et al [1985] and Miller [1964]. The first attempts to quantify these relationships were seen in the works of Satterlund and Haupt [1967] who developed a model in a Douglas fir and white pine forest which represented the underlying interception efficiency distribution as the growth phase of a sigmoidal curve. This work was furthered by Schmidt and Gluns [1991] who found a similar sigmoidal distribution in interception and efficiency in the branches of Engelmann spruce, subalpine fir, lodgepole pine and artificial branches. However the magnitude of the interception (and efficiency) was higher with the artificial branches implying interception depends on the bending potential of the branch or more specifically initial branch stiffness and the initial branch angle.

The model from Hedstrom and Pomeroy [1998] was one of the first to directly include canopy parameterizations (LAI and canopy closure (CC)). The model, based on their initial assumptions that interception efficiency (1) decreases with canopy snow load and (2) increases with canopy density,

used an exponential decay model as the underlying efficiency distribution which contrasted to the majority of the prior findings.

Due to the inherent difficulties in direct interception measurements, a variety of inventive methods have been implemented in the past works. However, the standard direct method is destructive and necessitates the cutting of a tree which is then attached to a scale [Hedstrom and Pomeroy, 1998; Nakai et al., 1994; Nakai, 1999; Pomeroy, 1998; Satterlund and Haupt, 1967; Schmidt and Gluns, 1991; Storck et al., 2002; Suzuki and Nakai, 2008]. Optical methods have also been employed, which relate the visually intercepted snow load from time lapse photography to field measurements [Brundl et al., 1999; Kobayashi, 1987; Nakai, 1999; Tennyson et al., 1974]. Gamma Ray attenuation has also been used to directly measure the snow water equivalence on branches [Calder 1991]. Due to the heavy material reliance of these direct methods, no data over larger scales has been collected. Of the above examples which also presented direct model equations for interception, the largest data set was collected by Schmidt et al [1991] for a total of 175 branch samples (30 – 36 cm in length) over two seasons. Satterlaund et al [1967] used 4 tree saplings (3.7-4.2 meters) for a 1 season study and Hedstrom and Pomeroy [1998] used 4 jack pine trees (7 -15 meters in height and 38 – 90 kg in weight) over 4 seasons and one black spruce tree (12 meters in height and 22 kg in weight) over one season.

Like interception measurements, direct methods for measurement of canopy structure are also labor intensive and normally require destructive sampling of the overhead canopy. However, there are many indirect methods including hemispherical photography, plant canopy analyzers (LAI-2000), and spherical densitometers and each have particular strengths and weaknesses depending on the specific structure element estimated [Breda, 2003; Hyer and Goetz, 2004]. Airborne laser scanning (ALS) data is increasingly utilized to accurately estimate CC and LAI and is readily available for large areas throughout the world [Lovell et al., 2003; Moeser et al., 2014; Morsdorf et al., 2006; Morsdorf et al., 2004; Riaño et al., 2004; Solberg, 2010; Solberg et al., 2009]. ALS can also derive large scale features such as canopy openings within forested areas and it is also possible to provide information on how these open areas are positioned relative to the surrounding forest. Since ALS can quickly characterize

surfaces over large scales, it can also be used for a variety of novel canopy parameter estimates potentially valuable for forest snow modeling. Investigations of large scale canopy features represent a significant research gap with large potential improvements in a variety of research fields which has just begun to be investigated [Moeser et al., 2015; Varhola et al., 2010a; Zhao et al., 2011].

The Snow Model Inter-comparison Project (SnowMIP2) recognized 33 snow melt models which have directly integrated a snow interception module of varying degrees of complexity [Esssery, 2009; Rutter et al., 2009]. All of these models, utilize either canopy closure (CC), leaf area index (LAI) or a composite of the two in order to describe the canopy structure, with the majority directly utilizing the proposed algorithm by Hedstrom and Pomeroy [1998]. However, the interplay between generalized canopy characteristics such as LAI and CC and snow interception also depends on where these characteristics are situated in relation to surrounding forest architecture. As an example, field areas which have differing large scale canopy structures such as forest gaps around a point can still have the same LAI or CC estimate.

Canopy gaps have large impacts on the snow holding capacity in many forested areas. These areas can show divergent snow accumulation patterns as compared to the surrounding forest and may have snow accumulation that exceeds nearby open, non-forested areas [Troendle and Meiman, 1986; Winkler et al., 2005]. The interface between the open and forested areas also show the most heterogeneous snow accumulation and ablation patterns within a forested area and can house both the maxima and minima depending upon the position relative to the surrounding forest [Golding and Swanson, 1986; Veatch et al., 2009]. In efforts to describe the relationship between openness and surrounding canopy, some practitioners categorize gaps for opening size as a function of the average surrounding tree size.

In order to permit for more robust interception modeling at landscape scales the greater canopy topography as well as the spatial heterogeneity of canopy structure needs to be accounted for within models. Despite this, interception modules continue to use only point based predictors, most likely due to the intensive requisite time involved in collecting canopy parameters over large areas. The inclusion

of parameters which describe point based canopy topography (canopy closure) with those which give information regarding where these parameters reside in relation to larger encompassing features such as the distribution of gaps around a point (e.g. total open area around a point), could allow for better upscaling of snow forest models to the landscape scale [Moeser et al., 2015]. ALS (when compared to manual collection methods) has the ability to provide such parameters over large scales, in a time and cost effective manner.

In order to develop a model that includes the greater canopy structure and allow for greater transferability of results, interception measurements are also needed over a large distribution of heterogeneous canopy architectures. With some assumptions, storm interception can be indirectly measured by comparing the ratio of newly fallen snow in the open to the amount newly fallen snow under the canopy. Typically this is done by measuring the new snow accumulation on top of preplaced boards [Kobayashi, 1987; Lundberg et al., 1998; Pfister and Schneebeli, 1999].

This research has utilized a novel indirect snow interception measurement method at thousands of surveyed measurements points (1932) within various canopy density and openness regimes over a series of interception events for a total of 9000 manually measured snow interception points (A) (cf. 4 – 175 samples from past studies). These interception estimates were then paired with novel canopy parameterizations from ALS data (B) in order to create a new interception model. This model integrated prior interception efficiency distribution research performed from branch, sapling and tree studies and scaled these to be effectively used over forest landscape scales from the integration of novel canopy parameters from ALS data.

This is the first study to utilize such a large database of interception measurements (A) as well as use novel canopy parameters which integrate larger scale canopy structure (B) for an interception model. We have highlighted the (1) basic process flow of this pairing and (2) demonstrated the utility by a comparison to the most used snow interception model to date [Hedstrom and Pomeroy, 1998] under a broad range of canopy conditions and scales.

Furthermore, the Hedstrom and Pomeroy model, of which we compared our model skill, was created in a cold boreal climate but is often utilized in a variety of different meteorological environments. This should emphasize the need for not just a model integrating larger scale canopy structure, but one better suited for temperate snow environments.

4.2   Methods
4.2.1   Field areas

Seven 50m by 50m forested field areas have been equipped for study in three unique elevation bands. They were set up in the fall of 2012 and are part of a long term forest snow hydrology study area operated by the WSL Institute for Snow and Avalanche Research (SLF). The field areas were characterized by highly heterogeneous canopy characteristics at the sub-plot scale along with the presence of larger scale canopy attributes such as canopy gaps. The field areas were further chosen to have low to no surface slopes and minimal surrounding terrain shading influences. The canopy was comprised of predominately Norwegian spruce with heights varying from seedling to a maximum of 45 meters, with the majority between 10 and 30 m. Each field area contained 276 surveyed points for a total of 1932 locations utilizable for ground measurements and canopy characterizations. The field areas consisted of 36 permanent poles drilled in to ground positions measured with a distometer with exactly 10 meter horizontal ((± 1cm) spacing from each other creating a 50m x 50 m grid. A fixed line was attached to all poles and 2 meter intervals were manually measured and marked between each. A differential GPS was used (± 20cm) at each of the poles to convert the projected coordinate system to a global one. The global coordinates were then distributed to all internal marked points for a final maximum rectification error of ± 50cm for each of the 1932 points. Two open field sites with 50 measurements points each (± 20cm) were also equipped as reference sites for direct comparison to the under canopy snow measurements. See figure one.
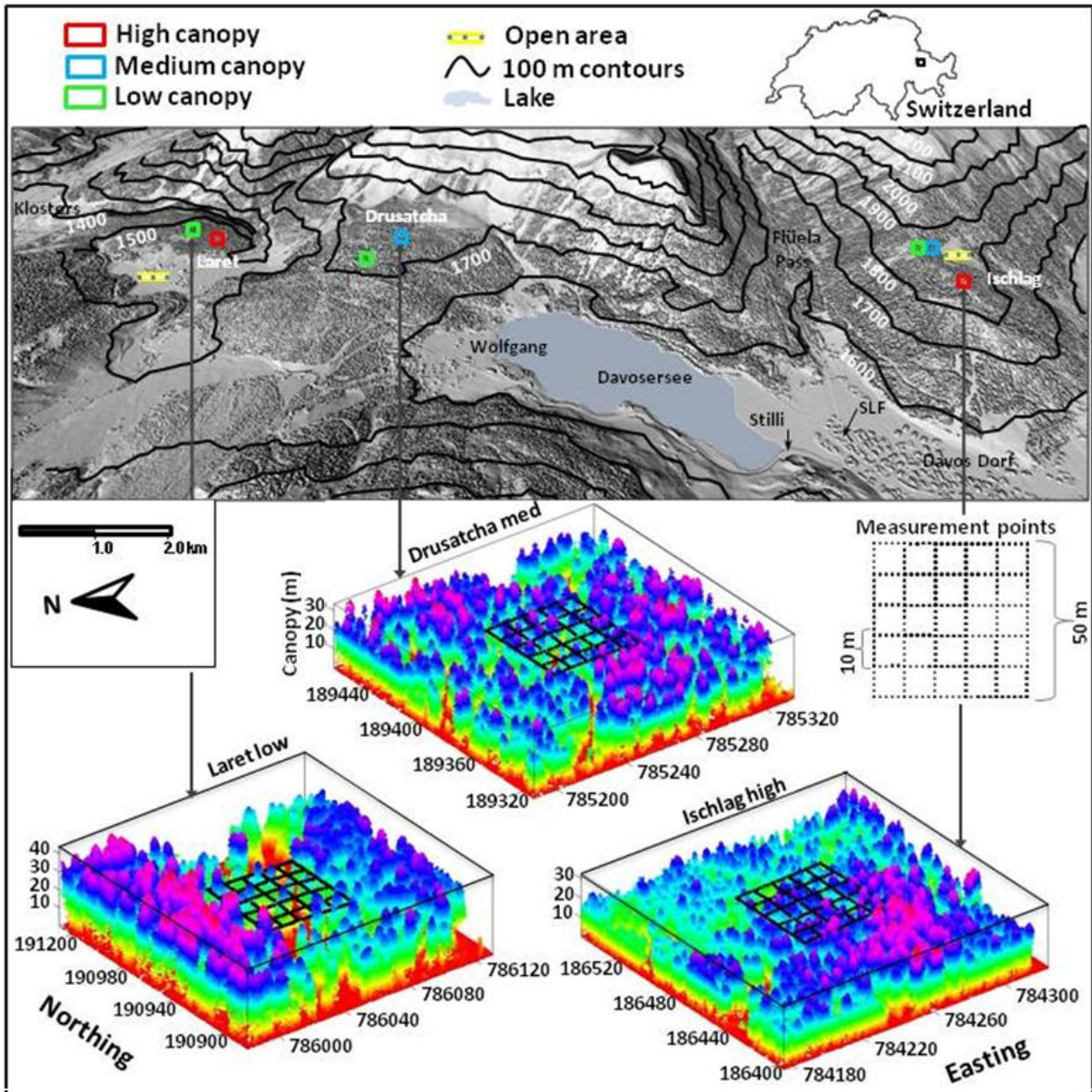
Figure 1. There were seven forested areas and two open field areas located in three elevation regimes around Davos in eastern Switzerland. Each field area was located in a unique gap fraction regime and maintained heterogeneous canopy characteristics. The box plots below the map are LiDAR cloud representations of three of the seven areas. The measurement points (276 points) surveyed in a 50 m x 50 m grid can be seen within each of the box plots. The remaining field areas maintained the equivalent experimental setup.

Table 1. Dates of snow sampling within the 2012/13 and 13/14 winter seasons. The snow depth measurements represent the total snow storm depth which fell in the Laret open field site. The remaining values, representing storm based values (swe – total storm swe, and temp - average storm temperature °C), are modeled.

storm date	snow depth (cm)	swe (mm)	temp (C)
13-Jan-2013	28.53	22.65	-3.9
22-Feb-2013	20.31	13.89	-12.1
6-Mar-2013	37.16	28.96	-4.2
20-Mar-2013	16.81	13.62	-3.5
27-Mar-2013	17.41	12.81	-5.7
15-Jan-2014	27.65	24.42	-2.4
28-Jan-2014	27.80	21.18	-4.7
17-Feb-2014	24.31	22.49	-1.9
24-Mar-2014	35.88	26.93	-5.1

4.2.2   Snow measurements

Snow depth data was manually collected after every storm with a total open area snowfall amount of 15 cm or greater in the winter 2012 and 2013 seasons. These measurements were collected at each forested point (1932 points) as well as at 100 open area control points (total of ~69000 measurements).Indirect snow interception measurements were collected when conditions allowed (table one). In some cases a crust formed over the previous layer before the subsequent snow storm. In these cases, it was possible to measure the newly fallen snow from the base of the underlying crust. These differential snow depth measurements were made during 9 storm events (table one) when the appropriate pre- conditions allowed: (1) forest canopy must be 100% snow free before a storm event, (2) minimal wind redistribution during the storm period and (3) obvious crust on prior snow layer. These measurements were taken immediately after the storm period was over in order to reduce, as much as possible, snow unloading. These assumptions allowed the differential snow depth measurements to be thought of as 1- snow interception, and were easily converted to interception within the sample areas (storm interception = newly fallen snow in the open – differential snow measurement in forest). The indirect storm interception measurements were subsequently parsed in order to remove any potential

conflicts with the necessary initial conditions and assumptions leaving ~9000 interception measurement points available for use.

4.2.3   LiDAR data

4.2.3.1   Technical details

LiDAR data acquisition was carried out from the 11th to the 15th of September 2010 using a Riegl LMS Q 560 sensor from a series of helicopter flyovers at a nominal flying altitude of 700 meters for a total area of ~90km2. The wavelength emitted from the Riegl device was 1550 nm with pulse durations of 5 ns and up to 7 returns were detected per pulse using a maximum scan angle of ±15°. The post processing of the full waveform data set yielded an average echo density of 35.68/m2 of the flyover domain and 19.05/m2 for the last returns (i.e. shot density) within the utilized domain area. The affiliated digital terrain model (DTM) or the underlying ground surface elevations were computed by using the classified ground returns at a 0.5 m horizontal resolution by Toposys using their in house processing software, TopPit (http://www.imagemaps.com/toposys.htm).

4.2.3.2   Polar system elements

LIDAR data was used to characterize the canopy at all measurement points in the field areas. Using the method of Moeser et al., 2014, the classical canopy descriptors, LAI and canopy closure were derived from a transformation of the ALS data into a spherical coordinate system (Figure 2, lower row). The ALS data was then flipped on the east west theta axis to represent an angular ground perspective. These data were converted in order to mimic hemispherical photos and further analyzed in a standard image analysis program, 'Hemisfer' [Schleppi et al., 2007; Thimonier et al., 2010]. Potential incoming solar radiation (PISR) and the affiliated direct and diffuse components were also estimated from this process. In this manner, LAI and CC were estimated with significantly higher correlations that using the standard Cartesian approach (r: 0.93 and RMSE: 0.037 for CC and r: 0.83 and RMSE: 0.813 for LAI). PISR showed similarly high correlations ranging from 0.90 to 0.94 dependent upon the field site. For details please refer to Moeser et al. [2014].
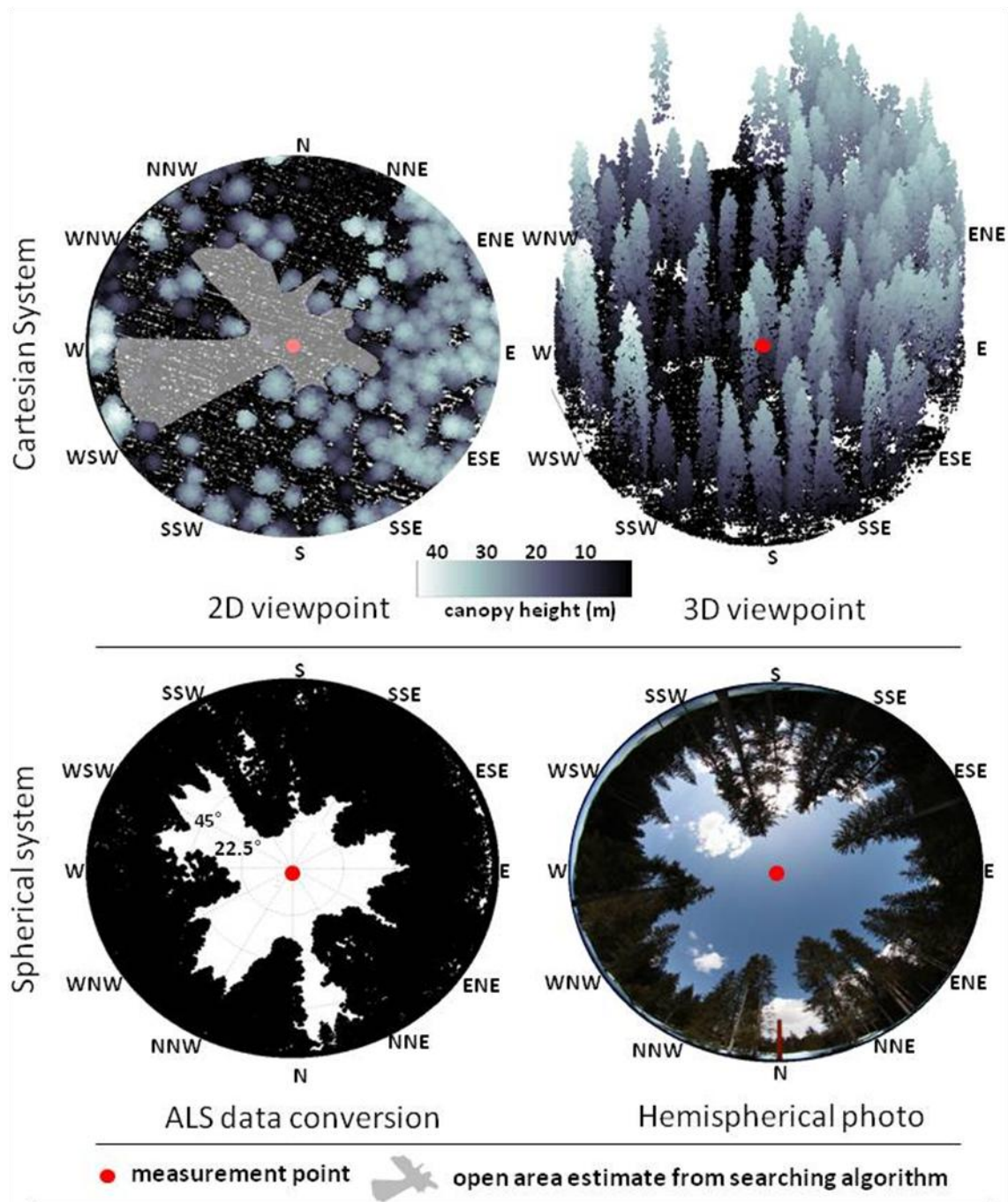
Figure 2. The LiDAR data is displayed in the standard downward looking Cartesian viewpoint on the upper row with an average echo density of 36 points/m2. The upper left image, displayed in a 2 dimensional format, includes an example of a polygon created from the vector searching algorithm. From these polygons, a variety of statistics can be estimated such as mean distance to canopy and total gap area. The lower left image is an example of LiDAR data converted to mimic a hemispherical image from an angular upward looking viewpoint. The lower right image is an actual hemispherical photograph. All images have been derived from the same point within an open area at the Laret low field area and have a data trap size of 100 meters (100 meter radius around point).

4.2.3.3 Cartesian system elements

A series of novel canopy descriptors were created from the ALS data for all snow sampling points from a vector searching algorithm. The algorithm searched the LiDAR data transformed into a 2 dimensional tree height model from a predefined center location approximately every two degrees on the planar surface. The tree height model was searched in 192 unique directions (~every two degrees) from vectors which originated from the predefined point. The vectors traveled in unique planar directions and did not stop until a canopy element from the tree height model was hit. Each vector was then given a distance (m) from the origin to the closest canopy element which was in the directional path of the vector (end point). The end points of each vector were connected and a 2 dimensional polygon was created. This shape (m^2) represents the total open area around a point and is referred to as total gap area (see the upper left tile of Figure 2 for an example of total gap area). The mean vector length (mean of the 192 vectors), which is called mean distance to canopy (m) was analyzed as well as the minimum (min distance to canopy), and maximum (max distance to canopy).

 Statistics from the total gap area (m^2) were also analyzed. The mean gap diameter (m), was defined as the mean diameter of the of the gap area. The max gap diameter (m) or the maximum fetch of the total gap area as well as the minimum (min gap diameter) were also calculated. The distance to canopy estimates (mean distance to canopy, max distance to canopy, min distance to canopy) were also calculated for 180 degree and 90 degree directional windows (north, south, east, west, northeast, southeast, southwest, and northwest). For example, a 180 degree search window of south searches all vectors from 90° (due east) to 270° (due west) and a 90 degree search window of south searches all vectors from 135° (southeast) to 225° (southwest).

A secondary domain with a 10 radius around each predefined point was used. Within these domains basic tree height proxies were estimated. Max canopy height, or the maximum height of the canopy elements within the domain as well as the mean canopy height, or the mean or all canopy elements within the domain were also calculated. A total of 57 canopy predictors were created from the vector searching algorithm automatically at each point. Table two displays all estimated canopy metrics. For a detailed method description refer to Moeser et al., [2015].

Table 2. Table modified from Moeser et al.,[2015]. Fifty-seven canopy metrics were created from the searching algorithm. Gap area and distance to canopy metrics were derived for the entire domain as well as for each directional sector from a 90 and 180 degree search window. The gap diameter metrics and canopy height proxies were generated only for the entire domain. Values within parentheses indicate number of times the descriptor was created.

Canopy Descriptors	The full domain	180°sector (N,S, E, W)	90°sector (N,S, E,
total gap area (m^2)	√	√ (4x)	√ (8x)
max gap diameter (m)	√	---	---
max distance to canopy (m)	√	√ (4x)	√ (8x)
min gap diameter (m)	√	---	---
min distance to canopy (m)	√	√ (4x)	√ (8x)
mean gap diameter (m)	√	---	---
mean distance to canopy (m)	√	√ (4x)	√ (8x)
max canopy height proxy (m)	√	---	---
mean canopy height proxy (m)	√	---	---

4.2.4 Data analysis

4.2.4.1 Snow depth to SWE conversion

In following with the methods utilized by Hedstrom and Pomeroy [1998] and Schmidt and Gluns [1991], the model from the US Army Corps of Engineers [1956] was utilized where snow density was related to the average storm temperature as follows:

$$\text{snow density} = 67.92 + 51.25\ e^{(T/2.59)} \qquad \text{eq. (1)}$$

where T is average storm air temperature (°C). The air temperature at each site, for each storm event, was interpolated based on an altitudinal gradient derived from surrounding meteorological stations. The interpolation utilized temperature data from 4 meteorological stations from the 'Intercantonal measurement and information system' (IMIS) surrounding Davos, Switzerland at four unique elevation bands: 1560 m, 2140 m, 2290 m, 2540 m (IMIS – KLO, IMIS – SLF, IMIS – PAR, IMIS – WFJ).

Equation one was then used to attached fresh snow density values to all measured snow depth values at each storm to arrive at SWE. Finally, the interception measurements were calculated from a simple subtraction of the freshly fallen SWE in the open – freshly fallen SWE in the forest.

4.2.4.2   Interception model

In accordance with the prior research from Satterlund et al [1967] and Schmidt and Gluns [1991], an initial increase in interception efficiency until a optimum (I_{max}) was reached along with a subsequent falling limb was seen within the plotted efficiency values at all canopy densities within this data set (figure 7). Due to this, the sigmoid growth curve proposed by Satterlund et al [1967] was used as the underlying model within this study:

$$I = \frac{I_{max}}{1+e^{-k(P-P_0)}}$$ eq. (2)

Where I is interception, I_{max} is the interception storage capacity (called S in prior studies), P is the storm precipitation, P_0 is the accumulated storm accumulation at the time of maximum interception efficiency and K expresses the efficiency rate. In prior studies, the factors, I_{max}, k, and P_0 were derived on a storm and tree species basis. Hedstrom and Pomeroy [1998] furthered this work by calculating I_{max} for trees from empirical values suggested from Schmidt and Gluns [1991], derived from snow density:

$$I_{max} = 0.27 + \frac{46}{\rho_{snow}}$$ eq. (3)

where ρ_{snow} is the density of fresh snow and multiplied this with LAI. Hedstrom and Pomeroy [1998] also used a static mulitiplier of 5.9 to this equation for spruce trees and defined Interception as:

$$I = 0.678 * I_{max} * [1 - e^{\frac{-CC*P}{I_{max}}}]$$ eq. (4)

Where 0.678 is a snow unloading multiplier valid for time after snow fall of 0 to 7 days.

The interception dataset was randomly divided into a calibration and a validation data set of 80% and 20% of total respectively. The Imax was calculated from a direct comparison of interception measurements from the calibration data set at the maximum efficiency event (13-Jan-2013) to all potential predictors (forest metrics). This included all parameters seen within table two, plus LAI, CC, incoming solar radiation as well as storm temperatures and fresh snow density. The parameters were then inter-compared using a correspondence analysis (CA) and K-means clustering analysis pairing in order to better understand how each of the variables related to each other.

4.2.4.3   Model Construction

CA is a non parametric principle components style analysis method specifically used for analyzing correspondence (or independence) among variables. This analysis has distinct advantages over traditional factorial analyses in cases where the analyzed data scales have a small response ranges. Within CA, the significance of data pairings is based upon the chi-squared distance between the actual and expected values [Car, 2002]. CA transforms the data into an 'equivalent' data space where the largest amount of data variability is captured within the first dimension (displayed as the x axis) the subsequent largest amount of variability in the second dimension (displayed as the y axis) and so on.

Each dimensional axis can further be given a significance value which represents the amount of variability the dimension (or axis) represents from the dataset (percent of inertia). Independence can therefore be qualitatively visualized by the separations distance between the plotted potential predictors (canopy metrics, etc) with greater significance given to separation distances seen on the axes with higher percent of inertia values. Specifically, small distances between points indicate a high association (cross correlation) and large distances indicate low association or independence. For a full mathematical description please see: [Car, 2002; Greenacre and Blasius, 1994; Lorenzo-Seva et al., 2009; Van de Velden and Kiers, 2003; Van de Velden and Kiers, 2005].

In order to reduce the potential bias in visual (qualitative) approaches such as CA, K-means clustering was used in order to quantify and automate the variable separations seen within the output of CA. K-means clustering was used to automatically choose groups of variables (canopy metrics) which plot similarly on the CA graph (Figure 4) by maximizing their inter cluster distances and minimizing their intra cluster distances [Seber, 1984; Späth, 1985]. The factor values (percent of inertia values) were integrated into the K-means routine and the routine was performed iteratively on the dataset where the centroid of each potential data cluster (grouping of variables) was randomly chosen. From prior work with similar datasets (interception ratio) the number of cluster groupings (k) was set to 4 [Moeser et al., 2015].

The component with the highest correlated value from each of the groupings was then used within a flexible regression modeling program. The program was fully automated and used the output of the CA / k-means clustering routine as input from the calibration data set. The program created a series of regressions for 1 variable, 2 variables, 3 variables and 4 variables with potential outputs being a (1) linear model, (2) linear model with component interaction (3) quadratic model and (4) quadratic model with component interaction. The input format of the variables was allowed to change between normal and log normal. This allowed for 16 potential models for 1 input variable, 112 potential models for two input variables, 96 potential models for three variables and 60 potential models for four variables for a total of 284 potential models. The program chose the best fit for each model scenario (1 variable model, 2 variable model, 3 variable model and 4 variable model) based on the lowest RMSE. The best fit Imax model scenario was then manually chosen from an analysis of the RMSE, correlation, visual analysis of the residuals and deviation of fit on the 1:1 line.

K and P_o were also subsequently optimized using the same method described above where k and P:

$$k = -\frac{\ln\left(\frac{Imax}{I}-1\right)}{P-P_0} \qquad\qquad \text{eq. (5)}$$

$$P_o = -\frac{\ln\left(\frac{Imax}{I}-1\right)}{-k} + P \qquad\qquad \text{eq. (6)}$$

However due to extremely low correlations of k and P_0 to any of the variables, these values were also used as constants. Equation 2, with the integration of the new Imax model, was explicitly solved from a series of given input values for k (between -1 and 1) and P_0 (between minimum and maximum P swe values) where the optimized values were derived from the minimization of the RMSE of the estimated and actual interception values from the calibration dataset.

4.2.4.4   Model upscaling

It is possible interception simulations based on a single model run using averaged canopy parameters over a grid area could be systematically offset as compared to interception averaged over individual point based model runs using local canopy parameters. In efforts to reduce the potential of systematic

bias upscaling from a point to larger scales, a stratified model approach was also integrated in to the model.

For upscaling from a point to a grid, the domain was split into a series of grid cells ranging from 16m^2 to 62500 m^2, where all internal measurement points within each grid cell were averaged. The grid sizes were chosen in order to avoid any overlap or sharing of internal grid points to neighboring grid cells of the same size. See figure 3 for an idealized representation of a field area and the grid domains. The 16m^2 grids included five internal measurements points within each grid for a total of 575 grids utilized for this study, the 64m^2 grids contained 9 points with a total of 575 grids utilized, the 200m^2 grids contained 67 points with a total of 143 grids utilized, the 2500 m^2 grids contained 276 points with a total of 35 grids utilized and the 62500 m^2 grids contained 1380 points with a total of 9 grids utilized.

The same approach was utilized as outlined above (section 2.4.3) to create the stratified model except the regressions were further parameterized using two threshold values governed by a canopy parameter. For example, if LAI was chosen as the parameter, with the threshold values being 3 and 5, the modeling domain would therefore be clustered into 3 zones (1) LAI ≤ 3, (2) 3<LAI<5, and (3) LAI ≥5 where a separate model would be utilized for grids or points in each of the three zones.

In order to choose the correct parameter as well as the threshold values of that parameter, dummy variables were integrated into the regression analyses which were given values of either 0 or 1, dictated by the two threshold values. A list of the threshold value pairs were automatically created by the program by first separating the range of the utilized parameter values into a series of equidistant step values (up to 100). These values (threshold one) were attached to a value from the same list of step values as long as the step size was greater than the first threshold (threshold two). For example, if LAI was used and ranged from a LAI of 1 to a LAI of 4, the equidistant step would range from 1 to 4 and the threshold pairs would be, 1,2 : 1,3 : 1,4 : 2,3 : 2,4 : 3,4. If the threshold pair, was 1,3: then the domain would be clustered into three zones: (1) LAI ≤ 1, (2) 1<LAI<3, and (3) LAI ≥3. Two extra variables (dummy variables) would be used within the regressions, with the first variable displayed as 1 when LAI

was ≥ 1 and 0 when LAI was < 1 and the second variable displayed as 1 when LAI was ≥ 3 and 0 when LAI was < 3.

The best fit threshold pair was optimized from a minimization of the RMSE when each regression run that utilized the threshold pairs was analyzed. The canopy parameter was also left flexible, where the program, as with the threshold values, also chose the best parameter based on a RMSE minimization. When the best fit run was found, the regressions were decomposed based upon the dummy variables giving unique equations for each range (3 equations for two thresholds).
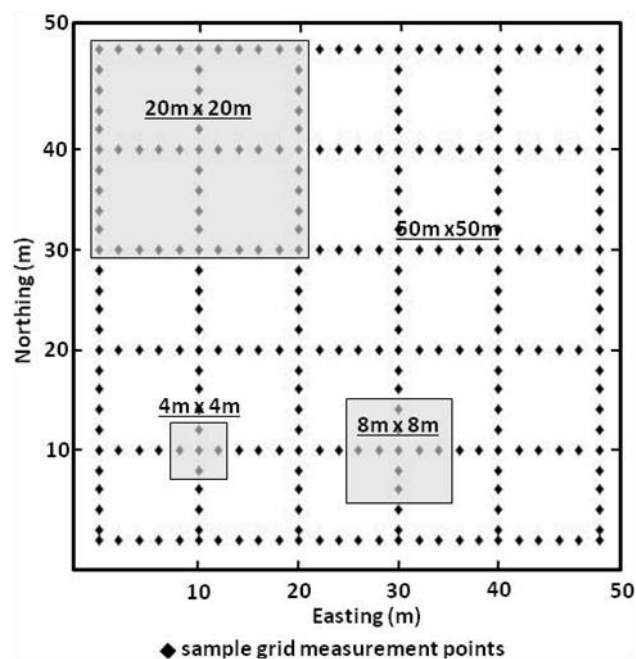

Figure 3. Represents an idealized sampling grid (276 points) and grid cells. The grid cells were created in order to avoid any sample point sharing between grid cells. The 4mx4m grid cells contained 5 measurement points for a total of 16 per field area, the 8mx8m grid cells contained 9 points for a total of 16 per field area, the 20m x20m grid cells contained 67 measurements points for a total of 4 per field area, the 50mx50m grid cells contained 276 points and the 250m x 250m grid cells, which was a composite of 5 field sites, contained 1380 points.

4.3 Results and Discussion

4.3.1 Canopy parameter analysis

The generated canopy parameters varied greatly through space. For example, LAI varied from ~1.2-8.0 and total gap area varied from ~0 to 2270m^2. Figure 4 shows the CA / k-means clustering analysis of all canopy parameters. The traditional canopy descriptors, LAI and CC along with mean tree height showed a high degree of cross correlation (cluster one) and the strongest member (highest correlation to interception at Imax) was canopy closure (R: 0.76). The next smallest cluster grouped all area (total gap area, gap area to the north, gap area to the northeast, etc) estimates except those which had a southerly direction, with the strongest end member being total gap area (m2) (R. 0.76). The next cluster contained all direct incoming solar radiation components as well as distance to south and area to the south estimates with the strongest member being average daily PISR (R: 0.71). The largest cluster included all distance estimates except those to the south and diffuse incoming radiation estimates with the strongest end member being mean distance to canopy(m) (R. 0.83). Contrasting with the use of fresh snow density in the model framework (equation 3) utilized by both Schmidt and Gluns [1991] and Hedstrom and Pomeroy [1998]; fresh snow density showed extremely low correlations (along with storm temperature) within this dataset. Due to this, these parameters were not included in the CA / k-means clustering analysis(R <0.10). The correspondence / k-means clustering analysis gave similar results from prior analyses of all parameters to interception ratio (differential snow measurement in forest / newly fallen snow in the open). For a thorough results analysis of the CA/ k-means in regards to interception ratio, see Moeser et al. [2015].
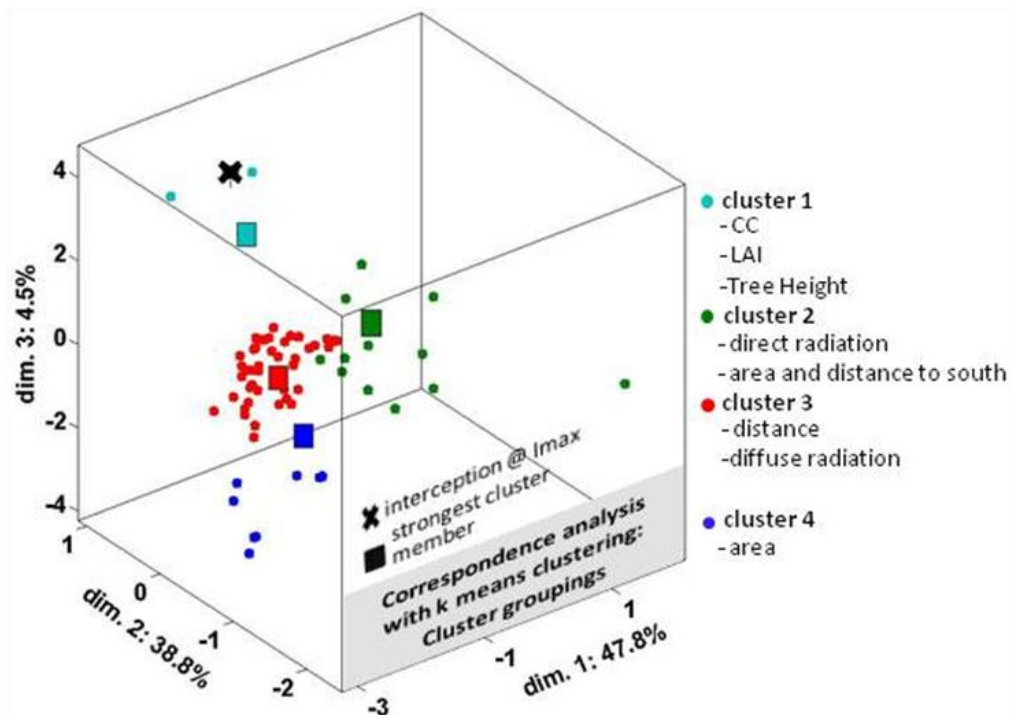
Figure 4. The parameter groupings within the correspondence analysis were chosen by k-means clustering with each group labeled by color. Each box within the colored grouping shows the highest correlated element within the grouping. The highest ranking member of group one was canopy closure (R: 0.76), group two was mean distance to canopy (R: 0.83), group three was daily average PISR (R: 0.71) and group four was total open area (R: 0.76). The cross represents the location of the independent element, snow interception at maximum efficiency.

4.3.2 I_{max}

Imax was best estimated from the integration of 3 variables obtained from the aerial LiDAR data, (1) mean distance to canopy(m), (2) canopy closure, and (3) total gap area (m2) with a RMSE of 2.82 mm SWE, and an r square of 0.75 (R: 0.86). See figure 5. The integration of the 4th cluster grouping from the CA analysis (PISR) added little skill to the final model and was subsequently omitted. Mean distance to canopy was created from the vector searching algorithm and represented the average distance to the closest canopy feature. Total gap area was also created from the vector searching algorithm and was an estimate of the total gap area from the perspective of the measurement point. Canopy closure was derived from conversion of the ALS data into a spherical coordinate system in order to create synthetic hemispherical photographs. The Imax model and affiliated coefficients are shown in Eq. 6 and table three. The Imax values within this study are considerably higher than in the prior works of Satterlund and Haupt [1967] and Schmidt and Gluns [1991]. However and as noted in

these papers, extrapolating results from branches and saplings to trees should exhibit increases in Imax values primarily from increased snow bridging effects from higher snow particle drop-off from upper to lower branches.

The Imax model proposed by Hedstrom and Pomeroy [1998] , utilized LAI as a multiplier to equation 3 along with a static multiplier of 6.6 (for spruce trees). However the CA / k-means analysis showed reduced correlation when LAI (R: 0.58) was directly compared to interception as with CC to interception(R: 0.76). Correlations of snow density to interception were also minimal. This implies that at least when storm based I_{max} is estimated, (1) CC gives better estimations of Imax than that of LAI and (2) the surrounding canopy elements appear to play a larger factor on Imax than the density of the falling snow.

Table 3. Imax was derived from the highest efficiency storm event (13-Jan-2013) and is represented as a quadratic equation with the independent variables described from aerial LiDAR data.   Each variable was transformed using the natural log. Imax has units of mm of SWE.

variable (log)		m1	m2	b
X1 --	mean distance to canopy (m)	2.167	-3.410	
X2 --	canopy closure	55.761	181.858	20.819
X3 --	total open area (m^2)	-2.493	0.499	

$$I_{max} = m1(x1) + m2(x1)^2 + m1(x2) + m2(x2)^2 + m1(x3) + m2(x3)^2 + b \qquad\qquad eq.(7)$$
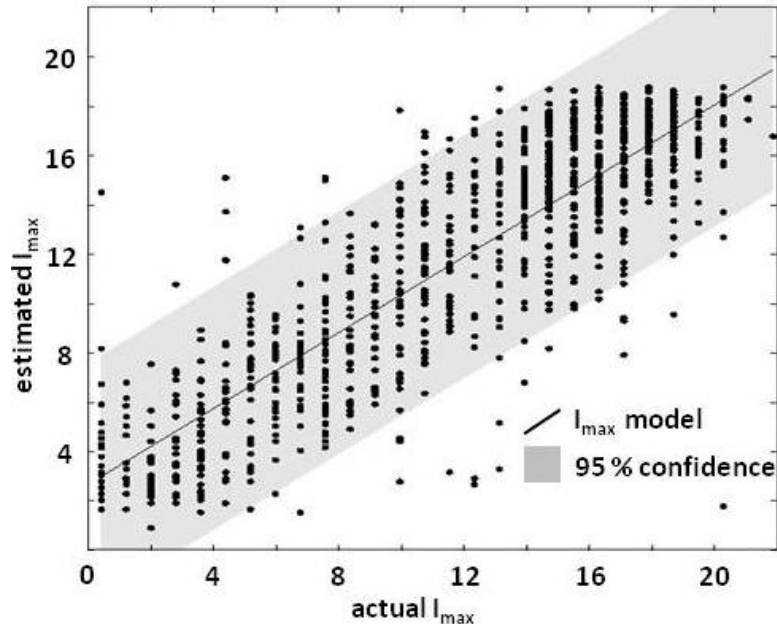
Figure 5. Compares Imax estimated from the model with the actual Imax values from the 13-Jan-2013 storm event. The model is represented as a black line with a RMSE of 2.82 mm SWE, and an r square of 0.75 (R: 0.86). The 95% confidence interval of the model is seen as grey shading.

4.3.3   Interception

K and P_0 had negligible correlations to all canopy parameters as well as to storm temperature and snow

density (eq. 4 and eq. 5). Due to this the K and P_0 were optimized from a minimization of the RMSE to

0.3 and 13.3 respectively. Interception is therefore:

$$I = \frac{I_{max}}{1+e^{-0.3(P-13.3)}}$$ eq. (8)

Where I is interception in mm, and I_{max} is eq. 7. The model can be used at sub storm event time scales

from integration of the underlying efficiency distribution. Therefore, P can be input at each time step as

a summation of precipitation from when I > 0 (start of storm period). However, this model was created

from data collected immediately after storm events, it inherently integrates unloading that occurs during

the storm event. Due to this, such a model should not be used in tandem with an unloading function

during storm events.
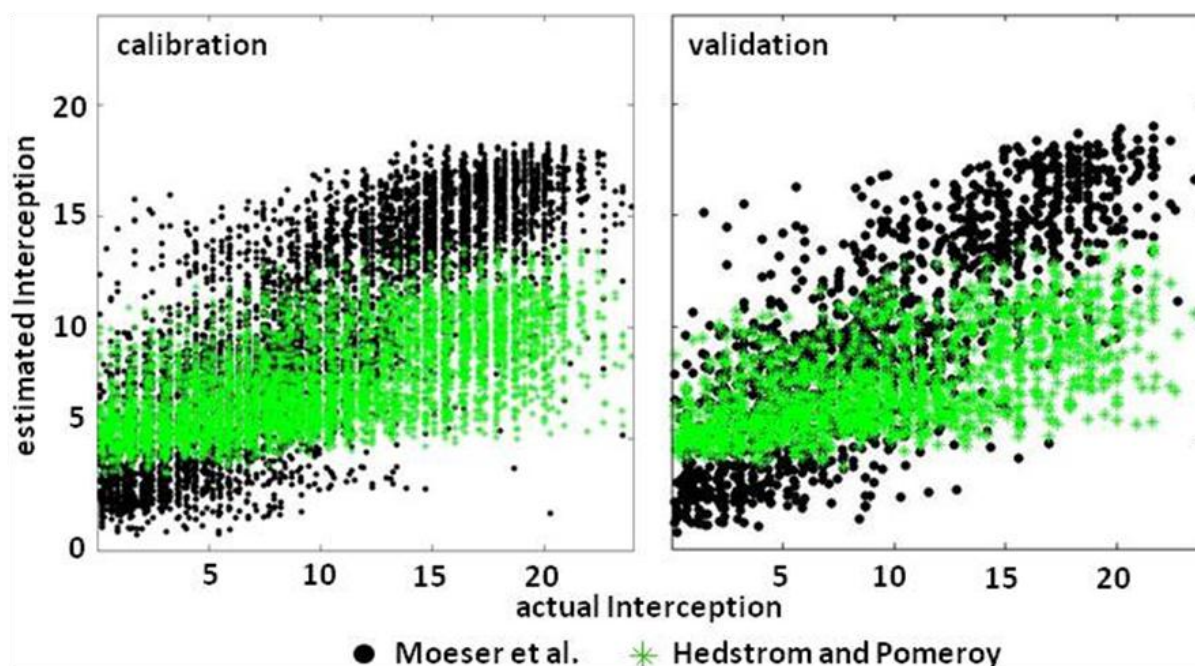
Figure 6. Performance comparison of the proposed interception model (Moeser et al.) to the model by Hedstrom and Pomeroy (1998). The calibration data (upper left) and the validation data (upper right) showed similar trends. The Moser et al. maintained an r square of 0.65 / RMSE of 3.39 mm SWE, from the calibration data and an r square of 0.64 / 3.4 mm SWE, RMSE in the validation data. The Hedstrom and Pomeroy model showed an r square of 0.39 / RMSE of 5.19 mm SWE, within the calibration data and an r square of 0.41 / 5.18 mm SWE, RMSE in the validation data and showed a substantial interception underestimation in both data sets.

The model fit both the calibration and validation data sets well with an r square ranging from 0.64 – 0.65 (R: 0.81) and an RMSE from 3.39 to 3.4 mm SWE (figure 6). The sigmoidal shaped efficiency model distribution (left tile, figure 7) shows a good fit with the actual data from each storm event (figure 8).

The Hedstrom and Pomeroy model showed an r square ranging from 0.39 – 0.41 for the calibration and validation data sets as well as an RMSE ranging from 5.18 - 5.19 mm SWE. This model showed a severe interception underestimation with estimated interception values over ~5, with the opposite holding true for values under this range. This is most likely due to the underlying efficiency distribution inherent within this model, which does not apply to this data set. Figure 7 exhibits the basic distribution differences between the two models. The Hedstrom and Pomeroy demonstrated an exponential decay of the efficiency from the beginning of snow fall, whereas the Moeser et al. showed an initial increase in efficiency until I_{max} was reached, at which point the efficiency dropped exponentially. These differences

were especially visible when the interception efficiency from the models were compared to the measured efficiency from each of the storm events (figure 8).
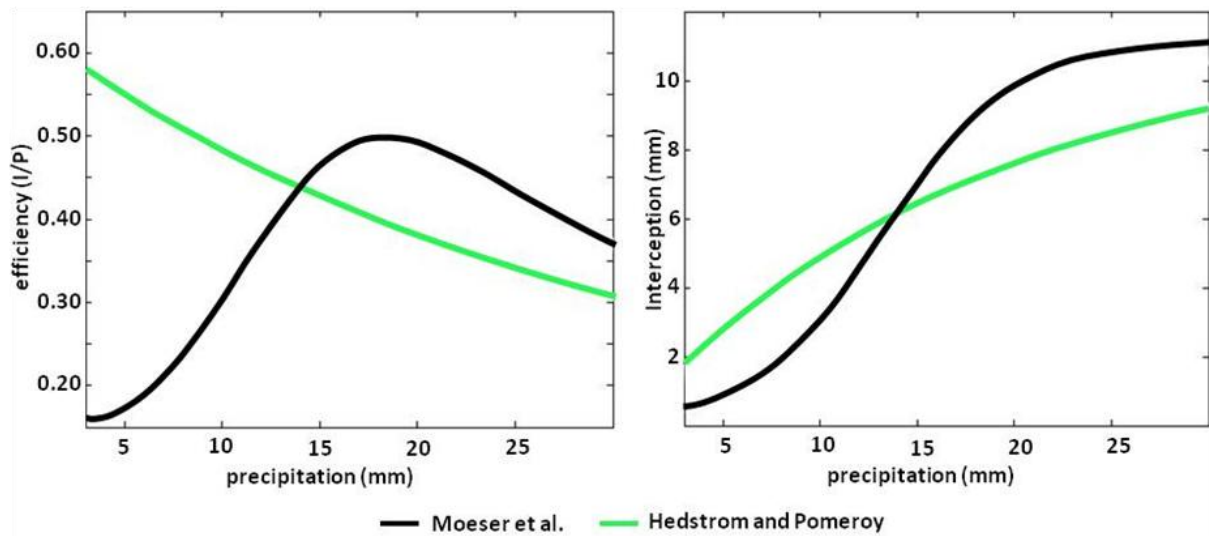

Figure 7. Comparison of interception model estimation distributions using mean canopy values and a precipitation data series from 1 to 30 mm with a 0.1mm step. The Moeser et al. model is seen in black and showed an initial exponential increase in efficiency before decreasing. The Hedstrom and Pomeroy model (in green) showed an exponential decrease in efficiency starting from zero. The Moeser et al. interception model showed an exponential increase (with the highest slope at P0) until Imax was reached at which point estimates level. The Hedstrom and Pomeroy showed increasing interception estimates with a slow reduction in slope until a maximum is reached.
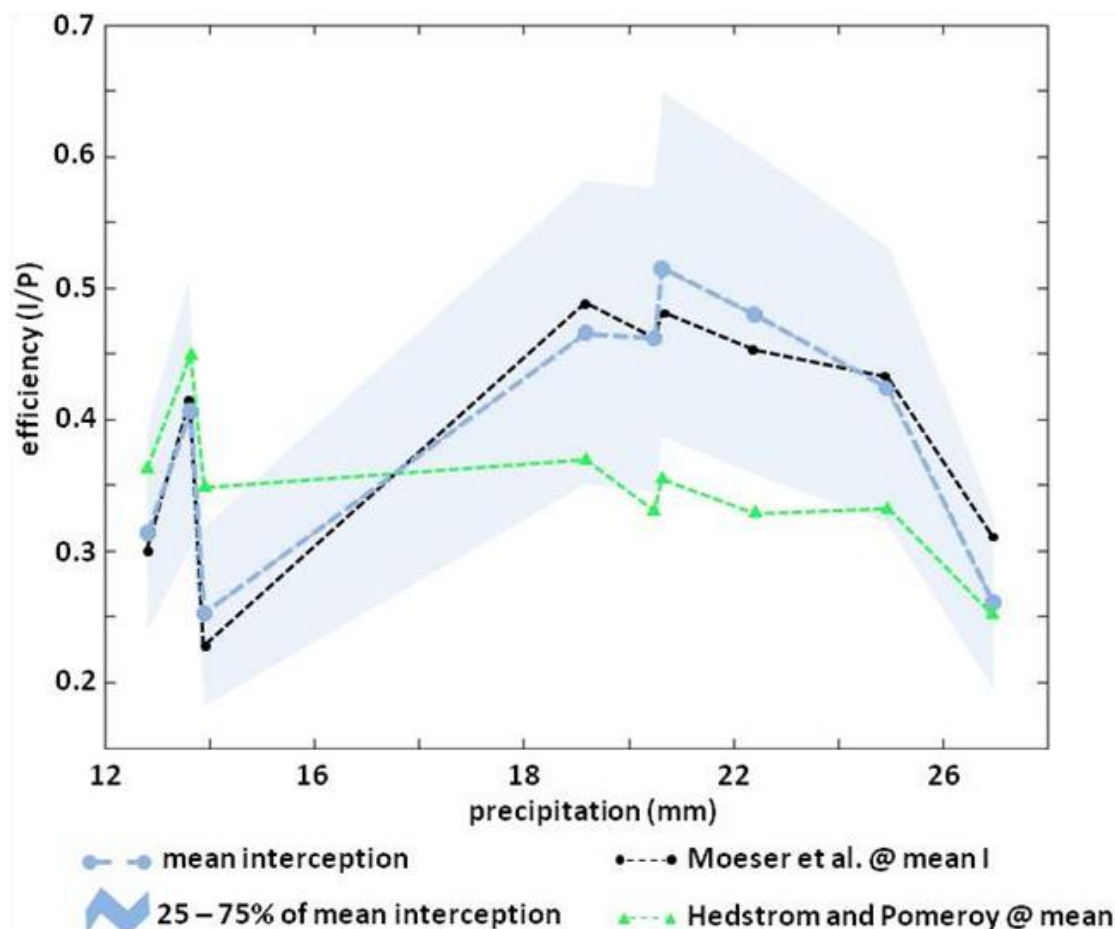
Figure 8. Comparison of measured interception efficiency from the 9 storm events (table 1) where mean efficiency from each event is shown in dark blue circles. The efficiency values ranging from 25% to 75% of mean interception are shown as a light blue band. Mean modeled efficiency values from the Moeser et al. model are shown as small black circles. The mean values from the Hedstrom and Pomeroy model are shown as green triangles. Note the large mean efficiency underestimation from the Hedstrom and Pomeroy model.

4.3.4   Parameter analysis

As noted in section 3.2.2, the Hedstrom and Pomeroy [1998] model utilized LAI as a principle parameter to estimate I_{max}. This is further integrated within the Interception model and used as a divisor to CC and precipitation for the exponential decrease portion of the model [Hedstrom and Pomeroy, 1998; Pomeroy et al., 1998]. However, when used with this data set, the paring of these two parameters (LAI, CC) could cause potential cross correlation within the model (see section 3.2.1) highlighting the necessity of parameters which describe varying aspects of the overstory.
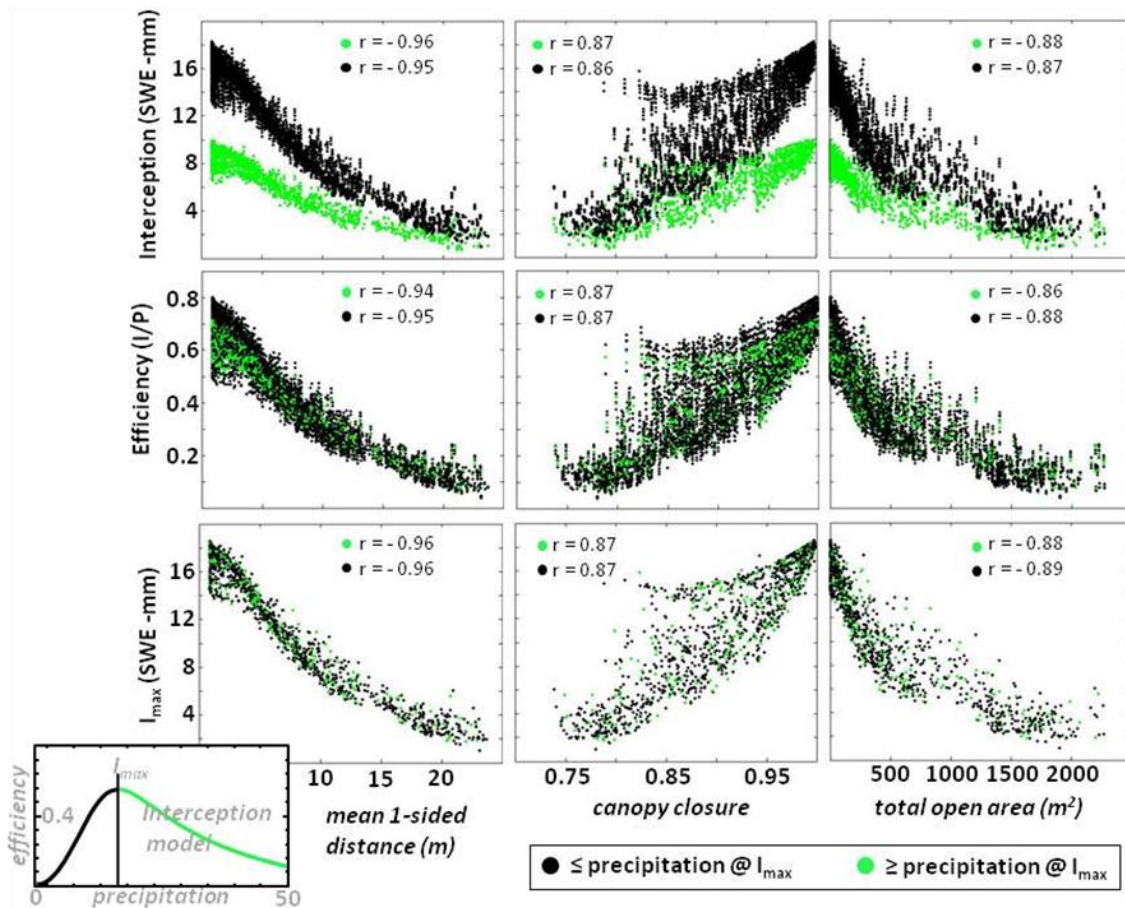
Figure 9. All dependent canopy parameters within the interception model showed high correlations to Interception (top panel), efficiency (middle panel) and Imax (lower panel) and each resolved high percentages of explained model variance. Mean distance to canopy was the most skilled variable within the model and maintained low internal variance and high correlations for the entire variable domain. Canopy closure retained the highest correlations and lowest variance at both high and low values with the median values showing the highest parameter variance. Total open area maintained a fairly uniform correlation. However this parameter had a fairly distinct zone where parameter variance increased (500-1000 m2).

Each independent canopy parameter within the Moeser et al. interception model (mean distance to canopy, canopy closure, and total gap area) was visually analyzed for sensitivity to I_{max}, efficiency and total interception (figure 9). Mean distance to canopy showed the highest skill, with high correlations and low variance for the entire data series. Canopy closure demonstrated higher correlations and lower variance for both high and low canopy closure values, with increased variance present within the median values. Total gap area maintained equivalent correlations. However this parameter demonstrated a fairly distinct zone where the line slope changed and variance increased (~500-1000 m^2). The separation between Interception >Imax and Interception <Imax showed no significant mixing

until mean distance to canopy was ~greater than 18m. Interestingly this threshold came much sooner in the data range of canopy closure (~less than 0.92) and total open area (~greater than 250). This implies that the lowest efficiency ranges (where mean distance to canopy is high, total open area is high, and canopy closure is low) are best captured by mean distance to canopy. The independent variable correlations at I_{max} (eq. 7) showed no significant reductions when this was used within the interception model (eq. 8) also lending significance to the underlying sigmoidal model distribution curve.

4.3.5   Model upscaling

When the modeling domain was stratified, the canopy parameter which demonstrated the lowest reductions in RMSE was total open area with the affiliated thresholds optimized at (1) 250 m^2 and (2) 750 m^2. This created a separate model for three open area zones: (1) total open area ≤250 m^2 (2) total open area >250 m^2 & < 750 m^2 and (3) total open area ≥ 750 m^2. The independent parameters are the same as the point based model (equation 7 and table 3), with the same underlying quadratic format and natural log conversion of independent variables. However, the coefficients have changed for each parameter from the point based equation. From a decomposition of the regression model, the dummy variables were removed giving unique intercept values for each open area group (table 4).

Table 4. Model coefficients and intercepts for the stratified model. Eq. 7 and 8 remain the same.

variable (log)	m1	m2	(open area ≤ 250 m^2)	(250 <open area <750m^2)	(open area ≥ 750m^2)
			Intercept values		
x1	1.275	-3.292			
x2	53.324	169.89	20.895	19.895	18.895
x3	-2.598	0.567			

Table 5. Basic statistics comparing the stratified model and the Hedstrom and Pomeroy at various grid sizes. The stratified model maintained an RMSE (mm SWE) approximately half that of the Hedstrom and Pomeroy for all grid sizes as well as a doubling of the standard deviation (mm SWE) at all grid sizes representing the estimation spread and subsequent underestimation of the Hedstrom and Pomeroy at all grid sizes. See figure 10 for a visual representation.

|	$16m^2$		$64m^2$		$400m^2$		$2500m^2$		$62500m^2$	
	M et al.	H and P	M et al.	H and P	M et al.	H and P	M et al.	H and P	M et al.	H and P
r^2	0.78	0.52	0.85	0.62	0.86	0.76	0.91	0.82	0.91	0.89
rmse	2.54	4.54	2.24	3.93	1.73	3.08	1.31	2.86	0.93	1.90
stdev	4.79	2.21	4.96	2.41	4.49	2.30	4.14	2.11	2.75	1.39
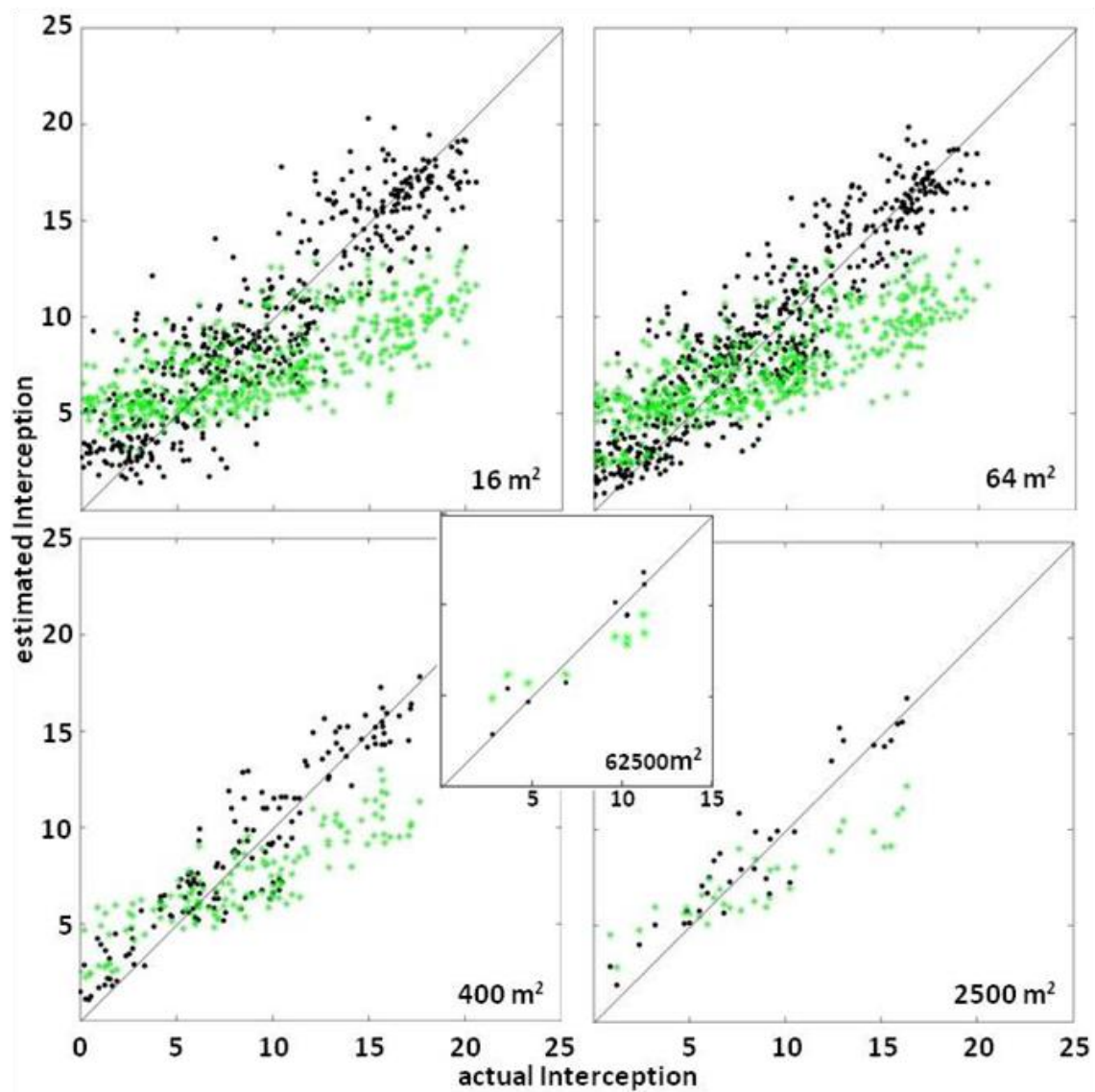
Figure 10. Comparison of the stratified model to the Hedstrom and Pomeroy model from 16m2 to 62500m2 grid sizes. While each model displayed an improved fit as the grid size increased, the Hedstrom and Pomeroy model demonstrated a significant underestimation at all grid sizes. See table 5 for a list of general statistics of each model. The point model derived similar results as to the stratified model.

The stratified model showed an improvement in the RMSE by a factor of 1.75 to 2.18 when compared to the Hedstrom and Pomeroy model at each grid scale. The standard deviation of the estimated interception was also higher by a factor of 1.95 – 2.17 within the Moeser et al. stratified model. These differences represented fairly substantial underestimations of interception as well significant spread in estimate confidence within the Hedstrom and Pomeroy model. However, both models showed an r square increase at each grid size, due to the smoothing of data.
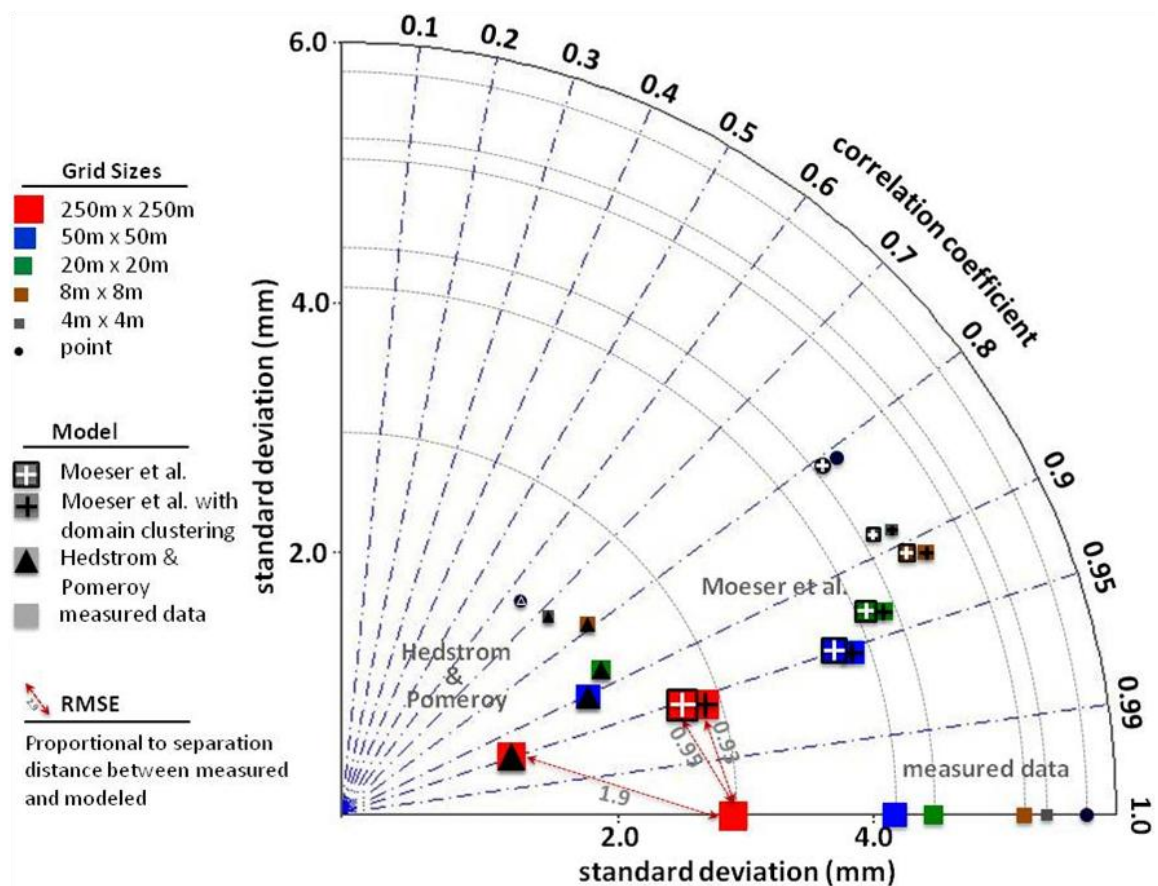

Figure 11. Taylor diagram comparing the: (1) Moeser et al point model (2) Moeser et al model with a stratified approach and the (3) Hedstrom and Pomeroy model at the point scale and all grid sizes from 16m2 to 62500m2. The standard deviation of the estimates and the actual data are plotted on the linear axes and represent the over or underestimation of the models. Model estimates that plot to the right of the actual data (for the appropriate grid size) represent an overestimation and model estimates which plot to the left represent and underestimation. The correlation is plotted on the log scale axis. RMSE at each grid size is directly proportional to the distance away from the actual data. The red arrows between the 62500m2 grid series show the distance: RMSE relationship, with the RMSE values labeled in light grey. The Moeser et al. models showed improved skill at all grid sizes. The stratified approach, while showing negligible improvement in RMSE or correlation, showed slight improvements in estimation power from an improved representation of the datasets variability and resulted in smaller underestimations.

When the point based model was utilized for the grids, the results showed insignificant increases in the r square and RMSE (r square: 0.65 - 0.66 RMSE: 3.39 - 3.38) as compared to the stratified approach. Despite this, increased variability of the data was captured within the stratified model, which slightly improved estimates at all scales. Figure 11 is a Taylor plot of the models: (1) Moeser et al. point model, (2) Moeser et al. model with a stratified approach and the (3) Hedstrom and Pomeroy model at all scales. Due to the geometric relationships of the plotted statistics, the skill of the model can be quantified by both distance to the measured data as well as distance to the standard deviation lines of the measured data [Taylor, 2001]. The Pomeroy showed large underestimations for all grid sizes. The Moeser et al. point model showed smaller underestimates with improvements from the stratified approach at all scales.

4.3.1.6   Model improvement: efficiency distribution vs. canopy structure metrics

In order to differentiate how much of the modeled interception improvement was due to the use of canopy structure elements and how much to the sigmoidal interception distribution; we have created a model where Imax was estimated using just CC. The exact methodology which used in the prior models was implemented to create this comparative model, where Imax is:

$$I_{max} = 71.55(CC) + 64.39(CC)^2 + 17.71 \qquad\qquad eq.(9)$$

$$I = \frac{I_{max}}{1+e^{-0.29(P-13.2)}} \qquad\qquad eq.~(10)$$

Where CC was log transformed and k and Po have been optimized to 0.29 and 13.2 respectively (eq. 10). The model was fit to both the calibration and validation data sets with an r square which ranged from 0.49 – 0.53, and a RMSE of 3.96 for both data sets. This implies that for the calibration data set, ~48% of the improvement in the r square and ~67% of the improvement in RMSE is due to the inclusion of canopy structure metrics (mean distance to canopy and total gap area). While it was not possible to fully separate the underlying model distribution and the variables, this shows that in general the improvement is due to both, the underlying sigmoidal distribution as well as the inclusion of canopy metrics which describe the overall canopy structure (mean distance to canopy and total gap area).

It should be noted, that the Hedstrom and Pomeroy interception model was created in a cold boreal forest environment. Despite this, it is the only know model which the authors are aware which has been integrated into snow melt models which have a forest canopy module. This should emphasize that there may be a need for an alternative model which can better perform in other environments.

4.4   Conclusion

Storm based interception was accurately predicted across a large range of canopy closure and gap opening regimes (from $0m^2$- $2250m^2$) from a database which included approximately 9000 manually measured interception points at 1237 independent points. The size and heterogeneity of both the calibration and validation datasets eclipses prior datasets utilized from interception modeling studies input data by over an order of magnitude. The model showed a good fit with increased performance dependent upon the grid cell size with r square values ranging from 0.65 at the point scale to 0.91 at the largest $62500m^2$ grid scales. The RMSE showed a similar trend and ranged from 3.35 mm SWE to 0.93 mm SWE.

The stratified model results showed modest improvements in interception estimations with the most obvious benefits being an increase in variation captured within the interception dataset (figure 11). While the inclusion of a stratified model approach did improve the model at larger scales, it seems likely that the inclusion of parameters which describe large scale features such as canopy gaps (total open area) are sufficient alone to reduce the potential of systematic bias when upscaling from a point to larger grid sizes. However this needs to be further tested on scales larger than $62500m^2$ (the maximum allowable domain size within this study).

The distribution of storm based events within this dataset showed an underlying sigmoidal shaped distribution similar to prior interception studies [Satterlund and Haupt, 1967; Schmidt and Gluns, 1991]. Akin to those studies, this data showed an initial efficiency increase until I_{max} was reached at which point the efficiency demonstrated a clear falling limb.

This model was compared to the most used snow interception model to date [Essery et al., 2009; Hedstrom and Pomeroy, 1998] and showed an r square increase of 25% for the point scale as well as a

reduction in the RMSE by 53%. At all grid scales, the Hedstrom and Pomeroy model showed an RMSE increase of 75 – to 114% when compared to the Moeser et al. model. The Moeser et al. model showed a minor underestimate of all estimated interception values. However, when compared to the Hedstrom and Pomeroy model, this underestimate is reduced by ~40%. The principle deficiency leading to the substantial interception underestimates within the Hedstrom and Pomeroy model was due to the underlying exponential decay interception efficiency distribution. These underestimates were further offset from the use of an I_{max} equation (equation 3) which integrated unique tree species specific multipliers from a study which derived them from the branch scale. As Schmidt and Gluns [1991] notes, extrapolating results from branch interception to that of a tree would exhibit efficiency and interception values greater than that for a single branch due to the increased probability of lower canopy structures collecting particle bounce.

The paired correspondence and k-means cluster analysis showed higher correlations of I_{max} to the novel canopy descriptors than LAI and canopy closure. Mean distance to canopy yielded the highest correlations to I_{max} (R: 0.83) and was the most significant variable within the model. This variable also increased model performance at low interception efficiency ranges and helps when usings a gridded modeling approach in terrain with heterogeneous to light canopy. Total open area (R. 0.76) also showed high correlations to Imax and no cross correlation issues with mean distance to canopy or canopy closure. The I_{max} integrated within the Hedstrom and Pomeroy model utilized fresh snow density and LAI. However the initial correlation analysis showed reduced correlation of I_{max} to LAI (R: 0.58) as compared to canopy closure (R: 0.76). Correlations of fresh snow density were also minimal implying that at least when storm based I_{max} is estimated, (1) the overhead canopy elements play a larger part than the density of the falling snow and (2) the use canopy closure give more robust estimations than LAI. The analysis also showed a high degree of cross correlation between canopy closure, LAI and mean tree height negating the utility of a pairing of CC and LAI in one model.

The independent parameters from this model are easily derived pending the existence of aerial LiDAR data and the vector searching algorithm scripts used within this study can be easily transferred to other datasets. All scripts related to this algorithm are freely available upon request.

Representing spatial variability of forest snow: Implementation of a new interception model

D. Moeser[1, 2], G. Mazzotti[1], N. Helbig[1], T. Jonas[1]

[1]WSL Institute for Snow and Avalanche Research SLF, Davos Dorf, Switzerland
David Moeser: moeser@slf.ch   Giulia Mazzotti: giulia.mazzotti@slf.ch   Nora Helbig: helbig@slf.ch   Tobias Jonas: jonas@slf.ch

[2] Forest Ecology, Institute of Terrestrial Ecosystems, Department of Environmental Sciences, Swiss Federal Institute of Technology ETH, Universitätstrasse. 16, CH-8092 Zurich, Switzerland

Corresponding author address:
David Moeser, WSL Institute for Snow and Avalanche Research SLF, Fluelastrasse 11, CH-7260 Davos Dorf, Switzerland. Email: moeser@slf.ch, phone: 0041 (0)81 4170 156, fax: 0041 (0)81 4170 0110

Abstract

A new interception model was integrated in a snowmelt model and for the first time the spatial variability of forest snow was effectively represented due to the inclusion of new forest structure metrics. The model was tested at 1273 field points surrounding Davos, Switzerland, that feature an extremely wide range of canopy and forest structure. The behavior of the new model was compared against a widely applied interception model. Due to the inclusion of novel forest structure parameters (mean distance to canopy and total gap area) in the new model, simulated interception mimicked the horizontal layout of canopy structure, while the standard interception model yielded fairly homogeneous interception

estimations even under highly heterogeneous canopy conditions. The large variance of estimated interception between points using the new model translated into significant effects on under-canopy snow water equivalent and snow depth. Precipitation conditions were also analyzed, and further differences between the models were related to storm intensity. In climates characterized by large storm events, the new interception model provides significantly higher interception estimations (i.e., lower under-canopy snow) than the standard model, whereas in climates characterized by small storms events, the new model yields lower interception estimations (i.e., higher under-canopy snow) in areas with moderately sized to large canopy gaps.

5.1 Introduction

Forests directly impact the snow accumulation and melt cycles over large areas. In the Northern Hemisphere, 20 percent of the seasonal snow cover occurs within forested regions, which accounts for 17 percent of the total terrestrial winter water budget [Guntner et al., 2007]. Primarily, the presence and structure of forest canopy affects the under-canopy snow distribution due to snow interception on the canopy and processes that lead to the release of intercepted snow, such as snow unloading and sublimation. Besides major implications for the water budget, the interplay of these mechanisms also affects albedo and the related energy transfer processes in forest regions.

Intercepted snow estimates range from 0 to 80 percent of the total annual snowfall within forested areas and the longer intercepted snow remains in the canopy, the more sublimation can occur [Martin et al., 2013; Moeser et al., 2015b; Montesi et al., 2003; Storck et al., 2002]. Due to this, the spatially heterogeneous nature of interception leads to equally heterogeneous sublimation rates, which vary from 0 to 50 percent of the total annual snowfall in forested areas [Essery and Pomeroy, 2001; Essery et al., 2003; Hedstrom and Pomeroy, 1998; Lundberg and Halldin, 2001].

Many studies that have focused on forest-snow interactions, with initial research starting over 100 years ago. To date there have been four synthesis reviews of these efforts, which all highlight the complex nature of forest-snow interactions as well as sometimes disparate interception measurement methods

and results [Bunnel et al., 1985; Friesen et al., 2014; Lundberg and Halldin, 2001; Varhola et al., 2010b]. In 2007, an assessment of the skill of current snowmelt models that include representations of canopy-snow interactions (Snow model inter-comparison project – SNOWMIP2) was undertaken [Essery, 2009; Rutter et al., 2009]. Within this project, not only was no best fit model found for the sites included in the study, but model performance showed much lower consistency for forested areas than for open areas. These findings underscore the sometimes overly simplistic representation of canopy structure in the underlying processes. All the models in SNOWMIP2 that utilized a snow interception module integrated canopy closure (CC) and / or leaf area index (LAI) to parameterize the canopy. However, prior studies showed that field points that have the same LAI or CC can have different large-scale canopy structures, such as open areas surrounding these points [Moeser et al., 2015a; Moeser et al., 2015b]. Furthermore, the importance of the greater forest structure has also been highlighted as a major factor dictating the under-canopy SWE accumulation patterns and timing of snow melt [Golding and Swanson, 1986; Lopez-Moreno and Latron, 2008; Lopez-Moreno and Stahli, 2008; Troendle and Meiman, 1986; Varhola and Coops, 2013; Varhola et al., 2010a; Veatch et al., 2009; Winkler and Moore, 2006; Winkler et al., 2005].

Despite the large amount of research on the interactions between forest canopy and snow, few studies have attempted to quantify this in the form of a mechanistically relevant interception model that can be integrated in a snowmelt model. Storck [2000] created a model for maximum interception capacity based on data from the Pacific Norwest of the US in the form of a temperature-based stepwise function that integrated LAI, and combined this with a constant interception efficiency (percentage of precipitation that is intercepted) multiplier which was first applied and tested by Andreadis et al. [2009]. Hedstrom and Pomeroy [1998] developed an interception model based on data from a boreal forest and were among the first to include canopy parameters (CC and LAI) and combined this approach with an interception efficiency function based on precipitation. This interception model has been widely used in the majority of the SNOWMIP2 models and is hereafter referred to as the 'standard model'. Despite the fact that this is a major step forward, the model did not integrate snow bridging or branch bending, which were formalized in past studies [Satterlund and Haupt, 1967; Schmidt and Gluns, 1991a] by a

sigmoidal function of interception efficiency (i.e., interception divided by precipitation). Instead, the model used an exponential decay function that reduces interception efficiency with increasing precipitation during a storm.

In order to (1) better represent the interplay between local canopy characteristics (LAI, CC) and the greater canopy structure and (2) provide an interception efficiency function valid in Norwegian spruce forests, Moeser et al. [2015b] developed a new interception model. It utilized canopy closure, total gap area, and mean distance to canopy (see section 2.3) to characterize the canopy and the structure of the surrounding forest. It also integrated a sigmoidal interception efficiency function to represent snow bridging that reflects an initial exponential increase (representing snow bridging) of the efficiency to a maximum, and a subsequent efficiency decrease (representing branch bending). Here, this new interception model is integrated in a snowmelt model. Since the interception model was initially formulated as a function of total interception during a storm event, it necessitated adaptations to function appropriately within a dynamic, discrete-time model.

The principal goal of this study was to (A) implement the new interception model in an existing snowmelt model, the Factorial Snow Model (FSM; Essery et al., 2015), at hourly time steps under a range of canopy and forest structure conditions. The subsequent analysis will show, (A-1) how the inclusion of forest scale canopy metrics (total gap area, mean distance to canopy) better accounts for the heterogeneous nature of under-canopy snow, (A-2) how the use of a sigmoidal interception efficiency distribution affects the interception and under-canopy snow estimations, and (A-3) how this new model deviates from a model that features a standard parameterization of interception when used in different precipitation regimes.

5.2 Methods

5.2.1 Overview of the FSM model

The Factorial Snow Model (FSM) is a simplified multi-model approach currently under development and evolved from the JIM (Jules Investigation Model) modeling framework [Essery et al., 2013]. The JIM framework is an energy balance-based snowmelt model that allows for three different parameterizations

of seven snow processes, yielding 1701 potential model configurations [Essery et al., 2013]. From this and other projects no specific configuration was found to yield optimal snow mass simulations, however a group of configurations provided consistently better performances than others [Magnusson et al., 2015]. Thus, these groupings were used to guide the configurations of FSM for the present study. The FSM includes two potential parameterizations for five snow properties and processes: albedo, heat conduction, snow density, turbulent fluxes and liquid water content (see Essery et al. 2015 for details). None of the parameterizations for these snow processes are new, and similar guiding equations can be found in several models, including CLASS [Clark et al., 2015a,b,c; Verseghy, 1990], CLM [Oleson et al., 2010], HTESSEL [Dutra et al., 2010], ISBA [Boone, 2009; Douville et al., 1995], JULES [Best et al., 2011], MOSES [Cox et al., 1999], and UEB [Mahat and Tarboton, 2014; Tarboton and Luce, 1996]. The primary function of the FSM model is not necessarily for forecasting but rather for providing a framework to evaluate how new parameterizations function within a comprehensive snow model. For this study, we implemented a canopy module in FSM with two possible parameterizations for canopy snow interception and affiliated processes (unloading and sublimation), where one parameterization used the standard Hedstrom and Pomeroy [1998] interception model and the second parameterization used the Moeser et al. [2015b] interception model (see Section 2.5 for details). Both interception parameterizations used the same unloading and sublimation modules in order to directly test the sensitivity of the new interception model against the standard model. The addition of these two interception parameters (to the existing parameterizations for each of the 5 snow properties and processes, as outlined above) led to an increase from 32 to 64 model configurations.

Hourly meteorological driving data of incoming shortwave radiation - ISWR (W m-2), incoming longwave radiation - ILWR (W m-2), snowfall rate - Sf (kg m-2s-1), rainfall rate - Rf (kg m-2s-1), air temperature - Ta (K), relative humidity - RH (%),wind speed - V (m s-1), and surface air pressure - Ps (Pa) were needed in order to run the model. In order to utilize the interception configurations, CC, LAI, mean distance to canopy (m), and total gap area (m2) were also needed at each point where the model was run.
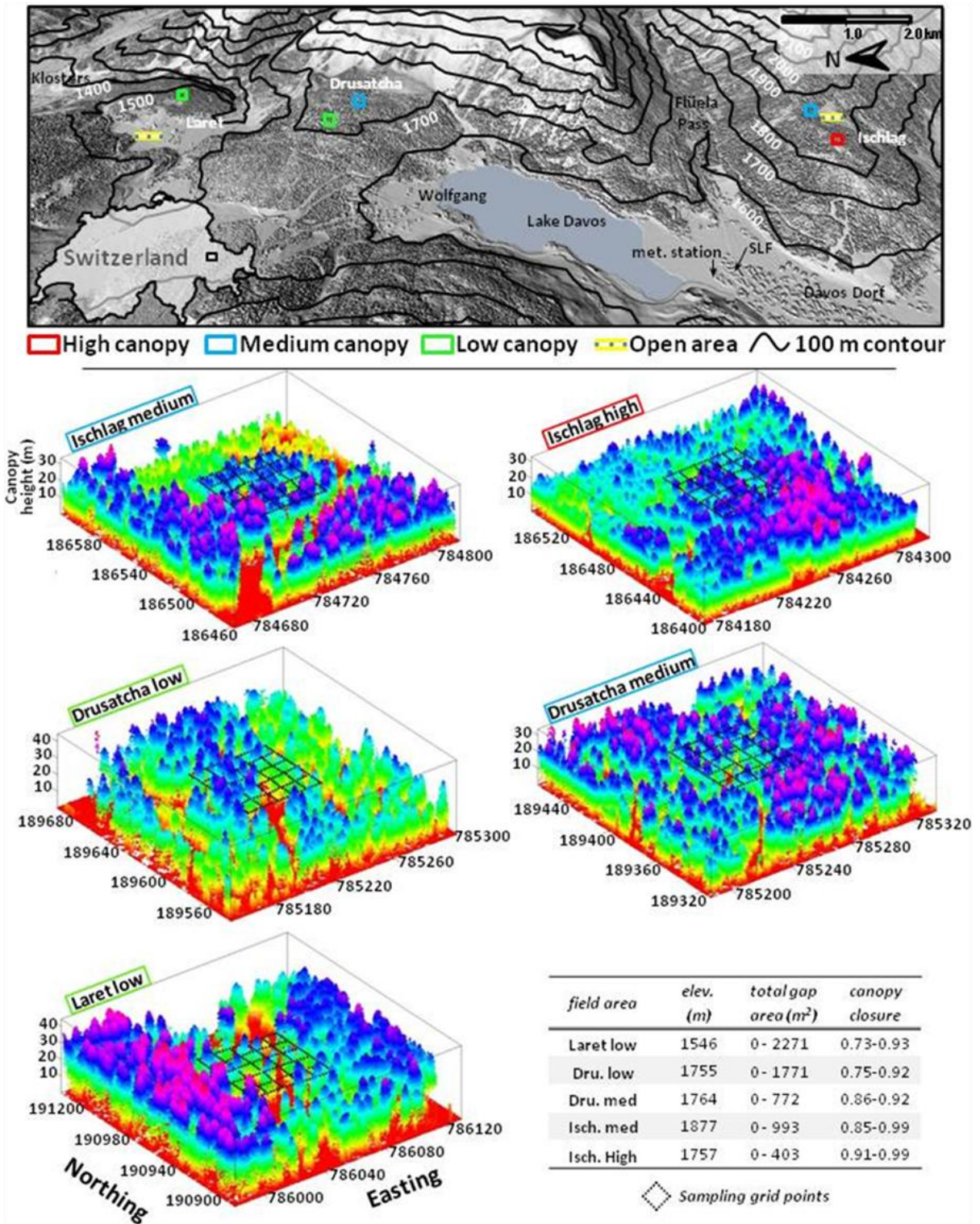
Figure 1. Five forested field areas and two open areas are located at three elevation bands surrounding Davos. The box plots are LiDAR data cloud representations of the forested field areas. Each field area contains a measurement grid (50m x 50m) with 276 surveyed and marked points. Each field area has unique forest gap fractions and highly heterogeneous canopy characteristics, as displayed in the lower right corner.

5.2.2   Field areas

Snow data from five field areas and two open areas at three elevation bands were utilized for this study (Figure 1). These areas were part of a long-term forest snow research initiative set up in Fall 2012 by the WSL Institute for Snow and Avalanche Research (SLF). Each of the five areas had a size of 2500 m2 and were chosen for study due their heterogeneous canopy cover which included larger scale forest properties such as forest openings. The stands are dominated by Norway spruce (Picea abies) and range in height from 0.5 to 45 m. The field areas have minimal terrain shading influence and low to no surface slopes. In each field area, a sampling grid was set up containing 276 points that were labeled and surveyed. Two open areas were also used (also part of the SLF forest snow research project) for comparison with the under-canopy measurements (see Figure 1 for a map outlining the location of the field areas as well as aerial LiDAR representations of the field areas). For more detailed information regarding the field sites, cf. Moeser et al. [2014].

5.2.3   Snow measurements

Snow depth (SD) and snow water equivalent (SWE) measurements were taken during the 2012/13 and 2013/14 winter seasons after all storm events (which had greater than 15 cm of SD in the open). SD measurements were taken at all sample grid points both in and outside the forest (1480 points in total). Total SWE was taken at twelve points per forested field area, and at two points per open field area.

Prior studies have utilized a variety of methods to quantify canopy interception, including weighing tree experiments [Hedstrom and Pomeroy, 1998; Nakai et al., 1994, 1999; Pomeroy et al., 1998; Satterlund and Haupt, 1967; Schmidt and Gluns, 1991; Storck et al., 2002; Suzuki and Nakai, 2008], Gamma Ray attenuation [Calder, 1991], time lapse photography [Bründl et al., 1999; Kobayashi, 1987; Nakai et al., 1999; Tennyson et al., 1974] and weighing lysimeters [Andreadis et al., 2009; Storck et al., 2002]. However, because of the large logistics effort required for these methods, no point-based data have been collected over large scales to date (see Friesen et al. 2014 for a detailed overview of measurement techniques). Thus, a method to indirectly measure interception was utilized. Snow interception was measured when specific ground and meteorological pre-conditions were prevailing: (1) solid crust on snow prior to storm, (2) no interception on trees prior to storm, and (3) low to no wind

redistribution during storm events. Nine storms in the two winter seasons met these conditions. In these cases, SD of the new snow on top of the crust was measured. Interception was determined as the difference between the depth of the newly fallen snow in the open areas and the SD in the forest at each grid point. Finally, all field points that were in positions that could have hindered the quality of the measurement were removed from the data set. This included points on top of stumps, on logs, in depressions or in areas where trees fell during the sampling campaign. This reduced the number of measurement points from 1480 to 1276.

The interception data were converted to water equivalent (SWE) using the fresh snow density model derived from the US Army Corps of Engineers [1956] by Hedstrom and Pomeroy[1998].

$$\text{snow density} = 67.92 + 51.25 \, e^{(T/2.59)} \qquad\qquad \text{eq. (1)}$$

Average air temperature (T) during each storm at each field site was derived from temperature lapse rates (individually derived for each storm event). These were based on an altitudinal gradient from four IMIS (Intercantonal measurement and information system) meteorological stations surrounding Davos, Switzerland, at 4 elevations bands: IMIS-KLO (Klosters) – 1560 m, IMIS-SLF (Davos) – 2140 m, IMIS-PAR (Parsenn) – 2290 m, IMIS-WFJ (Weissfluhjoch) – 2540 m. They yield an average RMSE of 0.38 °C.

5.2.4   Canopy and forest metrics

Aerial LiDAR data were used to derive all canopy metrics: CC, LAI, total gap area (m2), and mean distance to canopy (m). LiDAR acquisition was carried out in September 2010 from a helicopter flyover using the Riegl LMS Q 560 sensor. The average echo density was 36 /m2 with a shot density of 19 /m2 (density of last returns).

Canopy closure was derived using the method from Moeser et al. [2014] where the LiDAR data were used to create hemispheric-like images (synthetic images) at all surveyed points. The synthetic images were processed using the software 'Hemisfer' [Schleppi et al., 2007; Thimonier et al., 2010], and LAI and CC were derived for each point. The LiDAR-based estimates of CC and LAI resulted in a

correlation of 0.93 for CC and 0.83 for LAI when compared to estimates based on true hemispherical photography at 112 locations within the field areas [Moeser et al., 2014].

Total gap area (TGA) and mean distance to canopy (MDC) were derived using a vector searching algorithm developed by Moeser et al. [2015a]. It analyzes the dimensions of open areas as seen from a specific point in 192 unique directions (in a 2D projection) and calculates the open area based on this directional analysis (TGA). MDC was defined as the average distance of each of the 192 search directions (distance from the point to a canopy element). This process was run for each of the 1276 forest field points.

5.2.5   Meteorological input data

All meteorological input data were collected from the SwissMetNet (automatic meteorological stations run by MeteoSwiss) station DAV2 (http://www.meteoschweiz.admin.ch/home.html?tab=overview). It is located <5 km from all field sites at 1594 m.a.s.l. (labeled as 'met. station' in Figure 1). For ISWR, ILWR, Rh, V, and Ps the measured values were used for all field areas, whereas Ta, Rf and Sf were adjusted to better match the specific meteorological conditions of each field area, as explained below. All data were used at hourly time steps.

Temperature was interpolated to each field area by applying the commonly used atmospheric lapse rate (Lr) of -6.5 °K per 1000 m of elevation gain:

$$T_{corr} = T_{metstation} + L_r(Alt._{fieldstation} - Alt._{metstation})$$
<div align="right">eq. (2)</div>

where Tcorr is the corrected temperature (at all time steps) for each site, which depends on the elevation difference (in meters) between the field stations (Alt.fieldstation) and the meteorological station (Alt.metstation).

The DAV2 station used a heated gauge to measure precipitation. Therefore a partitioning scheme was needed to separate solid (fsolid) from liquid precipitation (fliquid). There is a considerable amount of work on solid vs. liquid partitioning (Kienzle, 2008; Marks et al., 2013; Rohrer, 1989; Ye et al., 2013). However, a modification of the S-shaped function proposed by Kateveski and Kuczera [2007] was

implemented because it was locally calibrated. The threshold temperature, Tp (1.2 °C), which denotes

the temperature at which precipitation is 50% solid, and a further parameter, Mp (0.4), which controls

the width of the function, were calibrated at the nearby Weissfluhjoch meteorological station from prior

work by Wever et al. [2014]:

$$f_{liquid} = \frac{e^{\frac{T_a - T_P}{m_P}}}{1 + e^{\frac{T_a - T_P}{m_P}}}$$

eq. (3)

$$f_{solid} = 1 - f_{liquid}$$

eq. (4)

where fliquid and fsolid are the relative fractions of liquid and solid precipitation, respectively.

The undercatch of solid precipitation from the heated gauge was corrected by a direct comparison of

manual SWE measurements made at the station during the accumulation season from the past 35

years to the cumulative precipitation values from the gauge [as in Egli et al., 2009]. The data series was

parsed to exclude time periods with temperatures over 0 °C. This gave a series of cold periods during

accumulation. The difference between the first manual SWE measurement (SWEt0) and last SWE

measurement (SWEtend) during each of the cold periods were calculated and divided by the total

cumulated precipitation (P) from the gauge:

$$undercatch = \frac{(SWE_{t_{end}} - SWE_{t_0})}{\Sigma_{t_0}^{t_{end}} P_t}$$

eq. (5)

All undercatch estimates were averaged, and this value (30% undercatch) was used as a multiplier to

the precipitation data from the gauge.

A strong precipitation gradient is present across the Davos region. In general, the sites at Laret and

Drusatscha receive more precipitation than the Ischlag sites and the meteorological station (Figure 1).

Due to this, a comparison was made between measured SWE at the Laret open area and at the

meteorological station. The same was done for the Ischlag open area. The equivalent methodology as

the above undercatch analysis was utilized to account for the horizontal precipitation gradient per site

and on a yearly basis.

5.2.6   New interception model

5.2.6.1   Description and changes

Moeser et al. [2015b] defined Imax (mm SWE), i.e. the maximum amount of interception on a canopy

element, as a function of the log10 of mean distance to canopy (x1), log of canopy closure (x2), and log

of total gap area (x3):

$$I_{max} = 2.167(x1) - 3.410\ (x1)^2 + 55.761(x2) + 181.858(x2)^2 - 2.493(x3) + 0.499(x3)^2 + 20.819 \qquad \text{eq. (6)}$$

The Imax function was combined with a sigmoidal distribution of interception where I or interception

(mm SWE) was defined as:

$$I = \frac{I_{max}}{1 + e^{-k(P - P_o)}} \qquad\qquad \text{eq. (7)}$$

where P is total storm precipitation, and the constants k and Po are 0.3 and 13.3, respectively.

However, this equation could not be directly implemented for time series data because storm

precipitation cannot be used in a model framework that utilizes discrete model time steps. Therefore

this equation was changed to represent dI/dt (i.e., the rate of change of snow held in the forest canopy)

per equivalent time step unit.

However, two hurdles were encountered when converting eq. 7 into a differential form. To ensure

consistency with the law of mass conservation, dI/dt cannot exceed dP/dt, or equivalently dI/dP must be

≤1. However, while a rare occurrence, eq. 7 can result in interception rates that exceed precipitation

rates for certain values of Imax (Figure 2).
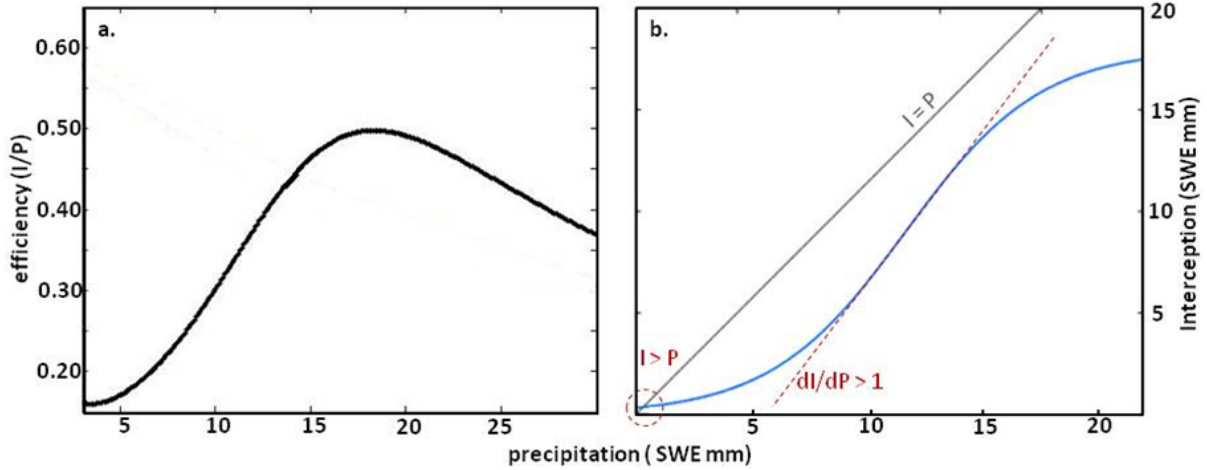
Figure 2. Left (a.): Original efficiency curve as published in Moeser et al. (2015b). Snow bridging is represented by the efficiency increase to a maximum, at which point branch bending outcompetes bridging, thus leading to a decline in efficiency. Right(b.): Interception curve (blue) The red circle shows that where precipitation values are small, this model version led to interception greater than precipitation. The red line shows where (dependent upon I_{max}), the derivative of the interception function can exceed unity.

If P is explicitly solved, then

$$P = -\frac{1}{k}\ln\left(\frac{I_{max}}{I} - 1\right) + P_0 \qquad \text{eq. (8)}$$

$$\frac{dI}{dP} = -\frac{kI}{I_{max}} \quad I_{max} - I \qquad \text{eq. (9)}$$

Eq. 9 must fulfill the condition of dI/dP ≤1 in order to ensure no errors are introduced in the mass balance. Solving for I when the derivative of dI/dP is set to 0 and reinserting this term into equation 9 leads to the following constraint:

$$\frac{kI_{max}}{4} \leq 1 \qquad \text{eq. (10)}$$

When the initially proposed k of 0.3 and Po of 13.3 were used, eq.10 was not fulfilled with Imax > 13.3 mm of SWE. Therefore k and Po were re-optimized, but now with the constraint of eq. 10. The optimization process followed the exact methodology used for the initial model development [Moeser et al., 2015b], which was based upon the minimization of the RMSE of the actual vs. model values (from eq. 7). This led to updated values of k = 0.215 and Po = 12.483 (Figure 3).

The second hurdle was encountered when considering extremely low precipitation events, which were not present in the data used to develop the interception model, led to overestimations (albeit very small) of interception efficiency because I > 0 for P close to zero (equation 7, red circle in Figure 2b). This is a structural problem that cannot be circumvented when using this sigmoidal function. To account for this, the interception function was forced to pass through the origin by defining an interception threshold:

$$I_{thresh} = \frac{I_{max}}{1+e^{-k(5-Po)}}$$ eq. (11)

$$dI/dP = I_{thres} / 5 \text{ mm, if } I < I\_thres$$ eq. (12)
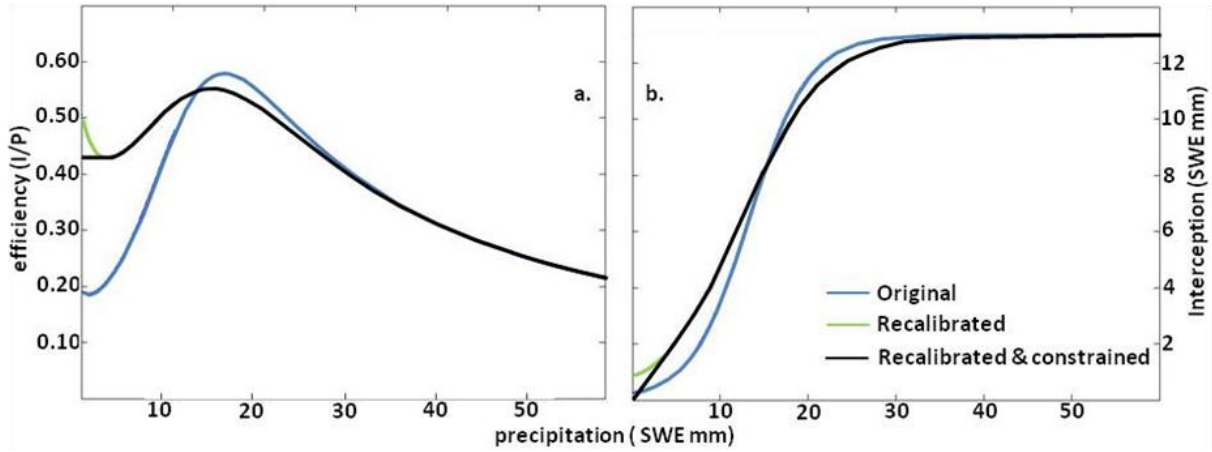

Figure 3. <u>Left (a):</u> Interception efficiency for Imax = 13.0 mm SWE. <u>Right (b):</u> Interception for Imax = 13.0 mm SWE. The blue lines represent the original Moeser et al. model (eq. 7 with k = 0.3 and Po = 13.3). The green lines show the recalibrated model (k=0.215 and Po = 12.483). The black lines show the recalibrated and constrained model (from eq.11 and eq.12).

5.2.6.2   Model implementation

To incorporate equations (7), (11) and (12) into FSM, a new variable, Ptotal was introduced that cumulates precipitation and allowed for conversion between storm steps and uniform time steps. Thus, interception is calculated using the following set of equations.

$$I(t) = \frac{I_{max}}{1+e^{-0.215[P_{total}(t)-12.483]}}$$ eq. (13)

$$I^*(t) = I(t) - \text{sublimation}(t) - \text{unloading}(t)$$ eq. (14)

where I*(t) is interception at time t with sublimation and unloading removed, and

$$P_{\text{total}}(t) = P^*(t-1) + P(t) \qquad \text{eq. (15)}$$

when $I^*(t) \leq I_{\text{thresh}}$:

$$P^*(t) = \frac{I_{\text{thresh}}}{5} P(t) \qquad \text{eq. (16)}$$

when $I^*(t) > I_{\text{thresh}}$:

$$P^*(t) = \frac{1}{-0.215} \ln\left[\frac{I_{\text{max}}}{I^*(t)} - 1\right] + 12.483 \qquad \text{eq. (17)}$$

5.2.7 Standard interception model

The standard interception model from Hedstrom and Pomeroy [1998] defined Imax as a function of LAI:

$$I_{max} = 5.9 \left(0.27 + \frac{46}{\rho_{snow}}\right) LAI \qquad \text{eq. (18)}$$

Where ρsnow (kg m-3) is the density of falling snow and the multiplier of 5.9 is specific for spruce trees. Imax was combined with an exponential decay function of interception:

$$I = I_{max}\left(1 - e^{-\frac{CC}{I_{max}}P}\right) \qquad \text{eq. (19)}$$

where P is precipitation. The model was implemented into the FSM following the method of Hedtsrom and Pomeroy [1998] and Pomeroy et al. [1998].

5.2.8 Canopy snow removal: unloading and sublimation

5.2.8.1 Unloading

Unloading is a complex process which is dependent upon precipitation characteristics (timing, duration, amount and density), wind (speed and direction), temperature, canopy characteristics, and branch flexibility. Due to these complexities, unloading represents a major research gap in forest snow hydrology to date [Hedstrom, 1998; Liston and Elder, 2006; Roesch, 2006]. Since the primary goal of this work was to analyze the sensitivity of a new interception algorithm by gauging its performance against a standard model, the standard unloading model could not be used, as it unloads different

amounts of intercepted snow on a canopy element in approximately the same amount of time. This eliminates any potential differences in snow on the ground from differing interception models. Due to this, we implemented (in both parameterizations of interception) a variant of the model introduced by Liston and Elder [2006] that was used in 'SnowModel' [Liston and Elder, 2006]' and 'AMUNDSEN' [Strasser et al., 2008b; Strasser et al., 2004]:

$$\text{unloading} = 5.8 * 10^{-5}(T_a - 273.16) \qquad \text{eq. (20)}$$

where unloading (mm/second) is a direct function of air temperature (T_a in °K), gives an unloading rate of 5 mm/day per °K above 0 °C and is only applied when temperature is above 0 °C. We modified the stepwise function proposed by Liston and Elder [2006] to a continuous unloading function to allow for limited snow unloading snow even below 0 °C (starting from -5°):

$$\text{unloading} = 3.022 * e^{\frac{-(Ta - 258.15)^2}{63.28}} \qquad \text{eq. (21)}$$

Like the original Liston et al. model, eq. 21 does not capture many of the complexities found in the unloading process. However, unlike pure temporal decay functions such as the standard unloading model, it accounts for temperature effects on unloading and can be used for discrete time steps at all temperatures (Figure 4).
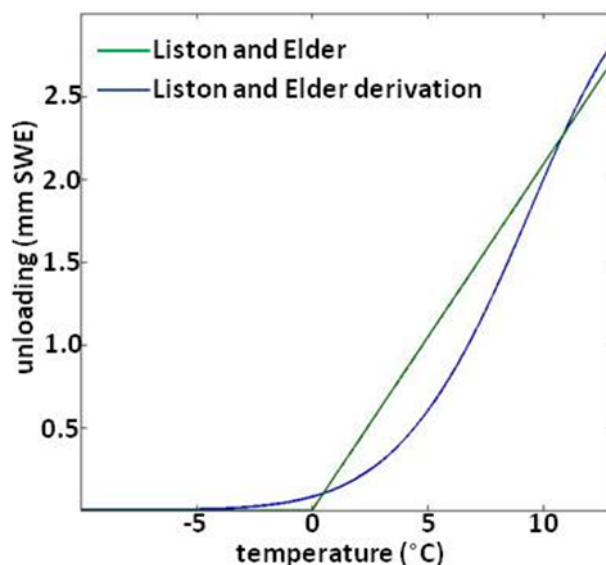
Figure 4. Comparison of the stepwise Liston and Elder (2006) model (green) and a continuous function (in blue).

Note that the new interception model implemented in FSM was developed based on data collected after storms that inherently included snow that was unloaded during snowfall. Due to this, the unloading function was not applied during snowfall events.

5.2.8.2   Sublimation

Sublimation of snow in the forest canopy is traditionally modeled by calculating the energy balance of snow on the forest canopy [Pomeroy et al., 1998]. However, in its current form, FSM does not have the capability to model the energy balance of snow on the canopy. Instead, a new sublimation model based on values typical for this area (calculated at a neighboring field site [Seehorn: 46.815, 9.856] from eddy covariance estimates) was developed. Minimum, mean and maximum sublimation values were evaluated, and a power function was fitted to incoming solar radiation data

$$potential\ sublimation = 3.54 * 10^{-4} ISWR^{1.070} \qquad\qquad \text{eq. (22)}$$

This power function reflects min/mean/max sublimation values, from the input of   min/mean/max measured ISWR values from the meteorological station. Potential sublimation in mm/ hour is the potential amount of sublimation that can occur during a time step ⫶t (Figure 5). Actual sublimation is dependent on the amount of snow remaining in the canopy (if any); if the amount of remaining canopy

snow is less than or equal to the potential sublimation rate then all remaining snow is sublimated. This model (eq. 22) gave an average value of 0.35 mm / day and a maximum of 3.48 mm/day of potential sublimation (from this data set). While this is a simplified approach, it produced reasonable values of sublimation that were comparable with prior studies (Table 1).

Table 1. Review of average and maximum sublimation rates as well as the fraction of annual snowfall sublimated from prior studies. *Assuming 5 months of Sf precipitation.

| mean rate	maximum rate	% sublimated	location	method	study
0.2 / hour	0.5 / hour	-	Scotland	mass balance	Calder et al. [1991]
0.51 / day	1.5 / day	-	Colorado	weighing tree	Schmidt et al. [1991b]
-	0.3 / hour / 3.3/ day	-	Sweden	weighing tree	Lunberg et al. [1994]
-	4.0 / 36 hour	-	Saskatchewan	-	Harding et al. [1996]
0.24 / hour	0.56 / hour / 3.9 / 7 hour	-	Scotland	Gamma ray attenuation	Lundberg et al. [1998]
-	3 / day	38-45%	Saskatchewan	weighing tree	Pomeroy & Pavanien [1998]
0.6 / day	2.3 / day		Japan	eddy covariance	Nakai et al. [1999]
-	2.5 / day	20-30%	global	model	Essery & Pomeroy [2003]
1.0 / day	4.3 / 7 hours	14%	SW Oregon	weighing tree	Storck & Lettenmaier [2002]
0.70 / day	3.7 / day	-	Colorado	eddy covariance	Molotch et al.[2007]
1.31-1.64 / day*	-	≤50%	Austrian Alps	model	Strasser et al. [2008a]
0.55 / day	1.6 / day	50%	N. America / Europe	model	Ellis et al. [2010]
-	-	32%	Colorado	mass balance	Wilm & Dunford [1945]
-	-	24%	East. Oregon	mass balance	Miner & Trappe [1974]
-	-	40%	-	-	Meiman et al. [1974]
-	-	32-36%	Sasketchewan	mass balance	Pomeroy & Gray [1995]
-	-	32-45%	Sasketchewan	mass balance	Pomeroy et al. [1998]
-	-	39-45%	Yukon	mass balance	Pomeroy et al. [1999]
-	-	20-30%	-	-	Montesis et al. [2004]
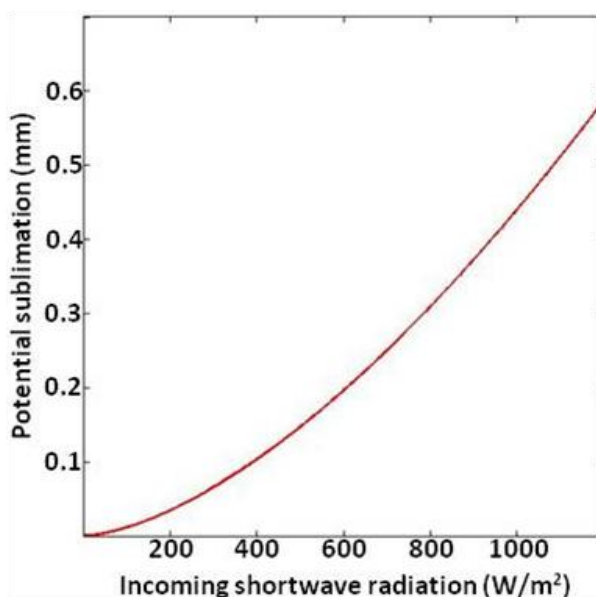
Figure 5: Potential sublimation as a function of ISWR.

5.2.9   FSM model application

The FSM model was run at 1276 points for the 2012 and 2013 field seasons. The FSM configurations for each of the interception models (standard model and Moeser et al.) were grouped at each time step and the median value at each step was taken. This gave median values (as well as a range) for each output parameter from the FSM (SD, SWE, etc) for each interception parameterization at each time step. The median values from each interception model were compared. Specifically, the sensitivity between the interception parameterizations was analyzed for the effect on (1) interception estimation, and (2) under-canopy SWE and under-canopy SD. These differences were primarily assessed using a comparison to the distribution of the forest canopy, in order to better estimate how well the forested environment has been represented and whether the heterogeneity of the forested environment has been captured down the modeling chain.

5.3 Results and Discussion

The initial interception model was successfully integrated into the FSM model at hourly time steps from the integration of equations 11 – 17. This new system of equations demonstrated a similar fit to interception events as the original storm-based model.

The Moeser et al. [2015b] model reproduced storm interception events with an R2 of 0.65 and RMSE of 3.39 mm. When k and Po were re-optimized using the constraint from eq. 10, no change was seen in R2, and the RMSE remained virtually the same (3.40). The standard model [Hedstrom and Pomeroy, 1998] had an R2 of 0.39 and RMSE of 5.19 mm. Below we have analyzed how these model differences transferred into contrasts in under-canopy snow and demonstrated how these contrasts relate to forest canopy characteristics.

The field points show a large spatial variation of canopy parameters, with total gap area ranging from 0 to 2250 m2, mean distance to canopy ranging from 0 to 23.7 m and LAI ranging from 1.2 to 8.0. Logically, these large variations should be seen in the results, with low interception at points with a high openness (high TGA and MDC) and high interception in areas with low openness (low TGA and MDC), with the closed canopy areas having even higher interception with progressively higher LAI or CC values. Furthermore, the trends in interception estimations as they relate to the canopy should also be seen in the under-canopy SWE and SD estimates.
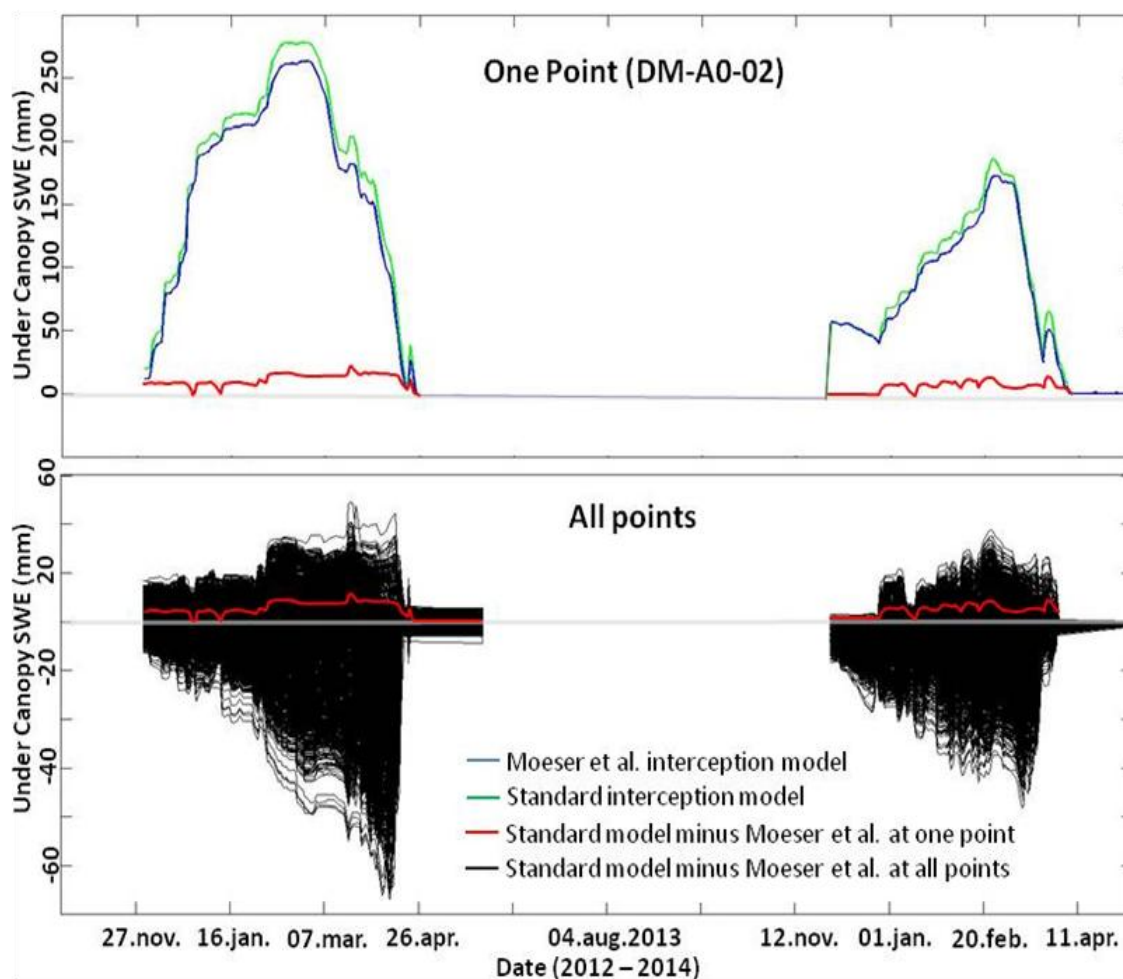
Figure 6. <u>Top:</u> Comparison of under-canopy SWE at point A0-02 in the Drusatcha Medium (DM) field area when using the standard interception model (green) vs. the Moeser et al. interception model (blue) and their difference (red). While some field points feature similar under-canopy SWE estimates, such as this point, many points show substantial differences between the two interception modules.

<u>Bottom:</u> Difference of under-canopy SWE from the two interception models at all points (black), with the red difference line from point A0-02 (top) being displayed again in the lower panel.

5.3.1   Interception and under-canopy snow

Despite the fact that some simulated points showed similar under-canopy SWE estimations between the two interception modules (Figure 6, top), the majority of the points featured large deviations (Figure 6, bottom). The under-canopy SWE estimates using the Moeser et al. model were generally improved, due to the inclusion of new metrics of forest structure (i.e., TGA, MDC). Specifically, the largest differences between the two models were found at the canopy–open area interface and at open areas which were described by TGA and MDC.

To demonstrate this, two points with similar canopy closure (0.90 vs. 0.92) but different TGA (68.81 m2 vs. 541.62 m2) and MDC (2.01 m vs. 10.75 m) that are located approximately 8 m apart were analyzed (Figure 7, for locations of the points see Figure 8). The use of the standard interception model yielded almost equivalent cumulative interception and sublimation estimates (and therefore also SWE and snowmelt), while use of the Moeser et al. model simulated substantial differences.
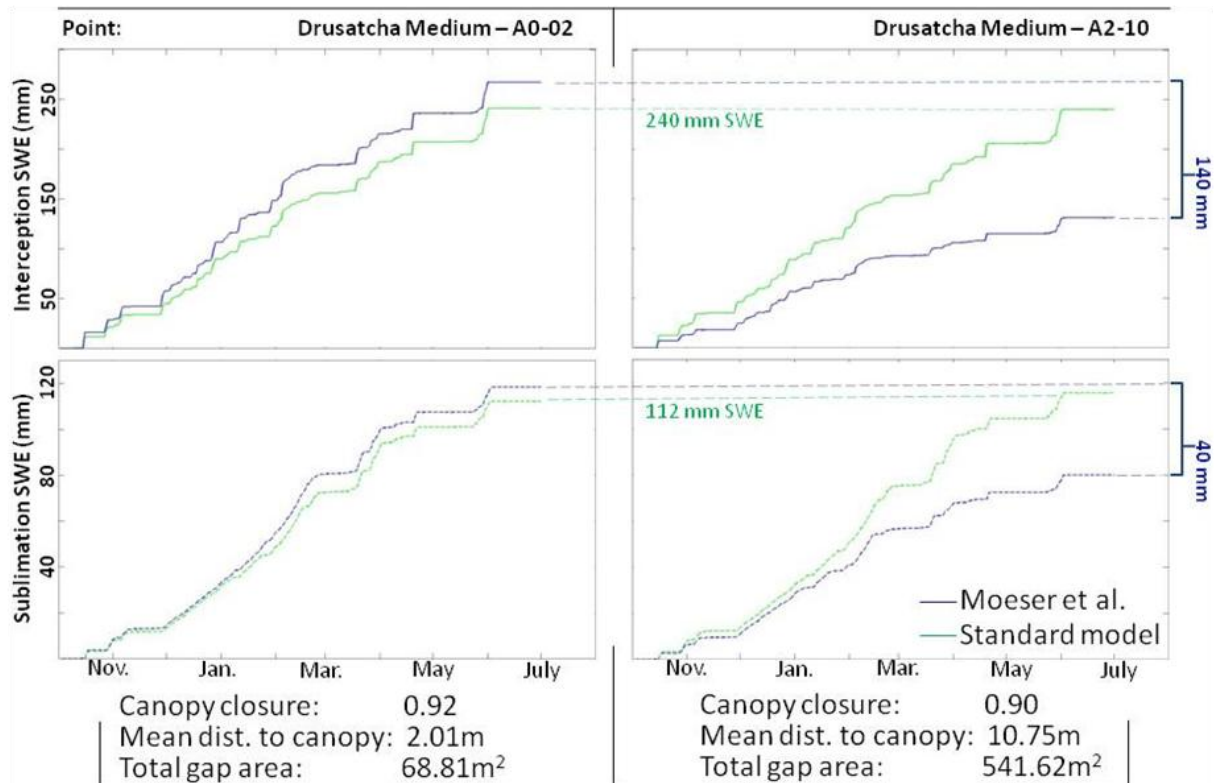

Figure 7. The point on the left (A0-02) and the point on the right (A2-10) have similar CC values (0.90-0.92) but display very different forest scale metrics. Top: cumulative interception for the 2012/13 winter season. Bottom: cumulative sublimation for the 2012/13 winter season. Locations of these points can be seen within figure 8.

TGA and MDC had further effects on the behavior of the two FSM groupings [i.e., the Moeser et al. interception grouping and the standard interception grouping) on larger scales. Figure 8 displays the cumulative interception for all points within the Drusatcha Medium field area along with the overlying canopy structure. The open areas and canopy-open area interfaces can be visualized (Figure 8, left), and when these features are compared to the simulation output, significant differences between the modeling approaches become evident. Furthermore it displays (as with the point-based analysis in

Figure 7) nearly equivalent cumulative interception estimates at all points within the field area when the standard interception model was applied (Figure 8, right). This is contrasted to the Moeser et al. model which displayed a significant cumulative interception estimation variance which closely mimicked the horizontal forest structure. At all points, the Moeser et al. cumulative interception estimates ranged from 25 to 310 mm SWE, whereas the estimates from the standard model ranged from 165 to 310 mm SWE.
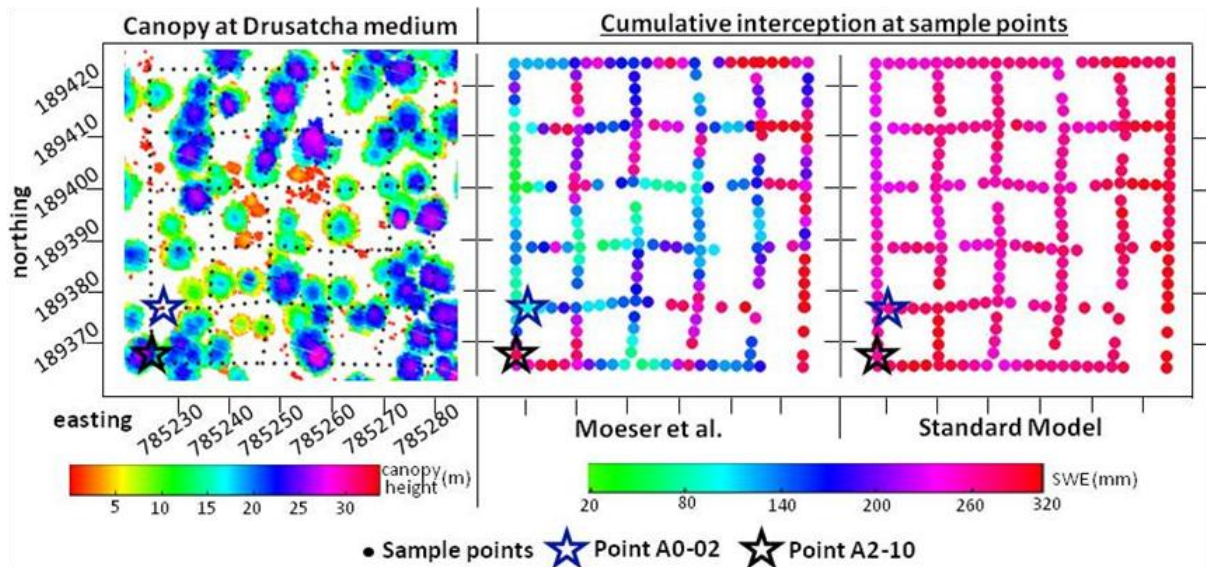
Figure 8. Left: Canopy height at the field area Drusatcha Medium. Center: Cumulative interception estimates from the Moeser et al. model. Right: Cumulative interception estimates from the standard model. The points from figures 6 & 7 are labeled as stars.

Similar patterns were evident from the simulated under-canopy SD for the peak of the winter 2012/13 (Figure 9): the Moeser et al. model displayed much greater variation in estimated values, ranging from 55 cm to 83 cm on the ground, compared with 53 cm to 67 cm from the standard model.
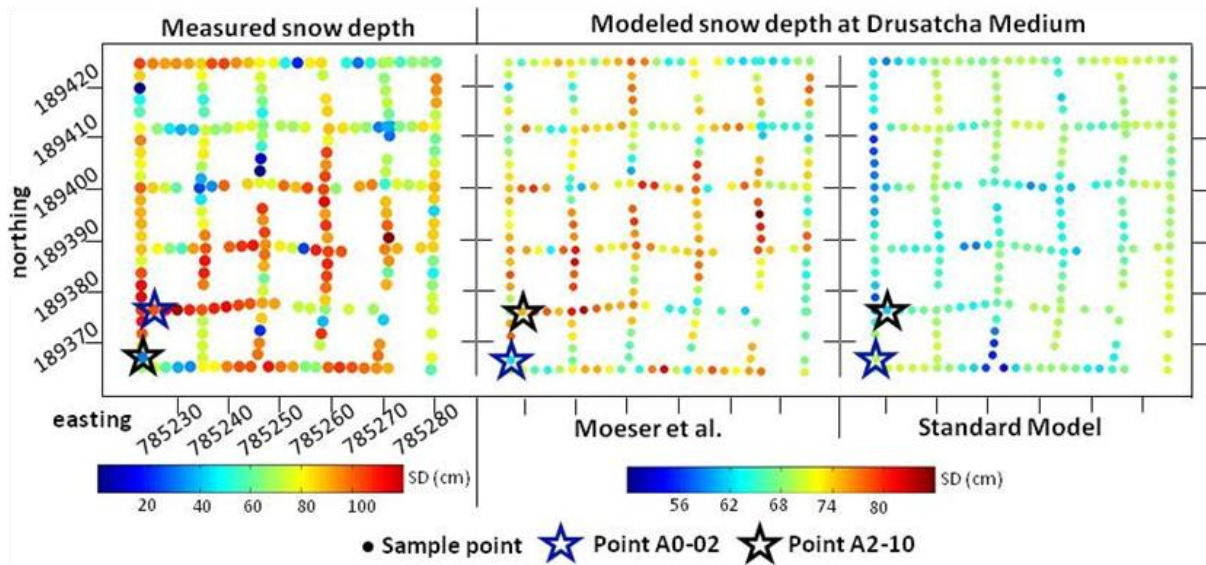
Figure 9. Left: Measured snow depth at the peak of winter 2012/13. Center: Simulated SD when using the Moeser et al. interception model. Right: Simulated SD when using the standard interception model. Similar to the interception estimates (Figure 7), the standard model showed fairly homogenous estimates throughout the field area, while simulated SD from the Moeser et al. model features heterogeneous values and displayed a similar pattern as in the measured data.
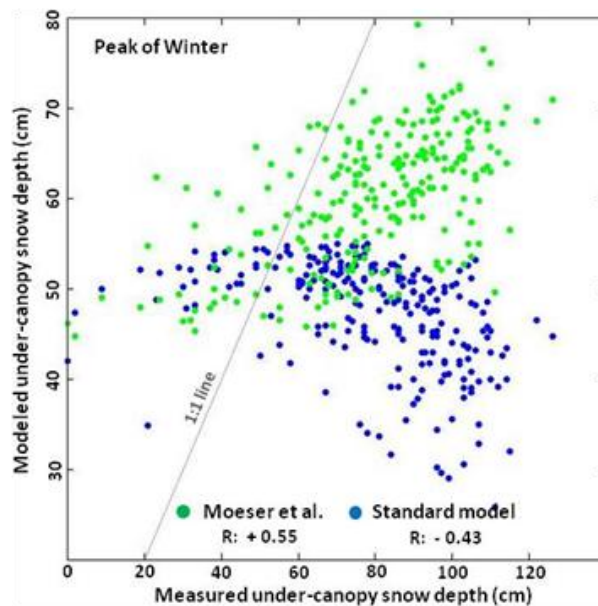
Figure 10. Comparison of simulated and measured under-canopy snow depth in the Drusatscha Medium field area. The negative correlation in the standard model is primarily due to interception overestimates in open areas. The RMSE of the Moeser et al. and the standard model are 22 and 29 cm of snow depth, respectively.

Although both models showed some degree of absolute biases (of ~20 cm SD which can be seen in the disparate scale bars in figure 9), the Moeser et al. model output was more consistent with ground observations compared to the standard model. Absolute SD estimates from the Moeser et al. model

were reasonably close to observations, and the spatial pattern was very similar. This was not the case for the standard model, where some of the low simulated values (blue colors) were associated with high observed values (red colors; cf. Figure 10). This inverse correlation present within the standard model can be visualized within a plot of observed vs. modeled snow depth in figure 10. See section 3.4 for further analysis.

5.3.2 Unloading and sublimation

The larger range in estimation variance from the Moeser et al. interception model was also evident in simulated unloading and sublimation estimates. Sublimation ranged from a maximum of 0.79 to 3.48 mm/day SWE (depending on Imax), with a mean of 0.05 to 0.47 mm/day SWE, which amounted to 2.6 to 31% of total winter precipitation (or 3 to 42% of total winter snowfall). This was more than double the variance compared to the standard interception model (Figures 11, 12). Although these numbers would vary if other unloading and sublimation models were used, the magnitude of the estimation variance between the two interception models would remain similar since they are a function of the amount of intercepted snow on the canopy. Furthermore, these results were comparable to those of prior studies (Table 1).
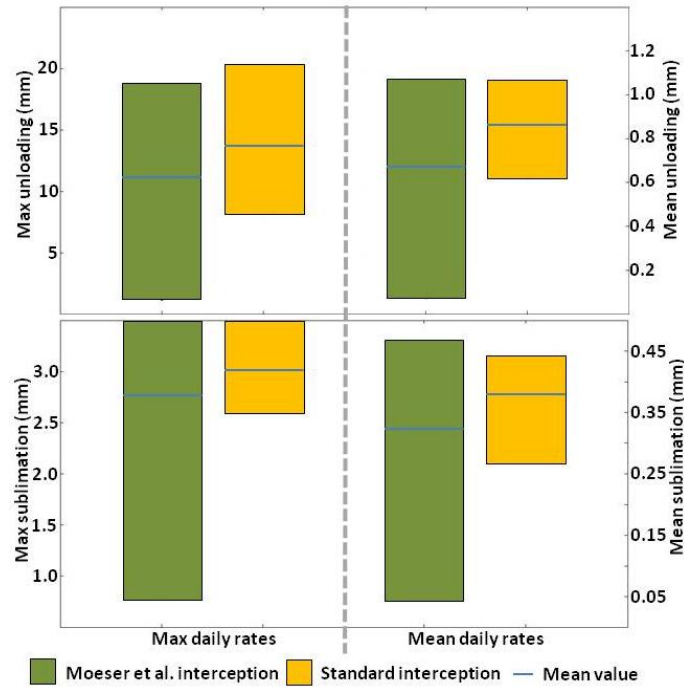
Figure 11. <u>Left:</u> Maximum simulated daily unloading and sublimation rates according to both models. <u>Right:</u> Simulated mean daily rates at all points. The range of values represents the variability between sample points.
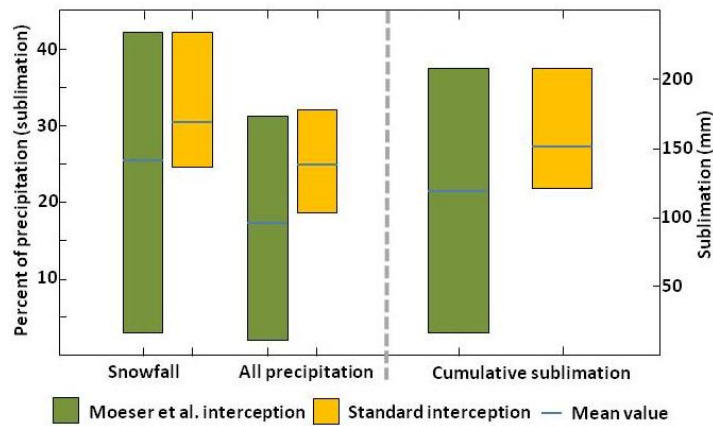
Figure 12. <u>Left:</u> Percent of total precipitation that was sublimated according to both models. <u>Right:</u> Cumulative sublimation values for the 2012/13 season at all points.

5.3.3   Precipitation event size

The differences in the output of the two interception models were not only related to canopy structure variables. Structural differences between the models also resulted in varying responses to the size of precipitation events. Frequent small storms, which characterize the study areas, led to higher

estimations of interception from the standard model compared to the estimations from the Moeser et al. model, whereas large storms, which are atypical of the area, led to lower estimations from the standard model. This was also evident from the storm event analysis [Moeser et al., 2015b, Figure 6] where interception was underestimated by the standard model for large storms and overestimated for small storms. This was due to the function describing interception efficiency (Figure 13), which in the standard model was modeled as an exponential decay. This allowed for large amounts of freshly fallen snow to be intercepted early in a storm event. In contrast, the Moeser et al. interception model started with a lower interception efficiency, which increased as the storm continued due to snow bridging and then decreased due to branch bending. While, for large precipitation events, both models may reach a maximum interception, the underlying efficiency has systematic consequences on the mass balance if a snow storm does not reach this point.
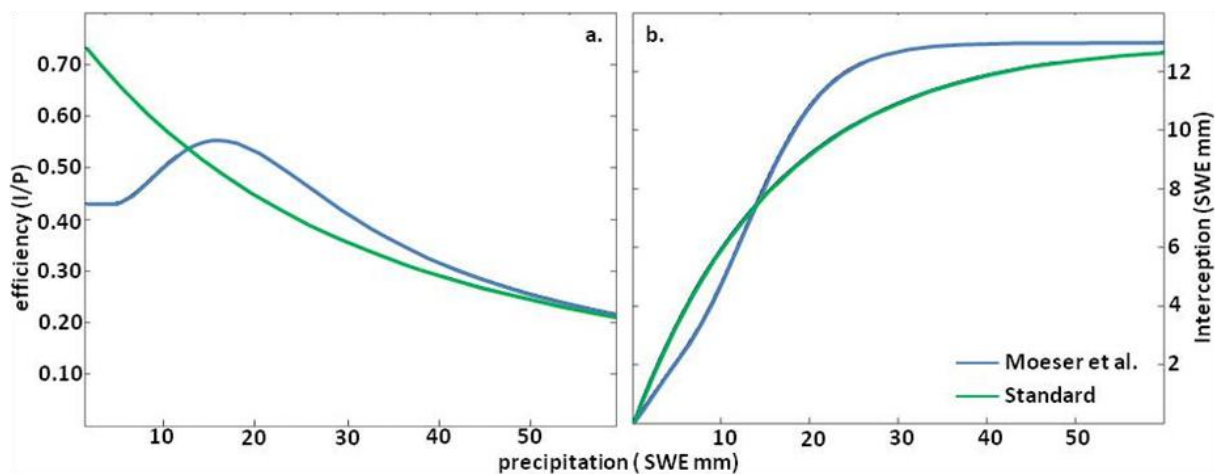
Figure 13. <u>Left (a.):</u> efficiency curves from the two interception models for Imax = 13.0 mm SWE. SWE. <u>Right (b.):</u> Interception curves Imax = 13.0 mm SWE.

The effect of the precipitation distribution was visualized from an analysis of Ptotal, which is a proxy for cumulative storm precipitation (Figure 14). When Ptotal was ≥ 5 mm, the Moeser et al. model showed significantly higher hourly interception values than the standard model. When Ptotal was < 5 mm, the standard model displayed higher hourly interception estimations in areas with moderate to high MDC and TGA values. Thus, if the standard model is to be utilized in forests that are characterized by snow

bridging and large storm events prevail, the interception would be underestimated and under-canopy snow over-estimated. The opposite applies to areas characterized by frequent small precipitation events (such as Davos).
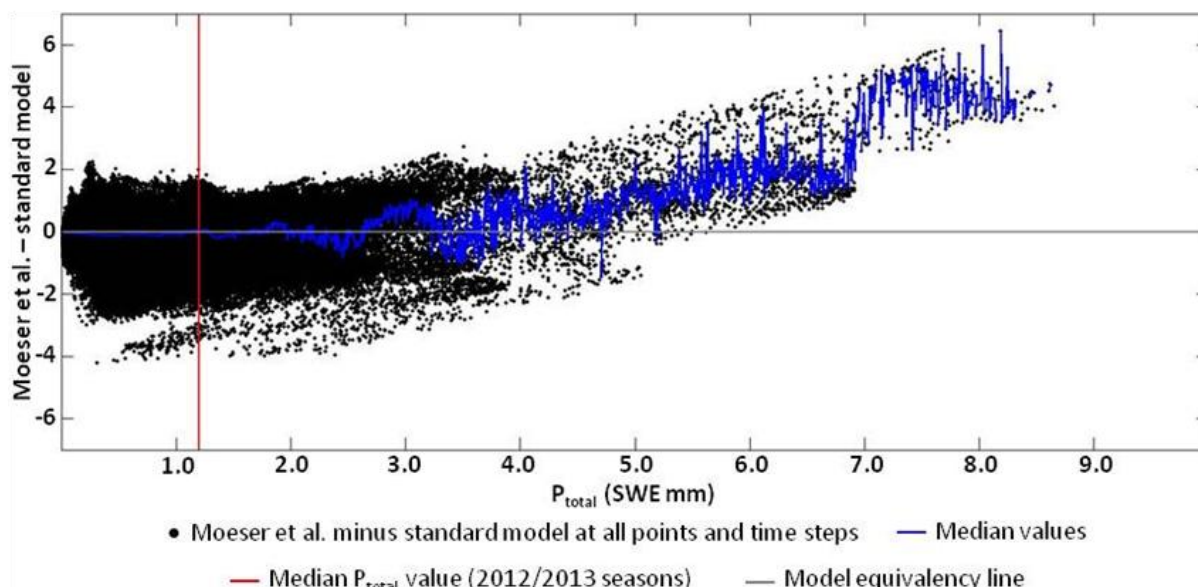
Figure 14. Analysis of the effect of precipitation distribution on simulated interception. Ptotal is a proxy for total storm precipitation and was calculated every hour for the 2012 and 2013 season. At large storm events, the Moeser et al. model gives higher estimates than the standard model, whereas for small storms, the standard model gives higher values when the simulated areas have medium to high TGA and MDC values.

5.3.4   Sensitivity analysis

The FSM model used basic parameterizations of various processes [Essery et al., 2015], including the unloading and sublimation routines proposed in this paper. These simplifications can be seen in the difference between the goodness-of-fit statistics between interception estimates and the under-canopy snow depth estimates (Table 2, Figure 15). The correlation coefficient of under-canopy SD (for both interception models) was approximately 20% lower compared to the correlation coefficient of interception estimates. Still, the sensitivity behind using two disparate interception models could be analyzed relative to the forest structure. As the size of forest gaps increased (openness), the standard model lost the ability to estimate interception and under-canopy snow. The new model, however, showed no major degradation in the correlation coefficient as forest stand openness increased for the

interception and under-canopy snow estimates (Figure 15). This was due to the inclusion of forest metrics that were able to resolve where a point was located relative to an open area (i.e., open areas have low to no interception). This was contrasted by the point-based metrics in the standard model that were unable to determine where an open area begins and ends (LAI, CC).
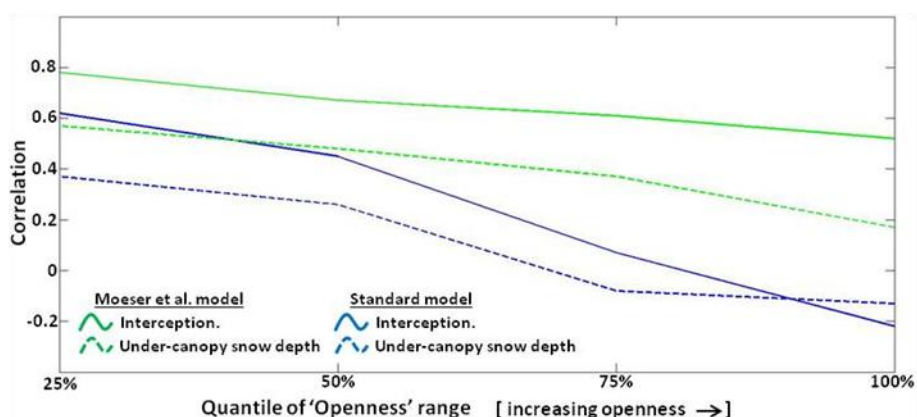

Figure 15. All points were grouped into quartiles based upon mean distance to canopy and total gap area to represent openness (x axis). The solid lines represent the correlation of interception estimates and the dotted lines represent under-canopy snow depth estimates. Note that the standard model (in blue) demonstrates reduced correlations as compared to the Moeser et al. and the initial correlations quickly diminish as openness of the field points increases (increase in TGA and MDC) which is not as apparent in the Moeser et al. model.

Table 2. Comparison of the use of the interception models for under-canopy snow depth at peak of winter (04.April.2013) and interception. All points were grouped into quartiles based upon mean distance to canopy and total gap area to represent openness. For a visual analysis see Figure 15.

'openness' Quantile	Interception (mm- SWE)				Peak of Winter Snow Depth (cm)				total gap area (m²)	mean dist. to canopy (m)	canopy closure
	r		RMSE		r		RMSE				
	Moeser et al	Standard model	Moeser et al.	Standard model	Moeser et al	Standard model	Moeser et al.	Standard model			
≤ 25%	0.78	0.62	2.7	6.8	0.57	0.37	21	22	< 27	< 2	.82-.99
25-50%	0.67	0.45	3.5	5.6	0.48	0.26	18	20	27 - 181	2 - 6	.81-.99
50-75%	0.61	0.07	3.4	4.5	0.37	- 0.08	23	32	181 - 665	6 - 12	.79-.99
> 75%	0.52	-0.22	3.5	4.1	0.17	- 0.13	24	39	> 665	> 12	.70-.99

5.3.5   Transferability and research gaps

In spite of the key steps forward that are represented by the new snow interception model developed here, this project has highlighted the complexity of modeling under-canopy snow as well as several important research gaps.

Due to the indirect measurement technique for interception, no field measurements of unloading, melt and drip or sublimation were taken. Snow unloading is an extremely complex process that depends on the timing, duration, amount and density of precipitation (current and prior) falling onto the canopy (cf. section 2.8.1). Canopy and branch-bending characteristics in conjunction with precipitation further determine how much and where the snow will unload. Finally, temperature, wind and solar radiation dictate when the snow will unload. It is also common for snow to follow preferential unloading paths, e.g. when the unloaded snow falls from one particular side or section of the canopy. Research in warmer winter climates (e.g., Pacific Northwest, USA), beginning with work in Japan [Shidei et al., 1952] has also illustrated the importance of melt and drip processes (not modeled within FSM) and demonstrated its relationship to temperature [Clark et al. 2015b; Friesen et al. 2015; Lundquist et al. 2013; Martin et al. 2013]. However, quantifying the effects of intercepted snow on under-canopy SWE and runoff will not be fully possible until it is known how much and when intercepted snow falls to the ground in all climates.

It is unclear how this model (eq. 11- 17) would perform for forest types other than Norway spruce. In principle, the benefits of the new Imax model that utilizes stand-scale metrics should be species-independent. Yet, it is unclear how the variables k and Po, which dictate the rate of interception efficiency and the maximum efficiency, may change if the model was transferred to new areas. It is possible that the formulation underlying these variables is related to snow density and/or tree species (as long as the constraint of eq. 10 is not violated). Intuitively, this makes sense: the denser or 'stickier' the snow, the higher the potential rate of snow bridging (up to a certain point at least).

Both interception models require detailed data to characterize the canopy. In both models, this is the primary crux in implementation over large model domains. LAI and CC (CC is utilized in both models and LAI is utilized in the standard model), require sufficiently high resolution remotely sensed data for effective derivation of these elements. Total gap area and mean distance to canopy (utilized only in the new model) have, to date, only been derived using high resolution LiDAR data. However, the estimation of these metrics does not require a high point cloud density. Furthermore, the algorithm that was used to derive these metrics first transformed the data into a grid, removing any dependence on a high point cloud density. TGA and MDC could potentially be derived from other, lower resolution gridded data sets. It is conceivable that photogrammetric methods could be used in place of aerial LiDAR data to accurately derive these metrics (TGA, and MDC). It is also possible high resolution aerial imagery could be used, provided that information on the photo angle is retained.

5.4   Conclusion

The conversion of a storm based interception model to a model applicable at discrete model time steps was successfully achieved by the derivation of a new system of equations (eq. 11 – 17), which allowed for a numerically stable implementation in a large-scale snowmelt model, FSM. Given that the new interception model inherently includes unloading during snowfall, these guiding equations can be used in other snowmelt models as long as the corresponding unloading model is not utilized during snowfall events.

The inclusion of forest scale metrics (total gap area, and mean distance to canopy) in the Moeser et al. interception model had major impacts on simulated interception. The largest differences between the standard and the new interception model were evident at the canopy-open area interfaces and the open areas. The standard model showed very little variation of interception estimates regardless of differences in total gap area or mean distance to canopy, with a maximum cumulative seasonal interception range of ~145 mm SWE between all points. This was contrasted by the new interception model, which showed a variance of ~285 mm SWE between all points and a better fit with measured data. The variance within the new interception model was dictated by the canopy structure, with high

interception values in dense canopy with low MDC and TGA values and subsequently lower interception estimates as MDC and TGA increased. Field points that feature similar CC can have very different large-scale canopy structures (MDA, TGA). However, the standard model is not able to discriminate between such points.

The spatial heterogeneity of the forest environment was also represented farther down the modeling chain in the new approach. Larger variations of under-canopy SWE / SD as well as sublimation were featured by the new model as compared to the standard model. The new interception module resulted in SD simulations that were consistent with the small-scale patterns evident from the ground observations. The updated FSM represents one of the first snowmelt models that is able to reflect the spatial variability in forest snow caused by local heterogeneity in the canopy.

The new function used to model interception efficiency had a systematic impact on interception estimates. It accounted for snow bridging and branch bending, where interception efficiency rose to a maximum with increasing precipitation and then decreased. This was contrasted by the standard model, which featured an exponential reduction of interception efficiency as precipitation increased. These differences demonstrated, at least for these study areas, which are characterized by frequent small storms, higher estimates of interception from the standard model in areas with moderate to large open areas. The opposite was also true, with large storms, the standard model led to lower estimates in all openness regimes. If the Moeser et al. interception model was implemented for climates characterized by large storms events, it would yield significantly higher interception estimations than the standard model (and subsequently lower under-canopy snow estimates).

While the benefits of the inclusion of new canopy structure parameters (MDC, TGA) should be universal, it remains to be seen whether a sigmoidal interception function is also suitable for other climates or other tree species. Further research should address the applicability of this interception model in different forest regions worldwide.

Acknowledgements:

6

6. Synthesis

6.1 General Discussion

Filling the research gaps: A new interception model valid for discrete time steps, various scales and heterogeneous canopy structures was developed and implemented as the sum of the work described in chapters 2-5. The model was designed to fill several research gaps (RG) that had been highlighted in the most recent snow model inter-comparison project (Snowmip2), which assessed the skill of snow melt models in forests. This assessment revealed a much lower consistency of snow melt model results for forested areas than for open areas. The project further highlighted the limitations of the sometimes overly simplistic representation of canopy structure within the models. Specific findings revealed a particular need to:

- RG1: Predict SWE under forest canopies relative to SWE in the open and improve the consistency of model simulations between open and forested sites.
- RG2: Understand the partitioning of snow precipitation that i) immediately reaches the ground, ii) is intercepted by the forest canopy and subsequently unloaded to the ground, and iii) remains intercepted until sublimating into the atmosphere.

Intuitively, the spatial distribution of under-canopy SWE should mimic the overlying canopy; extensive field work from the largest forest snow data set ever collected has demonstrated this (1932 surveyed under-canopy points and 84000 manual measurements). The simulation results further showed similar snow distribution patterns and predicted under-canopy SWE relative to open areas at a resolution never before obtainable (RG1). Thus, this is the first model to effectively and accurately represent small-scale snow distribution heterogeneity under forest canopies based on an improved partitioning of 'snowfall which is intercepted' vs. 'snowfall which immediately reaches the ground' (RG2).

This research has shown that simplified representations of canopy structure – often present in earlier interception models (such as LAI and CC in the standard model) – deliver homogenous results that are incapable of representing the heterogeneous nature of the canopy and its effects on snow cover dynamics. The new model integrates novel canopy metrics (total gap area around a point [TGA] and mean distance to canopy from a point [MDC]), which quantify the size and generalized location of a forest gap around a point. Two physical processes were readily evident in the field data: snow bridging and branch bending. The inclusion of these processes represented a major deviation from the underlying interception modeling assumptions in many earlier efforts. The pairing of these processes with larger-scale forest metrics (TGA, MDC) has allowed for the first time to accurately represent the extreme spatial variability of forest snow. These differences from the standard model not only provide better representations of interception and under-canopy snow at the point scale, but they also allow for improved snow modeling over larger areas.

Evaluation of past research: This research provided a unique opportunity to review older findings, examine them from a new perspective and integrate them into novel interception model.

The model developed in this thesis represents a synthesis of ideas from earlier research extending over more than a century. A fitting example is the work of James Church. In 1912 he described the snow holding capacity of a forest as a 'honeycomb matrix' (see Introduction) and stated that the snow-holding capacity of a forest depended on canopy density and the 'closeness of trees to each other'. He also concluded that the water holding capacity of a forest gap was directly proportional to the height of the surrounding trees. Based on research dating back to the time of Dr. Church we know that two points with identical LAI but with different canopy gap distributions may feature different SWE values. Until now, however, snowmelt models have only included descriptions of interception through canopy density metrics (CC, LAI) and were not able to differentiate between such points. The inclusion of forest stand scale metrics in snow models can decipher how the canopy density of a specific element is positioned relative to the surrounding canopy structure, or in the words of James Church, the 'closeness of trees to each other'.

Satterlund and Haupt (1967) quantified snow bridging and branch bending from their observations in temperate coniferous forests and proposed a sigmoidal model to represent these phenomena. Until now, no snowmelt models have integrated the interplay of these mechanisms; instead they used exponential decay functions or static multipliers of incoming precipitation to represent interception. Our interception dataset (~8500 measurements) demonstrated snow bridging and branch bending and was regularly observed within all of the field sites. We also advanced the ideas of Satterlund and Haupt by updating and integrating the sigmoidal curve into the new interception model.

Development of new ideas: Novel canopy metrics were developed and integrated which no longer limits snowmelt models to forest descriptions from traditional parameters and techniques.

The quantity and quality of remotely sensed (RS) data such as ALS are constantly improving, and large areas of the world now have data available. The primary advantages of RS techniques for forest research lie in the ability to quickly assess large areas. This allows for the derivation of large-scale features, which is not possible with standard ground-based methods such as hemispherical photography. In order to accurately apply an interception model over heterogeneous forests, information is needed, among others, on the position of canopy openings (gaps) relative to the surrounding canopy. This necessitates the development of new canopy metrics that represent such forest stand-scale metrics for a point.

A novel method was created from ALS data to estimate various aspects of gap openings around a point. The vector-searching algorithm detailed in Chapter three has automated the process of determining two important forest metrics: TGA and MDC. These metrics were able to effectively constrain the interception model in terrain that is characterized by highly heterogeneous canopies. Earlier interception models were prone to interception overestimates within forest gaps and these metrics are able to considerably reduce these errors. When used in tandem with CC, these parameters act as a generalized coordinate system by defining the size of a gap (if any) around a point and determine its relative position within the gap.

6.2   Conclusion

6.2.1   Remote sensing

Synthetic images: As with all methods that employ RS to estimate canopy density, the principal improvement over ground-based methods is the ability to characterize large areas in a relatively short amount of time. The synthetic images can be directly compared to the validation data (hemispherical photos). Even when no hemispheric photo is available for comparison, the synthetic images provide a visual analysis to qualitatively validate the output metrics which removes the 'black box' output quandary from standard RS techniques.

The synthetic images accurately estimated CC and LAI when compared to hemispherical photographs (r: 0.93 / RMSE: 0.037 for CC and r: 0.83 / RMSE: 0.813 for LAI) for almost 2000 points in the field sites. This method has several advantages over the standard ALS derivation method. First, the standard method was not able to predict LAI at values above 4. Second, the standard method demonstrated a universal underestimation bias of almost an order of magnitude, which required a secondary regression to offset. Although the standard method performed well for CC (r: 0.91), a significant underestimation bias was evident, and similar to the LAI estimates (using the standard method), this required a secondary regression to calibrate the offset.

Potential incoming solar radiation (PISR) was analyzed from the synthetic images and resulted in a simulated radiation regime (time series) at each field point. This method allowed for a flexible partitioning of direct and diffuse incoming radiation that was dependent on the time and point used. This method demonstrated average correlations from 0.90 to 0.94 when compared to a series of radiometer surveys at 30 points during clear sky conditions. The direct and diffuse radiation components were well represented at all values of canopy closure up to 0.85. Yet, for CC >0.85, the direct radiation component was underestimated and required a scaling function.

Forest structure metrics: For more robust modeling at scales greater than the point scale, the greater canopy topography needs to be analyzed. A vector searching algorithm was developed to describe large scale forest features and derived over 50 parameters intended to describe canopy openness

around a point. As with the synthetic images, this approach allowed for (1) a rapid characterization of large areas and (2) the derivation of parameters for each field point in a period of minutes. All parameters were then correlated to the field-based interception ratio measurements. A novel pairing of correspondence analysis and k-means clustering was used to analyze the potential cross-correlations between each parameter. The analysis highlighted variables highly correlated with interception ratio: mean distance to canopy and total gap area, which also demonstrated low cross-correlation. LAI, however, displayed a low correlation with interception ratio and a large cross-correlation with CC. This implies that the use of LAI with CC, as done in the standard interception model, does not provide better estimations of interception ratio than CC alone. Rather, a pairing of CC with larger-scale metrics such as TGA and MDC would allow for not only a better representation of the interception ratio in a uniform forest, but particularly in areas with heterogeneous canopy cover.

The vector-searching algorithm and the synthetic image creator have been programmed flexibly in order to be applicable to other data sets. Each program is available upon request and contains sample datasets and basic user guidelines. All parameters associated with the respective program can be easily manipulated in order to fit specific datasets.

6.2.2   Interception modeling

Storm Interception Model: Storm-based interception was accurately modeled for a large range of canopy densities. The model displayed a good fit at the point scale (r^2: 0.65 / RMSE: 3.35), which represents a 25% increase in the r^2 and a reduction of 53% of the RMSE when compared to the standard interception model. The standard model was characterized by a significant underestimate of interception for larger storms as a well as an overestimate for small storms. This was primarily due to the use of an exponential decay function that did not account for snow bridging. In contrast, the Moeser et al. model integrates a sigmoidally shaped distribution of interception efficiency, which accounts for the effects of snow bridging between canopy elements as well as branch bending. However, only half (52% of the r2 and 33% of the RMSE) of the improvement of the Moeser et al. model could be attributed to the underlying distribution.

The other half was due to inclusion of canopy metrics that described large-scale forest features: MDC and TGA. These features permitted better performance under heterogeneous canopy terrain. Primarily they allowed for differentiation between 'points with similar canopy closure (or LAI) situated near or in a canopy gap' and 'points with similar canopy closure (or LAI) not situated near or in a canopy gap'. These metrics further allowed for improvements when the model was up-scaled to larger grid cell sizes: increased correlation and decreasing bias were observed in both models. Yet, as grid cell size increased, the Moeser et al. model displayed much higher decreases of RMSE (75% - 114%) when compared to the standard model.

Interception model implementation: The storm-based Moeser et al. model (from chapter 5) necessitated conversion to a model valid at discrete time steps. This required the derivation of a new system of equations as well as a new variable, Pstorm. This variable accumulates precipitation and thus creates the link between the 'storm step' and uniform time steps. Pstorm, in conjunction with the system of equations (eq.11 – 17 in Chapter 6), allows the model to be implemented into any snowmelt model as long as the affiliated unloading module is not utilized during snowfall events. Even though the model could be applied at discrete time steps during inter-storm periods, the model is based on data collected after storm events. As a result, unloading is naturally integrated into interception estimates during storm events.

This new model features a high degree of variance in the interception estimates between each modeled point and dictated the layout of the overlying canopy structure. These results deviate significantly from those of the standard model primarily within canopy gaps and at the canopy-open area interface. Furthermore, the standard model shows relatively little variance regardless of the position relative to canopy gaps, and has a two-fold decrease in variance between points as compared to the new model.

Lastly, the new model represents the heterogeneity of the canopy down the modeling chain. Application of the new model leads to approximately twice the variance of under-canopy SD, under-canopy SWE and sublimation of intercepted snow when compared to the standard model. Similar to the interception

estimations, the variation of these estimates was tied directly to the spatial distribution of the canopy structure. This is not evident from the standard model.

6.3   Limitations and Research Recommendations

6.3.1   Snow unloading

The synthesis of Chapters 2 through 5 filled several research gaps that had been highlighted in the Snowmip2 project (RG1 & RG2 above). However, part ii of RG2 – i.e., the partitioning between snowfall that is intercepted and snowfall that is unloaded from the canopy – was not fully investigated due to the requisite time involved in order to create such a model. Yet, there continues to be a need for a model capable of capturing the process of snow unloading. Specifically, this work has shown that quantifying the effects of intercepted snow on under-canopy SWE and runoff will not be fully possible until it is known how much and when intercepted snow falls to the ground.

Snow unloading is an extremely complex process that depends on the timing, duration, amount and density of precipitation (current and prior) falling onto the canopy. Canopy and branch-bending characteristics in conjunction with precipitation further determine how much and where the snow will unload. Finally, temperature, wind and solar radiation dictate when the snow will unload. It is also common for snow to follow preferential unloading paths, e.g. when the unloaded snow falls from one particular side or section of the canopy (cf. Introduction, figure 1d). The interplay of these factors creates large spatial heterogeneity of snow unloading that current models do not account for, as reviewed below.

The standard unloading model developed by Hedstrom and Pomeroy (1998) assumed that unloading is proportional to the intercepted snow load and decreases exponentially as intercepted snow decreases. The model unloads all snow off a canopy in the same amount of time regardless of the initial amount of snow in the canopy. Liston et al (2006) created an unloading mechanism based on air temperature, with unloading occurring only after air temperature was >0 °C. Finally, Rösch et al. (2001) combined these two approaches and further included wind as a determinant of unloading. The wind thresholds used in this model, however, were chosen in an arbitrary manner. None of these models have

integrated field data explicitly, and thus cannot effectively represent the complexity of the phenomena. While the new interception model integrated unloading processes during storm events, there is still a need for a stand-alone snow unloading model applicable in all precipitation regimes.

6.3.2 Small precipitation events

Indirect measurements of interception have clear advantages. Most importantly, they allowed for measuring a large number of points under a variety of canopy constraints, which would simply not have been feasible with direct measurements (e.g., weighing tree experiments). However, indirect measurement limited the present research to storm sizes >15 cm of SD (in the open), which necessitated assumptions of interception efficiency during small events. It remains unclear whether interception efficiency during small precipitation events demonstrates the same characteristics as during larger events. For example, Schmidt and Gluns (1991) showed that during very low precipitation events, initial interception efficiency decreased before an efficiency increase was measured (~1 mm SWE and less). Supplementing the present work with direct interception measurements would be highly useful to improve the model assumptions during small storm events.

6.3.3 Model transferability: climate and canopy conditions

This model was calibrated and validated in one region. Still, the benefits of the new model structure parameters and should be universal. Yet, it is unclear how the variables k and P_o, which dictate the rate of interception efficiency and the maximum efficiency, may change if the model was transferred to new areas. It is possible that the formulation underlying these variables is related to snow density. Intuitively, this idea makes sense: the denser or 'stickier' the snow, the higher the potential rate of snow bridging (to a point). In this study (Chapter 4), however, these variables displayed no correlation with snow density, although it remained unclear whether this was due to the small range of densities and/or the limited number of storms that were measured.

It is also possible that these variables are a function of tree species (when TGA and MDC are low). Norway spruce, the dominant species in this study, typically has flexible and slightly upturned branches (depending upon tree size). This had a large impact on the potential canopy surface area as weight

was applied to the branches. These characteristics as they relate to interception efficiency can be mechanistically described in the following idealized example:

> When snow falls, the upturned branches bend downward. As the branches reach the planar position (~90° angle relative to the trunk), the potential snow surface area of the canopy reaches a maximum. When more weight is applied past the planar position, the surface area decreases. Dependent on the prior branch angle, the potential snow surface area can be augmented or attenuated by snow bridging.

Bründl et al. (1999) quantified the above relationship in a unique experiment in which ping-pong balls were hung on the branches of a Norway spruce tree. The offset of the balls as induced by snow load was quantified using time-lapse photos during storm events. There is no research to date, however, that has quantified these relationships for different tree species. Thus, the new interception model developed in this research should be tested in other areas to judge whether tuning of these parameters is in fact needed and if so create a tuning parameter based on climate conditions and/or tree species.

6.3.4   Synthetic image point size distribution

The creation of the synthetic images required a point size distribution to be defined. That is, when canopy elements defined from ALS occurred close to a predefined center point, a large point size was printed within the image. A small point size was printed when an ALS element was far from the center point. The point sizes were linearly distributed from small to large and the distribution range was optimized using a comparison to hemispherical photos.

The point size range, however, depends on the echo density of the ALS data. This requires a re-analysis of the point size range if other datasets with different echo densities are used to generate synthetic images. However, it is possible that the ALS point cloud density could be integrated into a general scaling function of the point size range. A logical next step would therefore be a comparison of ALS data of differing echo densities to hemispheric photos in order to derive such a function.

6.3.5   Vector-searching algorithm

The vector-searching algorithm utilized a smoothing function (neighborhood cell mean filter) in order to manage erroneous ALS data scatter. In order to implement the data smoother, the CHM (canopy height model) from the ALS cloud was transformed into a raster. A smoothing factor was integrated with the smoothing function that represented a minimum canopy density that was required to be considered a canopy element. In this case, the smoothing factor was optimized to 0.9, i.e. 90% of the surrounding raster cells (¼ m x ¼ m in size) must also have canopy elements to be considered canopy. It is unclear if the optimized smoothing factor and optimized raster cell size would change if other data sets were employed. As with the point size distribution, a comparison of varying ALS point cloud densities could be used to arrive at a general function to determine the optimal smoothing factor and raster size.

This algorithm uses data converted to a raster; therefore a high point cloud density is not necessarily needed. It is possible that other RS data sources could be used in place of ALS. The use of other techniques such as photogrammetry could represent a significant cost and time savings as compared to the high equipment and data manipulation cost inherent to large ALS flyovers.

6.3.6   Research continuum

Despite the above limitations, this research is a major step forward and greatly improves the process understanding and modeling of snow interception. The effects of interception on under-canopy snow melt processes can now not only be effectively represented but also related to canopy structure characteristics. It is hoped that this work, like much of the significant prior work upon which it is based, will also be used as a stepping stone for improved understanding and modeling of forest snow processes in the future.

References 7

Alexander, C., Moeslund, J.E., Bøcher, P.K., et al., 2013. Airborne laser scanner (LiDAR) proxies for understory light conditions. Remote Sens. Environ., 134, 152-161.

Anderson, E. A., 1976. A point energy and mass balance model of a snow cover, NOAA Tech. Rep. NWS 19, U.S. Dept. of Commerce, Silver Spring, Md.

Andreadis, K.M., Storck, P., Lettenmaier, D.P., 2009. Modeling snow accumulation and ablation processes in forested environments. Water Resources Research, 45(5) W05429.

Asner, G.P., Mascaro, J., Muller-Landau, H.C., et al., 2011. A universal airborne LiDAR approach for tropical forest carbon mapping. Oecologia, 168(4): 1147-1160.

Best, M.J., Pryor, M., Clark, D.B., et al., 2011. The Joint UK land environment simulator (JULES), model description – Part 1: Energy and water fluxes. Geoscientific Model Development, 4(3): 677-699.

Boone, A., 2009. Description du schema de neige ISBA-ES (Explicit Snow). Centre National de Recherches Mètèorologiques, Mètèo-France.

Breda, N., 2003. Ground-based measurements of leaf area index: a review of methods, instruments and current controversies. J. Exp. Bot., 54(392): 2403-2417.

Bunnell, F.L., McNay, R.S.,Shank, C.C., 1985. Trees and snow: the deposition of snow on the ground - a review and quantitative synthesis. Research, Ministries of Environment and Forests. IWIFR-17. Victoria, B.C.

7. References

Bründl, M., Bartelt, P., Schneebeli, M., Flühler, H., 1999. Measuring branch defection of spruce branches caused by intercepted snow load. Hydrological Processes, 13(14-15): 2357-2369.

Calder , I.R., 1991. Evaporation in the uplands. John Wiley & Sons, Chichester, New York.

Car, J., 2002. Data visualization in the geological sciences. Prentic Hall, Upper Saddle River, NJ.

Carpenter, L.G., 1901. Forests and snow. Colorado Agricultural Experiment Station, Bulletin 55.

Chang, M., 2003. Forest hydrology: An introduction to water and forests. CRC Press, Boca Raton, 392 pp.

Clark, M.P., Nijssen, B., Lundquist, J.D., et al., 2015a. A unified approach for process-based hydrologic modeling: 1. modeling concept. Water Resources Research, 51, 2498-2514.

Clark, M.P., Nijssen, B., Lundquist, J.D., et al., 2015b. A unified approach for process-based hydrologic modeling: 2. Model implementation and case studies. Water Resources Research, 51, 2515-2542.

Clark, M.P., Nijssen, B., Lundquist, J.D., et al., 2015c. The structure for unifying multiple modeling alternatives (SUMMA), version 1.0: technical description. In, NCAR Technical Notes NCAR/TN 514+STR. Boulder, CO USA: National Center for Atmospheric Research.

Church, J.E., 1912. The conservation of snow: its dependence on forests and mountains. Scientific American supplement, 74: 152-155.

Cox, P.M., Betts, R.A., Bunton, C.B., et al., 1999. The impact of new land surface physics on the GCM simulation of climate and climate sensitivity. Climate Dynamics, 15(3): 183-203.

Douville, H., Royer, J., Mahfouf, J., 1995. A new snow parameterization for the Meteo-France climate model part I: validation in stand-alone experiments. Climate Dynamics, 12: 21-35.

Dutra, E., Balsamo, G., Viterbo, P., et al., 2010. An improved snow scheme for the ECMWF land surface model: description and offline validation. Journal of Hydrometeorology, 11(4): 899-916.

Egli, L., Jonas, T., Meister, R., 2009. Comparison of different automatic methods for estimating snow water equivalent. Cold Regions Science and Technology, 57(2-3): 107-115.

Ellis, C.R., Pomeroy, J.W., Brown, T., MacDonald, J., 2010. Simulation of snow accumulation and melt in needleleaf forest environments. Hydrology and Earth System Sciences, 14(6): 925-940.

United Nations Environment Program, 2007. Environment for Development Assessment Report Rep., 572 pp, United Nations, Nairobi, Kenya.

Erdody, T.L., Moskal, L.M., 2010. Fusion of LiDAR and imagery for estimating forest canopy fuels. Remote Sensing of Environment, 114, 725-737.

Essery, R., 2015. A Factorial Snowpack Model (FSM 1.0). Geosci. Model Dev. Discuss., 8, 6583-6609.

Essery, R., Morin, S., Lejeune, Y., B Ménard, C., 2013. A comparison of 1701 snow models using observations from an alpine site. Advances in Water Resources, 55: 131-148.

Esssery, R., Rutter, N., Pomeroy, J., et al., 2009. SNOWMIP2 An evaluation of forest snow process simulations. Bulletin of The American Meteorological Society: 1120-1135.

Essery, R., Bunting, P., Hardy, J., et al., 2008. Radiative transfer modeling of a coniferous canopy characterized by airborne remote sensing. J. Hydrometeorol., 9, 228-241.

Essery, R., Pomeroy, J.,Ellis C., Link, T., 2008. Modelling longwave radiation to snow beneath forest canopies using hemispherical photography or linear regression, Hydrological Processes, 22(15), 2788-2800.

Essery, R., Pomeroy, J., Parviainen, J., Storck, P., 2003. Sublimation of snow from coniferous forests in a climate model. J. Clim., 1855-1864.

7. References

Essery, R., Pomeroy, J., 2001. Soil-Vegetation-Atmosphere transfer schemes and large-scale hydrological models international association of hydrological science conference, Maastricht, Netherlands, pp. 343-347.

Fiala, A.C.S., Garman, S.L., Gray, A.N., 2006. Comparison of five canopy cover estimation techniques in the western Oregon Cascades. Forest Ecol. and Manag., 232, 188-197.

Fleck S., Cater, M., Schleppi, P., et al., 2012. Manual on methods and criteria for harmonized sampling, assesment, monitoring and analysis of the effects of air pollution on forests: part XVII, leaf area measurements. In, United Nations Economic Commission for Europe International Co-operative programme on Assesment and Monitoring of Air Pollution Effects on Forests (ICP 469 Forests).

Friesen, J., Lundquist, J., Van Stan, J.T., 2015. Evolution of forest precipitation water storage measurement methods. Hydrological Processes, 29, 2504-2520.

Guntner, A., Stuck, J., Werth, S., et al., 2007. A global analysis of temporal and spatial variations in continental water storage. Water Resour. Res., 43.

Golding, D.L., Swanson, R.H., 1986. Snow distribution in clearings and adjacent forest. Water Resour. Res., 22(13)., 1931-1940.

Greenacre, M., Blasius, J., 1994. Correspondence analysis in the social sciences. Academic Press, Waltham, MA, 370 pp.

Guntner, A., Stuck, J., Werth, S., et al., 2007. A global analysis of temporal and spatial variations in continental water storage. Water Resour. Res., 43(5) W05416.

Harding, R.J., Pomeroy, J., 1996. Energy balance of the winter boreal landscape. Journal of Climate, 9(11): 2778-2787.

Hedstrom, N.R., Pomeroy, J., 1998. Measurements and modelling of snow interception in the boreal

forest. Hydrol. Processes, 12(10-11)., 1611-1625.

Hellström, R., 2000. Forest cover algorithms for estimating meteorological forcing in a numerical snow model. Hydrol. Processes, 14, 3239-3256.

Huld, T., Šúri, M., Dunlop, E.D., 2008. Comparison of potential solar electricity output from fixed-inclined and two-axis tracking photovoltaic modules in Europe. Progress in Photovoltaics: Research and Applications, 16, 47-59.

Hyer, E.J., Goetz, S.J., 2004. Comparison and sensitivity analysis of instruments and radiometric methods for LAI estimation: assessments from a boreal forest site. Agric. For. Meteorol., 122(3-4)., 157-174.

Intergovernmental Panel on Climate Change, 1997. The Regional Impacts of Climate Change: An Assesment of Vulnerability. Watson, R.T., Zinyowera, M.C., Moss, R.H., (eds); Rep., 517 pp, , Cambridge.

Jonas, T., Essery, R., 2011. Snow cover and snowmelt in forest regions. In: Singh, V.P., Haritashya, U.K., (eds.), Encyclopedia of snow, ice and glaciers, Series: Encyclopedia of Earth Sciences Series. Dordrecht Heidelberg, Springer, 1033-1036.

Johnson, W.M., 1942. The interception of rain and snow by a forest of young ponderosa pine. Trans. Am. Geophys. Union, 23:566-570.

Jordan, R., 1991, A one-dimensional temperature model for a snow cover, technical documentation for SNTHERM.89, special technical report 91-16, U. S. Army Cold Regions Research and Engineering Laboratory, Hanover, N.H.

Kato, A., Moskal, L.M., Schiess, P., et al., (2009). Capturing tree crown formation through implicit surface reconstruction using airborne lidar data. Remote Sensing of Environment, 113, 1148-1162.

7. References

Kavetski, D., Kuczera, G., 2007. Model smoothing strategies to remove microscale discontinuities and spurious secondary optima in objective functions in hydrological calibration. Water Resources Research, 43(3) W03411.

Kienzle, S.W., 2008. A new temperature based method to separate rain and snow. Hydrological Processes, 22, 5067-5085.

Kobayashi, D., 1987. Snow Accumulation on a narrow board. Cold Regions Science and Technology, 13: 239-245.

Koivusalo, H., Kokkonen, T., 2002. Snow processes in a forest clearing and in a coniferous forest. J. Hydrol., 262: 145-164.

Korhonen, L., Morsdorf, F., 2014. Estimation of canopy cover, gap fraction and leaf area index with airborne laser scanning. In: Maltamo, M., Naesset, E., Vauhkonen, J. (Eds.), Forestry Applications of Airborne Laser Scanning: concepts and Case Studies. Springer Science and Business Media, Dordrecht, pp. 464.

Leeuwen, M., Nieuwenhuis, M., 2010. Retrieval of forest structural parameters using LiDAR remote sensing. European Journal of Forest Research, 129, 749-770.

Li, W.,P., Luo, Y., Xia, K., Liu, X., 2008. Simulation of snow processes beneath a boreal Scots pine canopy. Advances in Atmospheric Sciences 25: 348-360.

Link, T.E., Marks, D., Hardy, J.P., 2004. A deterministic method to characterize canopy radiative transfer properties. Hydrol. Processes, 18, 3583-3594.

Liston, G.E., Elder, K., 2006. A distributed snow-evolution modeling system (SnowModel). Journal of Hydrometeorology, 7(6): 1259-1276.

Lopez-Moreno, J.I., Latron, J., 2008a. Influence of canopy density on snow distribution in a temperate mountain range. Hydrological Processes, 22(1): 117-126.

Lopez-Moreno, J.I., Stahli, M., 2008b. Statistical analysis of the snow cover variability in a subalpine watershed: Assessing the role of topography and forest, interactions. Journal of Hydrology, 348(3-4): 379-394.

Lorenzo-Seva, U., Van de Velden, M., Kiers, H., 2009. Oblique rotation in corrrespondence analysis: a step forward in search of the simplest interpretation. Br. J. Math. and Stat. Psychol., 62: 583-600.

Lovell, J.L., Jupp, D.L.B., Culvenor, D.S., et al., 2003. Using airborne and ground-based ranging lidar to measure canopy structure in Australian forests. Can. J. of Remote Sens., 29(5): 15.

Lundberg, A., Halldin, S., 2001. Snow interception evaporation - rates, processes and measurement techniques. Theor. Appl. Climatol., 70: 117-133.

Lundberg, A., Calder, I., Harding, R., 1998. Evaporation of intercepted snow: measurement and modelling. Journal of Hydrology, 206(3-4): 151-163.

Lundberg, A., Halldin, S., 1994. Evaporation of intercepted snow: analysis of governing factors. Water Resources Research, 30(9): 2587-2598.

Lundquist, J.D., Dickerson-Lange, S.E., Lutz, J.A., Cristea, N.C., 2013. Lower forest density enhances snow retention in regions with warmer winters: a global framework developed from plot-scale observations and modeling. Water Resources Research, 49, 6356-6370.

Magnusson, J., Wever, N., Essery, R., et al., 2015. Evaluating snow models with varying process representations for hydrological applications. Water Resources Research, 51(4): 2707-2723.

Mahat, V., Tarboton, D.G., 2014. Representation of canopy snow interception, unloading and melt in a parsimonious snowmelt model, Hydrological Processes, 28(26), 6320-6336.

7. References

Marks, D., Winstral, A., Reba, M., et al., 2013. An evaluation of methods for determining during-storm precipitation phase and the rain/snow transition elevation at the surface in a mountain basin. Advances in Water Resources, 55, 98-110.

Marks, D., Dozier, J., Davis, R.E., 1992. Climate and energy exchange at the snow surface in the alpine region of the Sierra Nevada, I: meteorological measurements and monitoring, II: Snowcover energy balance, Water Resour. Res., 28(11), 3029-3054.

Martin, K.A., Van Stan, J.T., Dickerson-Lange, S.E., et al., 2013. Development and testing of a snow interceptometer to quantify canopy water storage and interception processes in the rain/snow transition zone of the North Cascades, Washington, USA. Water Resources Research, 49, 3243-3256.

Meiman, J.R., Grant, L., 1974. Snow-Air interactions and management on mountain watershed snowpack, Colorado State University. Environmental Research Center Belletin, Fort Colins, Colorado.

Miller, D.H., 1964. Interception processes during snowstorms, US Department of Agriculture, Berkeley, CA.

Moeser, D., Roubinek, J., Schleppi, P., et al., 2014. Canopy closure, LAI and radiation transfer from airborne LiDAR synthetic images. Agric. For. Meteorol., 197: 158-168.

Moeser, D., Morsdorf, F., Jonas, T., 2015a. Novel forest structure metrics from airborne LiDAR data for improved snow interception estimation. Agricultural and Forest Meteorology, 208: 40-49.

Moeser, D., Stähli, M., Jonas, T., 2015b. Improved snow interception modeling using canopy parameters derived from airborne LIDAR data. Water Resources Research: 51(7): 5041-5051.

Molotch, N.P., Blanken, P.D., Williams, M.W.,et al., 2007. Estimating sublimation of intercepted and sub-canopy snow using eddy covariance systems. Hydrological Processes, 21(12): 1567-1575.

Montesi, J., Elder, K., Schmidt, R.A., Davis, R.E., 2003. Sublimation of intercepted snow within a subalpine forest canopy at two elevations. J. Hydrometeorol., 5(5): 763-773.

Morsdorf, F., Frey, O., Meier, E., et al., 2008. Assessment of the influence of flying altitude and scan angle on biophysical vegetation products derived from airborne laser scanning. Int. J. Remote Sens., 29(5): 1387-1406.

Morsdorf, F., Kötz, B., Meier, E., et al., 2006. Estimation of LAI and fractional cover from small footprint airborne laser scanning data based on gap fraction. Remote. Sens. Environ., 104(1): 50-61.

Morsdorf, F., Meier, E., Kötz, B., et al., 2004. LIDAR-based geometric reconstruction of boreal type forest stands at single tree level for forest and wildland fire management. Remote. Sens. Environ., 92(3): 353-362.

Musselman, K.N., Margulis, S.A., Molotch, N.P., 2013. Estimation of solar direct beam transmittance of conifer canopies from airborne LiDAR. Remote Sens. Environ., 136, 402-415.

Musselman, K.N., Molotch, N.P., Margulis, S.A., et al., 2012. Influence of canopy structure and direct beam solar irradiance on snowmelt rates in a mixed conifer forest, Agric. For. Meteorol., 161, 46-56.

Nakai, Y., Sakamoto, T., Terajima, T., et al., 1999a. Energy balance above a boreal coniferous forest: a difference in turbulent fluxes between snow-covered and snow-free canopies, Hydrological Processes, 13(4), 515-529.

Nakai, Y.S., Terajima, T., Kitamura, T., et al., 1999b. The effect of canopy-snow on the energy balance above a coniferous forest. Hydrologic Processes, 113: 2371-2382.

Nakai, Y., Kitahara, H., Saito, T., 1994. Snow interception by forest canopies: weighing a conifer tree, meteorological observation and analysis by the Penman- Montheith formula. Snow and Ice Covers: Interactions with the Atmosphere and Ecosystems, Proceedings of Yokohama Symposia J2 and J5(223): 227-236.

7. References

Nobis, M., Hunziker, U., 2005. Automatic thresholding for hemispherical canopy-photographs based on edge detection. Agric. For. Meteorol., 128, 243-250.

Oleson, K., Lawrence, D., Bonan, G., Flanner, M., 2010. Technical description of version 4.0 of the community land model (CLM). National Center for Atmospheric Research, Climate and Global Dynamics Division, Boulder, CO.

Pfister, R., Schneebeli, M., 1999. Snow accumulation on boards of different sizes and shapes. Hydrological Processes, 13(14-15): 2345-2355.

Pomeroy, J., Ellis, C., Rowlands, A., et al., 2008a. Spatial variability of shortwave irradiance for snowmelt in forests. J. Hydrometeorol., 9, 1482-1490.

Pomeroy, J., Gray, D., Marsh, P., 2008b. Studies on snow redistribution by wind and forest, snow-covered area depletion, and frozen soil infiltration in Northern and Western Canada, in Cold Region Atmospheric and Hydrologic Studies. The Mackenzie GEWEX Experience, edited by M.-k. Woo, pp. 81-96, Springer Berlin Heidelberg.

Pomeroy, J., Hedstrom, N.R., Parviainen, J., 1999. The snow mass Balance of Wolf Creek, Wolf Creek Research Basin: Hydrology, Ecology, Environment. National Water Research Institute, Envrironment Canada, Saskatoon.

Pomeroy, J. Gray, D. M., Shook, K., et al., 1998a. An evaluation of snow accumulation and ablation processes for land surface modeling. Hydrol. Processes, 12: 2339-2367.

Pomeroy, J., Parviainen, J., Hedstrom, N.R., Gray, D.M., 1998b. Coupled modelling of forest snow interception and sublimation. Hydrol. Processes, 12: 2317-2337.

Pomeroy, J., Gray, D.,M., 1995. Snowcover: Accumulation, Relocation, and Management. NHRI science report No.7. Saskatoon, Canada.

Pugh, E., Small, E., 2012. The impact of pine beetle infestation on snow accumulation and melt in the headwaters of the Colorado River, Ecohydrology, 5(4), 467-477.

Price, A. G., Dunne, T., 1976. Energy balance computations of snowmelt in a subarctic area, Water Resour. Res., 12(4), 686-694.

Riaño, D., Valladares, F., Condés, S., Chuvieco, E., 2004. Estimation of leaf area index and covered ground from airborne laser scanner (Lidar) in two contrasting forests. Agric. For. Meteorol., 124(3-4): 269-275.

Roesch, A., 2006. Evaluation of surface albedo and snow cover in AR4 coupled climate models. J. Geophys. Res.-Atmos., 111(D15): 18.

Rohrer, M. D., 1989: Determination of the transition air temperature from snow and rain and intensity of precipitation. IAHS/WMO/ETH International Workshop of Precipitation Measurement, B. Sevruk, Ed., WMO, 475–482.

Rosengrant, M., Cai, X., Cline, S., 2002. Global water outlook to 2025. In, A 2020 vision for food, agriculture and the environment. Washington, D.C., USA: International Food Policy Research Institute.

Rutter, N., Essery, R., Pomeroy, J., et al., 2009. Evaluation of forest snow processes models (SnowMIP2). J. Geophys. Res., 114(D6).

Satterlund, D., Haupt, H., 1967. Snow Catch by Conifer Crowns. Water Resour. Res., 3(4).

Shidei T, Takahashi T, Takahashi K, Kataoka K. 1952. Study of the fallen snow on the forest trees. Bulletin of the Government Forest Experiment Station 54: 115‑164.

Schleppi, P., Paquette, A., 2013. Solar radiation in forests: theory for hemispherical photography. In: Fournier R., Hall R. (ed.), Hemispherical photography in forest science: theory, methods, applications (in press).

7. References

Schleppi, P., Conedera, M., Sedivy, I., Thimonier, A., 2007. Correcting non-linearity and slope effects in the estimation of the leaf area index of forests from hemispherical photographs. Agric. For. Meteorol., 144, 236-242.

Schmidt, R.A., Gluns, D., 1991a. Snowfall interception on branches of three conifer species. Can. J. For. Res., 21: 1262-1269.

Schmidt, R.A., 1991b. Sublimation of snow intercepted by an artificial conifer. Agricultural and Forest Meteorology, 144(3-4): 236-242.

Seber, G. A. F., 1984. Multivariate distributions, in Multivariate Observations, John Wiley & Sons, Inc., Hoboken, NJ, USA.

Solberg, S., 2010. Mapping gap fraction, LAI and defoliation using various ALS penetration variables. Int. J. Remote Sens., 31(5): 1227-1244.

Solberg, S., Brunner, A., Hanssen, K., et al., 2009. Mapping LAI in a Norway spruce forest using airborne laser scanning. Remote. Sens. Environ., 113(11): 2317-2327.

Späth, H., 1985. Cluster dissection and analysis: theory, FORTRAN programs, examples. Horwood.

Stähli, M., Jonas, T., Gustafsson, D., 2009. The role of snow interception in winter-time radiation processes of a coniferous sub-alpine forest. Hydrol. Processes, 23, 2498-2512.

Strasser, U., Bernhardt, M., Weber, M., et al., 2008a. Is snow sublimation important in the alpine water balance? The Cryosphere(2): 53-66.

Strasser, U., Corripio, J., Brock, B., et al., 2008b. Distributed modelling of snow processes in the Berchtesgaden National Park. In: Strasser, U. (Ed.), Alpine Snow Workshop. Berchtesgaden National Park research report, Munich, Germany.

Strasser, U., Corripio, J., Pellicciotti, F., et al., 2004. Spatial and temporal variability of meteorological variables at Haut Glacier d'Arolla (Switzerland) during the ablation season 2001: measurements and simulations. Journal of Geophysical Research: Atmospheres, 109(D3).

Sturm, M., Holmgren, J., Liston, G.E., 1995. A seasonal snow cover classification system for local to global applications. J. Clim., 8, 1261-1283.

Storck, P., Lettenmaier, D.P., Bolton, S.M., 2002. Measurement of snow interception and canopy effects on snow accumulation and melt in a mountainous maritime climate, Oregon, United States. Water Resour. Res., 38(11): 16.

Storck, P. (2000), Trees, snow and flooding: An investigation of forest canopy effects on snow accumulation and melt at the plot and watershed scales in the pacific northwest. Technical Report No. 161., 195 pp, University of Washington, Seattle. http://www.ce.washington.edu/pub/WRS/WRS161.pdf

Suzuki, K., Nakai, Y., 2008. Canopy snow influence on water and energy balances in a coniferous forest plantation in northern Japan. Journal of Hydrology, 352(1-2): 126-138.

Suzuki K.N., Yuichiro, O., Takeshi, N., et al., 2003. Effect of snow interception on the energy balance above deciduous and coniferous forests during a snowy winter. Paper presented at the IUGG - Water Resource Systems, Sapporo, Japan 2003.

Tarboton DG, Luce CH. 1996. Utah energy balance snow accumulation and melt model (UEB). Computer model technical description and users guide. Utah Water Research Laboratory and USDA Forest Service Intermountain Research Station.

Taylor, K.E., 2001. Summarizing multiple aspects of model performance in a single diagram. Journal of Geophysical Research, 106(D7): 7183.

7. References

Tennyson, L., Ffolliott, F., Thorud, D., 1974. Use of time lapse photography to assess potential interception in arizona ponderosa pine. Water Resources Bulletin - American Water Resources Association, 10(6).

Thimonier, A., Sedivy, I., Schleppi, P., 2010. Estimating leaf area index in different types of mature forest stands in 516 Switzerland: a comparison of methods. Eur. J. For. Res., 129, 543-562.

Timofeev, Y.M., Vasil'ev, A., 2008. Theoretical fundamentals of atmospheric optics. Cambridge, UK: Cambridge International Science Publishing.

Troendle, C.A., Meiman, J.R., 1986. The Effect of patch clearcutting on the water balance of a subalpine forest slope, 54th Annual Western Snow Conference, Phoenix, AZ.

US Army Corps of Engineers., 1956. Snow hydrology: summary report of the snow investigations, North Pacific Division, Portland, OR., pp. 437.

Van de Velden, M., Kiers, H., 2005. Rotation analysis in correspondence analysis. J. Classification, 22(2): 251-271.

Van de Velden, M., Kiers, H., 2003. An application of rotation in correspondence analysis, New Developments in Psychometrics. Springer Japan, Tokyo, pp. 471-478.

Varhola, A., Coops, N.C., 2013. Estimation of watershed-level distributed forest structure metrics relevant to hydrologic modeling using LiDAR and Landsat. J. Hydrol., 487, 70-86.

Varhola, A., Frazer, G.W., Teti, P., Coops, N.C., 2012. Estimation of forest structure metrics relevant to hydrologic modelling using coordinate transformation of airborne laser scanning data. Hydrol. Earth Syst. Sci., 16, 3749-376.

Varhola, A., Coops, N., Bater, C., et al., 2010a. The influence of ground- and lidar-derived forest structure metrics on snow accumulation and ablation in disturbed forests. Can. J. For. Res., 40(4): 812-821.

Varhola, A., Coops, N., Weiler, M., et al., 2010b. Forest canopy effects on snow accumulation and ablation: an integrative review of empirical results. J. Hydrol., 392(3-4): 219-233.

Veatch, W., Brooks, P.D., Gustafson, J.R., et al., 2009. Quantifying the effects of forest canopy cover on net snow accumulation at a continental, mid-latitude site. Ecohydrology, 2(2): 115-128.

Verseghy, D., 1990. CLASS - A Canadian land surface scheme for GCMS. I. soil model. International Journal of Climatology, 11: 111-133.

Wilm, H., Dunford, E., 1945. Effect of timber cutting on water available for streamflow from a Lodgepole Pine, United States Department of Agriculture, Washington, DC, USA.

Winkler, R.D., Moore, R.D., 2006. Variability in snow accumulation patterns within forest stands on the interior plateau of British Columbia, Canada. Hydrological Processes, 20(17): 3683-3695.

Winkler, R.D., Spittlehouse, D.L., Golding, D.L., 2005. Measured differences in snow accumulation and melt among clearcut, juvenile, and mature forests in southern British Columbia. Hydrol. Processes, 19(1): 51-62.

Wever, N., Fierz, C., Mitterer, C., et al., 2014. Solving Richards Equation for snow improves snowpack meltwater runoff estimations in detailed multi-layer snowpack model. The Cryosphere, 8(1): 257-274.

Ye, H., Cohen, J., Rawlins, M., 2013. Discrimination of solid from liquid precipitation over Northern Eurasia using surface atmospheric conditions. Journal of Hydrometeorology, 14, 1345-1355.

Zhao, K., Popescu, S., Meng, X., et al., 2011. Characterizing forest canopy structure with lidar composite metrics and machine learning. Remote. Sens. Environ., 115(8): 1978-1996.

Zhang, Y., Chen, J.M., Miller, J.R., 2005. Determining digital hemispherical photograph exposure for leaf area index estimation. Agric. For. Meteorol., 133(1-4): 116.

8 *Acknowledgements*

This project would not have been possible without the numerous seasonal interns and students employed through the 'Mountain Hydrology and Mass Movements' and the 'Snow Hydrology' groups. Field work required snow measurements after every storm event and was often monotonous and in bad conditions. This work eliminated just about every powder day from them and deviated significantly from the typical benefits of being an SLF intern. Specific thanks go to: Clare Webster, Franziska Mohr, Giulia Mazzotti, Jan Magnusson, Roman Juras, Timea Marekova, Pascal Egli, Franziska Zeiger, Mirjam Stawicki, Florian Kobierska, Saskia Gindraux, Jiri Roubinek, Mathias Rieckh, Veronica Lechner, Thomas Werz, Stephan Vogel and Nena Karotten Griessinger, Claudia Bieler, and Anna Pöhlmann. Special thanks go to Luzi Bernard who served as the primary contact to the various landowners of the field areas. As a group, we have created a globally unrivalled dataset!

Thanks go to the Snow hydrology group for endless support. This was a collaborative work and simply not possible without their help. Specifically, Tobias Jonas the principle supervisor has been extremely patient and has been there every step of the way. Not once was I able to stump him with a Matlab question (I will find one though!). My officemates were always there both scientifically and personally. Jan Magnusson you are a programming guru. Nena 'Karotten' Griesinger, your laughter helped me through the hardest days. Florian Kobierska, your endless energy is an inspiration.

Big thanks go to Harald Bugmann for leading me through the Doctoral process, having me as a part of his Forest Ecology group, and his willingness for a remote working environment.

This work would have come to an abrupt halt without the support of Felix Morsdorf who was an immense help with technical LiDAR details. Florian Zellweger furthered this, and set me on the correct

trajectory during my LiDAR data initiation. Patrick Schleppi contributed significantly with technical hemispherical photograph support and lots of patience.

Many including, Janet Prevey, Clare Webster, Christopher Hoyle and Adam Winstral have helped with editing support as well acted as voices from the 'homeland' when needed!

Auch wenn ich nicht „Chuchichäschtli" richtig sagen oder richtig Bündner Dialekt sprechen kann, bin ich trotzdem stolz, dass ich endlich ein bisschen Deutsch kann. Ich bin meinen Kollegen sehr dankbar, die mir mit unglaublich viel Geduld und Lachen Deutsch beigebracht haben.

C. David Moeser

Email:	cdmoeser@yahoo.com
Phone:	+41 774 25 28 51
DOB:	30.05.1977
Citizenship:	USA

Education

ETHZ - Swiss Federal Institute of Technology Zürich (2012- Present)
- **PhD** candidate: Snow Hydrology
- Dissertation Title: The Influence of Forest Canopy Structure on Snow Hydrology

University of Nevada, Reno (2008- 2010)
- **M.S.** Hydrology
- Thesis Title: Development, analysis and use of a distributed wireless sensor network for quantifying spatial trends of snow depth and snow water equivalence around meteorological stations with and without snow sensing equipment

Fort Lewis College, Durango, Colorado (2001-2004) Cum Laude
- **B.S.** Environmental Geology, Chemistry Minor
- Thesis Title: Discriminating pre- and post mining effects on The middle fork of mineral creek, Silverton, CO, using tree core analysi**s**
  - Eugene M. Shoemaker Award, given to the outstanding senior in the earth sciences
  - Freda T. Roof Scholarship and Julie Turner Oliva Scholarship recipient, given for superior academic performance.

Employment

Swiss Institute for Snow and Avalanche Research, SLF –*Research Snow Hydrologist* / PHD candidate (February 2012 – Present) Davos, Switzerland
- Developed new algorithms for improved snow melt runoff modeling and data analysis
- Responsible for aerial and terrestrial LiDAR (light detection and ranging) data gathering, manipulation and use
- Supervised biweekly snow survey campaigns (total: 12 employees)

World Business Council For Sustainable Development – **Water Project** - Temporary *Hydrologist* (September 2011 – February 2012) Geneva, Switzerland
- Modeled water and energy use linkages between food, feed and fiber management scenarios
- Coordinated knowledge exchanges involving UN organizations, research institutes and businesses for water related projects

Swiss Institute for Snow and Avalanche Research, SLF – (Praktikant) *Snow Hydrologist* (Jan 2010 – July 2011) Davos, Switzerland
- Leader of snow survey campaigns within a high alpine basin in avalanche terrain

- Performed snow melt analyses using physically based models
- Learned and applied large scale meteorological and geographic data parsing and analysis

University of Nevada, Reno *– Research Assistant* (September 2008 – December 2010)
- Deployment and maintenance of wireless snow depth sensing equipment and affiliated meteorological stations
- Performed statistical and geo-statistical modeling of snow water equivalence
- Installed and monitored stilling wells and V-notch weirs on a local stream

Bureau of Land Management/ U.S. Forest Service *– Hydrologic Technician* (2005- 2007)
Durango, CO
- Received STAR award (2005, 2006) for outstanding performance
- Monitored and quantified surface and groundwater water quantity and quality in springs and streams within Colorado, Utah and New Mexico
    - Installed and monitored groundwater monitoring wells and piezometers
    - Characterized and remediated forest streams
- Compiled all work with a GIS framework for water rights applications

Teaching

Invited Instructor – ETHZ, *Department of Environment Systems Science (2013,2014)*
Course: Environmental Measurement Laboratory (701)
- Developed course and laboratory structure for a 6-hour lecture module that was designed to integrate matlab programing with remotely sensed data

Teaching assistant - University of Nevada, Reno *– Department of Natural Resources and Environmental Science* (2008 – 2010)
Course(s): Principles of Ecohydrology (295), Ecohydrology field camp (400)
- Developed new course material and methods
- Lectured and supervised field and laboratory work

University of Nevada Cooperative Extension, "Discover your Future Program" (2009, 2010)
- Served as activity leader and guest lecturer about basic hydrologic field methods and applications for high school students

Advised graduate students
- Jiri Roubinek: MSc – Snow hydrology (2012) – Charles University, Prague – Czech Rep.
- Giulia Mazzotti: MSc – Snow hydrology (present) – ETH, Zürich - Switzerland

Published papers

Moeser, D., J. Roubinek, P. Schleppi, F. Morsdorf, T. Jonas; *Canopy closure, LAI and radiation transfer from airborne LiDAR synthetic images*; 2014; Agricultural and Forest Meteorology, doi: 10.1016/j.agrformet.2014.06.008

Moeser, D., F. Morsdorf, T. Jonas; *Novel Forest Structure Metrics from Airborne LiDAR data for improved snow interception estimation*, 2015; Agriculture and Forest Meteorology, doi: 10.1016/j.agrformet.2015.04.013

Moeser, D., M. Stähli, T. Jonas; *Improved snow interception modeling using novel canopy parameters from airborne LIDAR data*, 2015; Water Resources Research, doi: 10.1002/2014WR016724

Moeser, D., G. Mazzotti, N. Helbig, T. Jonas; *Representing spatial variability in forest snow: Implementation of a new interception model*, 2016; Water Resources Research, accepted - 4.Jan

External reports and grant proposals

Swiss National Science Foundation – Co-wrote successful grant proposal, *'Snow Distribution Dynamics Under Forest Canopy' (2012)*

United States Department of Interior – Agriculture Research Service – *Wrote* document, *'Recommended Procedure for Assessing Soil Disturbances in Vegetation Management Projects within Sensitive Areas of the Lake Tahoe Basin'* (2008)
- Interagency planning guide directed towards governmental land management agencies (U.S. Forest Service, Tahoe Regional Planning Agency), NGO's and private contractors

Conference papers and presentations

Moeser, D., M. Stähli, T. Jonas; "*Snow Interception Modeling,*" oral presentation, The International Union of Geodesy and Geophysics, Prague, Czech Republic, June 2015

Moeser, D., F. Morsdorf, T. Jonas; *"Improving Snow Canopy Interception Modeling Using Airborne LiDAR Data,"* poster presentation, American Geophysical Union meeting, San Francisco, California, December 2014

Moeser, D., J. Roubinek, F. Morsdorf, T. Jonas; "*Snow Distribution Dynamics Under The Forest Canopy,*" poster presentation, American Geophysical Union meeting, San Francisco, California, December 2013

Moeser, D., T. Jonas, F. Morsdorf; *"Linking snow accumulation patterns in forests with LiDAR derived canopy structure data,"* oral presentation, Davos Atmosphere and Cryosphere Assembly – The International Union of Geodesy and Geophysics, Davos, Switzerland, July 2013

Jonas, T., **D. Moeser**, F. Morsdorf; "*Linking Forest Snow Distribution Measurements with Canopy Structure Data,*" Presented by Dr. Tobias Jonas at the American Geophysical Union meeting, San Francisco, California, December 2012

Jonas, T., **D. Moeser**, J. Magnusson, M. Bavay; "*Validation of Multiple Approaches for Modeling SWE Distribution and Subsequent Snowmelt in a Small Alpine Watershed,*" Presented by Dr. Tobias Jonas at the International Union of Geodesy and Geophysics, Melbourne, Australia, July 2011

Moeser, D., M. Walker, C. Skalka, J. Frolik; "*A Distributed Wireless Sensor Network for Quantifying Spatial Trends of Snow Depth and Snow Water Equivalent,*" Presented by Dr. Mark Walker at the 79th Annual Western Snow Conference, Stateline, NV, April 2011.

Moeser, D., M. Walker, C. Skalka, J. Frolik; *"Development, Analysis & Use of a Distributed Wireless Sensor Network for Quantifying Spatial Trends of Snow Depth & Snow Water Equivalence Around Meteorological Stations With & Without Snow Sensing Equipment,"*

Presented by Dr. Mark Walker at the Nevada Water Resources Association, Annual conference Reno, NV, February 2011.

Moeser, D., Skalka, C**.**, M. Walker, J. Frolik; "*Snowcloud: Development of a Distributed In Situ Instrument for Snowpack Monitoring,*" poster presentation, American Geophysical Union meeting, San Francisco, California, December 2009

Computer competencies

- Programming – Matlab, R
- GIS Software
- Statistical modeling software
- Data Logging Software

Hydrologic and engineering equipment competencies

- Creation, Installation, Maintenance and Interrogation of:
  - Automated stilling wells / hyporheic zone samplers / ground water monitoring wells / piezometers / V notch weirs
- Use/Installation, Maintenance and Interrogation of:
  - AA, flow mate, Marsh McBurney and Pygmy flow meters / Parshal flumes / precipitation gages / pressure transducers
  - Snow pillows / Federal snow samplers / snow tubes
  - Wireless sensor networks of snow depth and temperature sensing nodes
  - Ground penetration radar
  - Terrestrial laser scanning
  - Total station and other surveying equipment

Volunteer experience

Student Organization for International Water Issues (2008-2010)
- Chaired the 2009 fundraising campaign for student engagement experiences in Cameroon and Guatemala for the implementation of sustainable water systems
- Served on international trip planning committee

Animas River Stakeholders Group (2003 – 2006) Silverton, CO
- Performed water quality analyses of abandoned mine waters surrounding Silverton, CO
- Analyzed and aggregated water quality data for the newly formed Silverton area water quality database

Languages

- English – Native proficiency
- German – CEFR level B2
- Spanish – CEFR level B2